eXPRESS Polymer Letters Vol.6, No.1 (2012) 1
Available online at www.expresspolymlett.com
DOI: 10.3144/expresspolymlett.2012.1

Preface – 'Publication pollution'

*T. Czigány**

Department of Polymer Engineering, Faculty of Mechanical Engineering, Budapest University of Technology and Economics, Műegyetem rkp. 3., H-1111, Budapest, Hungary

Dear Readers,

eXPRESS Polymer Letters has entered its sixth volume, with an impact factor of 1.575, which is about 10% higher than last year. Assessing the past 5 years, statistically speaking 466 full research papers and 60 short editorial papers presenting actual trends and novelties have been published so far. International reputation and recognition of the journal increases year by year, with a growing number of citations and publication downloads. In ***eXPRESS Polymer Letters***, despite its young age, there have already been published certain papers that reached thousands of downloads and over 50 citations in the Web of Science. These remarkable results are due to the strict peer reviewing process of the journal that results in a rejection rate of almost 80%.

However, we cannot ignore the negative tendencies that seem to escalate nowadays, which can be divided into three main groups. Firstly, owing to the 'publication pressure', weak, poor quality manuscripts are flooding the editorial offices. This is simply denoted as 'publication pollution' by us, that only causes excess work to the editors, but does not contribute to the state-of-knowledge at all. The second, even worse phenomenon that also has its roots in the 'publication pressure' is the parallel publication of identical (or minimally modified) results in various journals, which raises a very serious ethical problem in science. It is a huge responsibility for academic leaders, research team leaders and PhD supervisors to prevent publication of results that have already been submitted or accepted elsewhere or perhaps even appeared in another journal. This 'cloning' of publications may provide short term advantages for the authors as they will have improved statistics and higher cumulative impact factor, but in the long run such unethical behaviour is sooner or later revealed, and the journals will no longer accept any publication by the authors or by their institutions involved. This kind of paper multiplication increases 'publication pollution' again, and does not contribute to a deeper scientific knowledge. The third, and most serious, problem is plagiarism that raises questions falling under the category of criminal law, as it may constitute crime. To present other people's results as if they were one's own without indicating the source is a reprehensible and despicable act.

Based on the above we consider it important to act together against such unethical behaviour of some authors, and for the sake of sustainable development all actors of education, research, development and innovation sites should actively participate to prevent 'publication pollution'.

Finally, we are grateful for the painstaking work of our authors and referees, and in the name of the editor-in-chief, the international advisory board and the local editorial team, the editor wishes you a lot of success in year 2012. Sincerely yours,

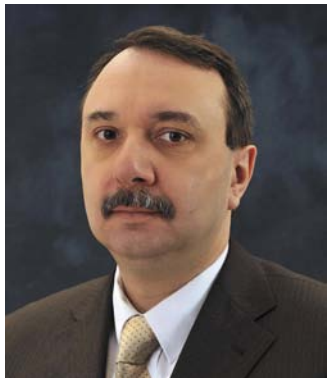

Prof. Dr. Tibor Czigány, editor

*Corresponding author, e-mail: czigany@eik.bme.hu

eXPRESS Polymer Letters Vol.6, No.1 (2012) 2–13
Available online at www.expresspolymlett.com
DOI: 10.3144/expresspolymlett.2012.2

Hybrid thin films derived from UV-curable acrylate-modified waterborne polyurethane and monodispersed colloidal silica

W. C. Lin[1], C. H. Yang[2], T. L. Wang[2], Y. T. Shieh[2], W. J. Chen[2]*

[1]Department of Environmental Engineering, Kun Shan University, Tainan 710, Taiwan
[2]Department of Chemical and Materials Engineering, National University of Kaohsiung, Kaohsiung 811, Taiwan

Received 18 April 2011; accepted in revised form 5 July 2011

Abstract. Hybrid thin films containing nano-sized inorganic domains were synthesized from UV-curable acrylate-modified waterborne polyurethane (WPU-AC) and monodispersed colloidal silica with coupling agent. The coupling agent, 3-(trimethoxysilyl)propyl methacrylate (MSMA), was bonded onto colloidal silica first, and then mixed with WPU-AC to form a precursor solution. This precursor was spin coated, dried and UV-cured to generate the hybrid films. The silica content in the hybrid thin films was varied from 0 to 30 wt%. Experimental results showed the aggregation of silica particles in the hybrid films. Thus, the silica domain in the hybrid films was varied from 30 to 50 nm by the different ratios of MSMA-silica to WPU-AC. The prepared hybrid films from the crosslinked WPU-AC/MSMA-silica showed much better thermal stability and mechanical properties than pure WPU-AC.

Keywords: *polymer composites, acrylate-modified waterborne polyurethane (WPU-AC), 3-(trimethoxysilyl)propyl methacrylate (MSMA), WPU-AC/MSMA-silica hybrid*

1. Introduction

Organic-inorganic hybrid materials have been extensively studied recently since these materials exhibit the combined characteristics of organic polymer (e.g., flexibility, ductility, dielectric property) and inorganic materials (e.g., rigidity, high thermal stability, strength, hardness, high refractive index) [1–7]. The properties of hybrid materials could be tailored through the adjustment of functionality or segment size of each component. Some special or novel properties can be acquired because of the effects of nanoparticles. Therefore, these materials could be widely used in the applications of protective coatings [8], high refractive index films [9–12], thin film transistor [13], light-emitting diodes [14–16], solar cell [17], optical waveguides materials [18–19], and photochromic materials [20].

Reinforcing of polymer is usually achieved in polymer composites by adding reinforcement such as fibers and particles to the polymer matrix, and some interesting results have been reported using polymer-clay nanocomposites [21], polymer-polyhedral oligomeric silsesquioxane nanocomposites [22], and organic-inorganic hybrids [1–20]. Generally, there are two typical kinds of organic-inorganic nanocomposites. One is the physical blend wherein weak physical interactions exist between organic and inorganic phases, e.g., hydrogen bonding, van der Waals forces. The other possesses strong chemical covalent or ionic bond between organic and inorganic phases. The addition of silica causes increase of crystallinity and chain orientation of polyurethane (PU) due to interactions between polymer and hydroxy groups present on the silica surface [23].

*Corresponding author, e-mail: yangch@nuk.edu.tw

The organic-inorganic hybrid method has attracted increasing attention in obtaining high performance composites. This approach has an advantage of processing at relatively low temperature by using a sol-gel process [5, 9, 18].

One of the recently studied materials is PU/inorganic oxide. PU has been used in optical devices due to its good optical properties and processibility. However, its thermal and mechanical properties have limited its applications [21]. One possible solution to the above problems is to hybridize with inorganic oxides such as silica or titania. The commonly used polymer was solvent-based polyurethane, and the silica network in the hybrid materials reported previously was prepared from alkoxysilanes [24]. The size distribution of the inorganic segment in the hybrid materials has not been well controlled, which may be very important for specific optical applications. One possible solution is to use monodispersed colloidal silica instead of preparing silica network from alkoxysilanes [24]. In real hybrid preparation, a selection of optimal hydrolytic media like alkoxysilanes is allowed to control the process of hybrid composites synthesis at an adequate level. However, the preparation of waterborne polyurethane/nanoscale colloidal silica composite films has not been addressed in the past studies. Such composite films could have important applications for optical coating or refractive index tuning films. In our previous work [25], waterborne polyurethane (WPU) was synthesized and followed by adding colloidal silica to prepare WPU-silica hybrids. The silica content in the hybrid thin films was varied from 0 to 50 wt%. The effect of interaction between silica particle and urethane polymer chains is more significant with increasing silica content. The prepared hybrid films show much better thermal stability and mechanical properties than pure WPU. The optical transparence did not linearly decrease with increasing the silica fraction in the hybrid thin film. Results showed that the prepared hybrid films demonstrated tunable transparence with the silica fraction in the films. This belongs to the physical blending. Here, we try to study the characteristics of the chemical covalent bonding/cross-linking through WPU-incorporating monodispersed colloidal silica with a coupling agent.

In this work, we extend our study that the hybrid films of polyester-based waterborne polyurethane incorporating monodispersed colloidal silica with a coupling agent (3-(trimethoxysilyl)propyl methacrylate, MSMA) as reinforcement are employed to investigate their properties. This combines the methods of a sol-gel process, spin coating, and UV-curing polymerization. The characteristics of hybrid films are investigated as a function of colloidal MSMA-silica content.

2. Experimental

2.1. Materials

Ester-type polyol (PA4210, M.W. ≒ 650, Taichin co., Kaohsiung, Taiwan), produced by the transesterification of ethyl glycol (EG), butyl glycol (BG), and adipic acid (mole ratio of EG to BG is 1:1), was dried and degassed under vacuum at 85°C for 24 h. Acetone was distilled over anhydrous $MgSO_4$ (Merck, Germany) at low pressure and stored over 3Å molecular sieve before use. 3-(Trimethoxysilyl)propylmethacrylate (MSMA, 98%, Aldrich, USA), colloidal silica (15–20 nm, 20 wt% in H_2O, Nissan Chem. Ind., Japan), 2-Hydroxyethylacrylate (2-HEA, First Chem., Taiwan), Photoinitiator (Irgacure 2959, Ciba-Gagy, Germany), and ethylene glycol ethyl ether (cellosolve, 99.9%, Acros) were used for the preparation of hybrid films.

2.2. Synthesis of Acrylate-modified WPU (WPU-AC)

Acrylate modified waterborne polyurethane (WPU-AC) dispersions were prepared employing our modified acetone process as Figure 1. The segmented prepolymer (polyester-DMPA-PU) used in this study was synthesized by a one-step addition reaction. To a 1000 ml four-necked round bottomed flask complete with an anchor-propeller stirrer 7 cm in length and 2 cm in width, a nitrogen inlet and outlet, and a thermometer, 4,4-methylenebis-(cyclohexyl isocyanate) (H_{12}MDI, Aldrich, USA) (95 g; 0.362 mol) was charged under a nitrogen gas atmosphere, and a solution of polyester polyol (113.87 g; 0.175 mol) and dimethylolpropionic acid/dimethylformamide (DMPA/DMF = 10 g/25 g, Merck, Germany) was then added over a period of 0.5 h under gentle stirring (300 rpm). The mixture was heated at 100°C until the theoretical NCO content of the

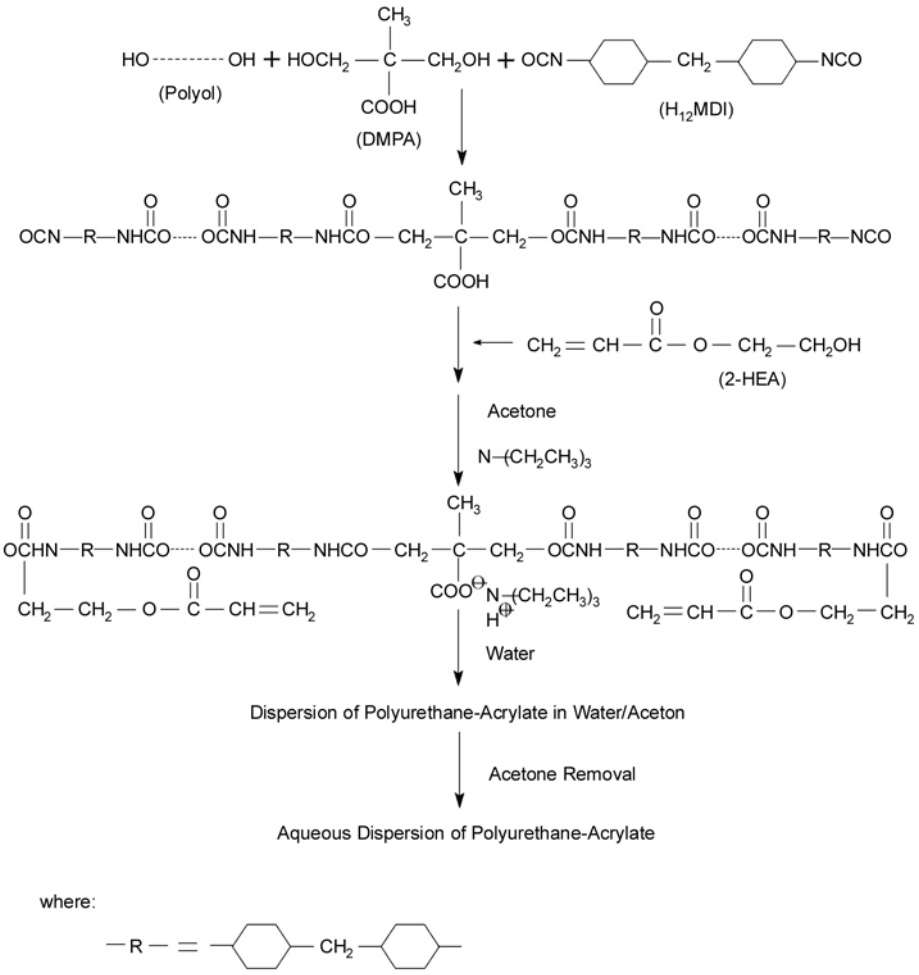

Figure 1. The process of acrylate-modified waterborne polyurethane (WPU-AC) dispersions

prepolymer was reached as determined by the di-n-butylamine titration method [26–27]. 2-Hydroxylethylacrylate (2-HEA, 15 g) was then added to react with the above NCO-terminated PU prepolymer. Partial residual NCO-terminated and 2-HEA-terminated PU solution was adjusted to acetone/PU-AC ratio of 2.8 through addition of a suitable amount of acetone. Triethylamine (TEA, 10 g, Merck, Germany), a neutralizing agent, was added immediately to the above solution (PU-AC solid, 243.87 g). The resulting mixture was then heated at 50°C for 3 min, yielding PU-AC anionomers in acetone. The stoichiometric ratio of TEA to COOH was 1.0. Doubly distilled water (500 g) was added to neutralize PU-AC anionomer solution at respective agitation rate and water addition rate of 500 rpm and 2 ml/min. An aqueous dispersion of ~33 wt% WPU-AC solids was obtained upon removal of acetone by rotary vacuum evaporation.

2.3. Preparation of colloidal MSMA-SiO_2

Preparation of colloidal MSMA-SiO_2 solution is shown in Figure 2. 3-(Trimethoxysilyl)propylmethacrylate, aqueous colloidal silica, de-ionized water and ethylene glycol ethyl ether (cellosolve, as

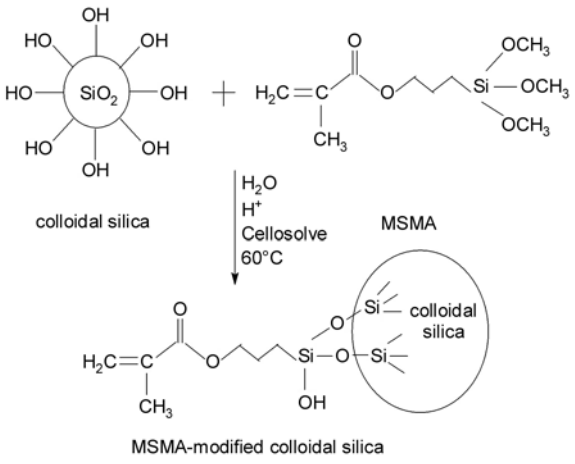

Figure 2. Preparation of MSMA-SiO_2 colloidal solution

a solvent) were mixed at the ratio of 2 : 5 : 2 : 25 with adding one drop of acetic acid. Then, the reaction mixture was poured into a three-necked reactor to perform the hydrolysis/condensation reaction. The reaction temperature was maintained at 60°C and the solution was stirred under a nitrogen flow for 2 h to obtain the transparent colloidal MSMA-SiO_2.

2.4. Preparation of WPU-AC-MSMA-SiO_2 hybrid films

The colloidal MSMA-silica obtained in the procedure of section 2.3. was subsequently mixed with a homogeneous WPU-AC dispersion with a desire ratio of WPU-AC/MSMA-SiO_2 and the photoinitiator, 5 wt% for total solid, to perform the preparation of film. The mixed solution was thoroughly stirred for 10 min. Then, this solution was spin coated on a 6 inches silicon wafer to control the final film thickness about 0.5 mm. The coated film was dried in glove box at room temperature (25°C) for 24 h, and then cured on a hot plate at 70°C for 1 h, 90°C for 1 h, and 150°C for 1 h, respectively. Finally, this dried film was subjected to UV-curing (Anly, APT-6S, Taiwan) with the irradiation of 2200 W power for 10 min.

2.5. Characterization

IR spectra of the prepared films were obtained on a KBr pellet using a Nicolet FTIR 550 Fourier-transform IR spectrophotometer. The ^{13}C and ^{29}Si NMR spectra of the solid-state hybrids were determined (Bruker, AVANCE-400, USA) with cross polarization combined with the magic angle spinning (CP/MAS) technique using 200–300 mg samples. The ^{13}C measured conditions of pulse width, recycle delay, contact time and number of scans are 5.5 μs, 5 s, 1000 μs, and 1486 cycles, respectively, at 100.6 MHz. These conditions corresponding to ^{29}Si are 3 μs, 200 s, 1000 μs, and 294 cycles, respectively, at 79.4 MHz. MSMA-SiO_2 particle size was measured on the transmittance electron microscope (120 kV, TEM, JOEL JEM-1230, Japan). The fracture surface of hybrid thin films was examined on the (Philips, XL-40FEG, Netherland) field emission scanning electron microscope (SEM).

Thermogravimetric analysis (TGA) was performed under a dry nitrogen flow using a Perkin-Elmer (TGA 7, USA) over a temperature range of 50–800°C at a heating rate 10°C/min. The TGA and DSC samples were prepared by spin-coating the mixed solution on a glass substrate, followed by curing at different temperature steps as described in the film prepared. Differential scanning calorimeter (DSC, Perkin-Elmer, DSC 7, USA) was used for the investigation of glass transition temperature of synthesized hybrid materials. Appropriate 5 mg of samples were sealed in aluminum sample pans. DSC analyses of these hybrid materials were then conducted under nitrogen flow at a heating rate of 20°C/min from –60 to 50°C. The stress-strain properties of the prepared films (1 mm thickness) were tested using an Instron (Shimadzu, AG-IS, Japan) at a pull rate of 10 mm/min.

Wide angle X-ray diffraction measurement was carried out with Rigaku ZD3609N (Japan) series, using CuK_α radiation at a scan rate of 5/min. The transmittance of the prepared hybrid films (ca. 0.5 mm thickness) was peeled from silicone wafer and then measured by using the UV-Vis spectrophotometer (Perkin-Elmer, Lambda 25, USA). The hardness of hybrid films (ca. 0.5 mm thickness) on silicone wafer was measured by using a pencil hardness tester (Jiin-Liang Co., B-3084T4, Taiwan) following the standard method of ASTM D1474-98 (2002).

3. Results and discussion

3.1. Analysis of chemical structure

Figure 3 shows the FTIR spectra of (a) MSMA, (b) colloidal silica, and (c) MSMA-silica (MSMA-SiO_2, MSMA/silica = 2.0/1.0), respectively. There are two characteristics from the comparison of the spectra. The first comes from the comparison of the Si–OH absorption band in the spectra. The Si–OH of the pure colloidal silica and MSMA is observed at 963 and 919 cm^{-1}, respectively, which is similar to previous report [28]. However, the Si–OH peak on silica and MSMA is completely disappeared with bonding MSMA onto silica. This suggests the complete condensation of the Si–OH bond on the colloidal silica or bond on MSMA. But a very weak Si–OCH_3 peak (1170 cm^{-1}) on MSMA still appeared in the spectrum of MSMA-SiO_2. This incomplete condensation of the Si–OCH_3 bond in MSMA probably resulted from a high MSMA content and thus the silica could not react with all of the Si–OCH_3 bonds on MSMA molecules. The second feature is the narrow absorption band of C=C at 1635 cm^{-1} in the spectra of (a) and (c), but it is reasonably absent in

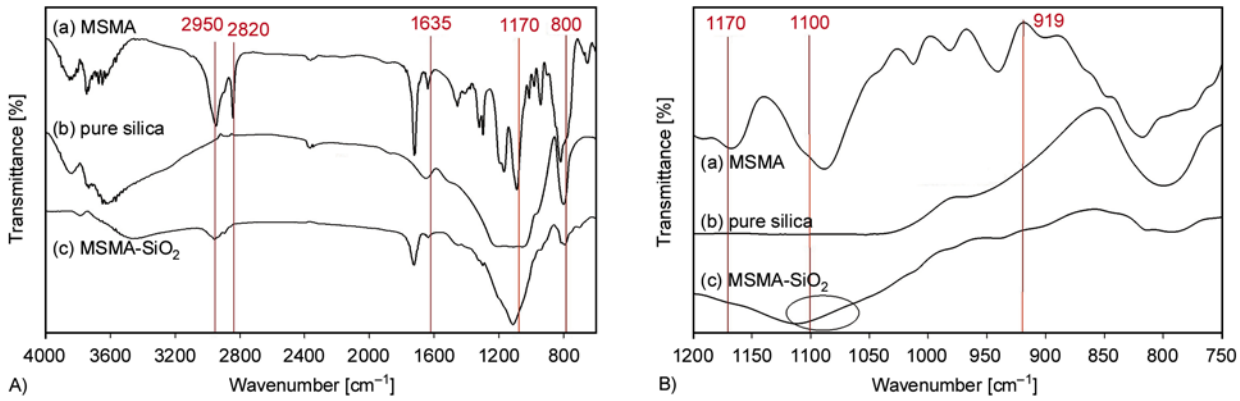

Figure 3. (A) Full-range and (B) specified-range (750–1200 cm^{-1}) FT-IR spectra of (a) MSMA, (b) pure silica and (c) MSMA-SiO_2

the spectra (b) of colloidal silica. On the other hand, the absorption bands of asymmetrical Si–O–Si (1110 cm^{-1}) and symmetrical Si–O–Si (800 cm^{-1}) are more significant in the spectrum of MSMA-SiO_2. This reflects that the Si–OCH3 groups on MSMA reacted with Si-OH groups on silica through the hydrolysis/condensation, resulting in the formation of Si–O–Si covalent bonding. The characteristic bands of MSMA are observed at 1100–1200, 1735, 2950 and 2800, and 1635 cm^{-1} corresponding to Si–O–C, C=O, $–CH_3$, and C=C, respectively. Figure 4A shows the FTIR spectra of (a) WPU-AC, (b) 5% MSMA-SiO_2/WPU-AC and (c) 20% MSMA-SiO_2/WPU-AC without UV-curing films, respectively. The absorption bands of C–O–C or Si–O–Si, C=C, C–H, and N–H are observed at 1039–1192, 1635, 2940, and 3250–3500 cm^{-1}, respectively. Asymmetrical Si–O–Si absorption band located at 1100 cm^{-1}, which increases with increasing MSMA-SiO_2 content. This indicates the formation of silica structure in the hybrid films. With the increase of MSMA-SiO_2 content, the absorption band of 800 cm^{-1} is also significant, corresponding to the formation of silica network. Moreover, the active group (C=C) at 1635 cm^{-1} still occurs in these films, which serves as further UV-curing polymerization to form an inorganic/organic hybrid film. The FTIR spectra corresponding to these hybrid films after UV-curing are shown in Figure 4B. It is obvious that the absorption band of C=C (1635 cm^{-1}) has disappeared through UV-curing reaction in the hybrid films. Also note that the broad bands of N–H can still be observed in the hybrid films.

^{13}C CP/MAS spectra of the MSMA-SiO_2, 5% MSMA-SiO_2/WPU-AC, and 20% MSMA-SiO_2/WPU-AC with UV-curing is shown in Figure 5. These spectra show a weak absorption peak at 106 ppm. The band might be due to the carbon atom of the Si–OCH_3 group [29]. The result indicates that the Si–OCH_3 residue exists in MSMA-SiO_2, 5% MSMA-SiO_2/WPU-AC and 20% MSMA-SiO_2/WPU-AC hybrids. For the case of MSMA-SiO_2, the carbon atoms on the methyl and methylene groups

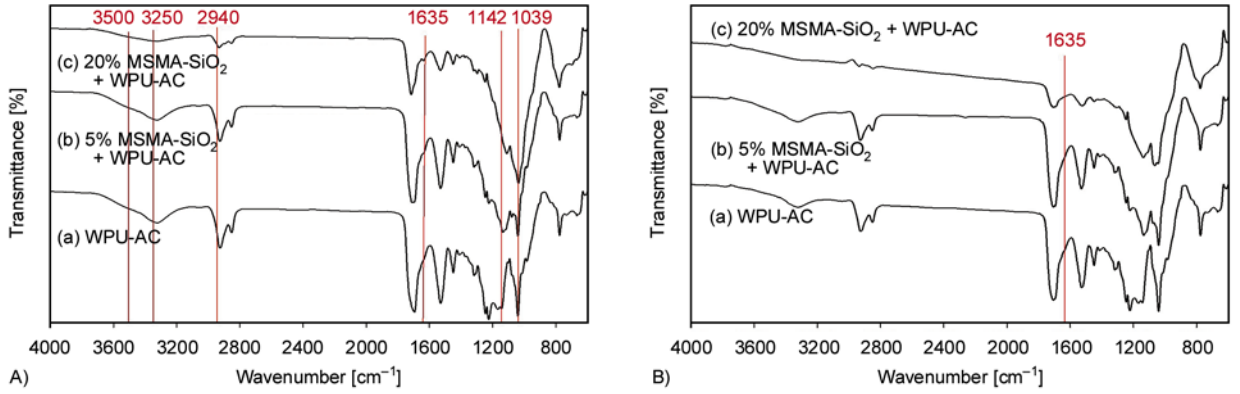

Figure 4. FT-IR spectra (A) before UV-curing and (B) after UV-curing for (a) WPU-AC, (b) 5% MSMA-SiO_2/WPU-AC and (c) 20% MSMA-SiO_2/WPU-AC

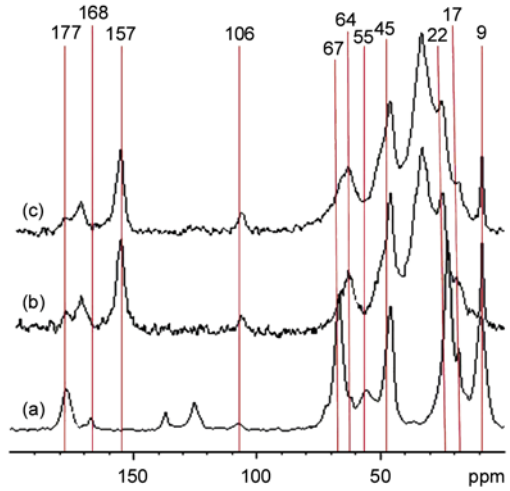

Figure 5. ^{13}C CP/MAS NMR spectra of MSMA-SiO_2 and MSMA-SiO_2/WPU-AC. (a) MSMA-SiO_2, (b) before UV-curing and (c) after UV-curing 5% MSMA-SiO_2/WPU-AC.

are observed at 9, 17, 22, 45, 55, 67, 106, 168, and 177 ppm. The absorption of 168 ppm corresponds to the C=C bond. The absorption peaks at 9, 22, and 67 correspond to propyl carbon atoms on MSMA molecules. The band at 17 is the methyl group. The absorption peaks of 45 and 55 ppm correspond to the carbon atoms of acrylic groups. And, the band of 177 ppm arises from the carbon atom of carboxyl group. In addition, the absorption peaks of 125 and 137 ppm result from the residue of cellosolve because this MSMA-SiO_2 sample is dried in room temperature. The carbon atoms on the WPU-AC chains are observed at 9, 27, 34, 47, 64, 157, 173 and 177 ppm. A peak centered at 157 ppm, is observed in the carbonyl region consisting of the urea and urethane carbons. The resonance at 64 ppm is ascribed to the soft-segment carbons that are adjacent to a urethane linkage. The absorption bands of 55 and 67 ppm for MSMA-SiO_2 are merged into the soft-segment carbons. The peak at 47 ppm is attributed to the secondary carbons on the cyclohexyl rings bonded to nitrogen atoms and CH_2 groups (C_8), respectively. The peaks at 34 and 27 ppm are associated with the primary carbons in the cyclohexyl rings. It is interesting to note that the line width of the 34 ppm peak is markedly sharp as compared with other peaks. This feature implies that an effective motional narrowing undergoes possibly due to the segmental motion of polymer chain. In addition, the band of 177 ppm in MSMA-SiO_2/WPU-AC becomes weaker than MSMA-SiO_2, indicating a diluted effect. The bands of 125 and 137 ppm disappeared in the spectra of MSMA-SiO_2/WPU-AC samples. This can be explained that the cellosolve residue is evolved during the baking step at 150°C for 1 h. It is noteworthy that the 168 ppm band of C=C bond exists in both MSMA-SiO_2 and MSMA-SiO_2/WPU-AC samples. But this peak cannot be observed in MSMA-SiO_2/WPU-AC film after UV-irradiation, indicating that the polymerization has been achieved between WPU-AC and MSMA-SiO_2 molecules. This result is consistent with FTIR observation.

To gain more insight into the influence of WPU-AC polymer chain on the silica, ^{29}Si CP/MAS NMR experiments of the prepared hybrid films have been performed and shown in Figure 6. The spectra show six peaks at –50 to –51, –57 to –59, –65 to –67, –91 to –93, –100 to –102, and –109 to –111 ppm (Figure 6A), which are assigned to T^1, T^2, T^3, Q^2, Q^3, and Q^4, respectively. The positions of these peaks are similar to previous reports [29, 30]. These peaks correspond to the chemical structures shown in Figure 6B. It is clear that T^i and Q^i peaks come from the coupling agent (MSMA) and colloidal silica, respectively. Q^i and T^i subpeaks were deconvoluted using a curve-fitting method (Figure 6C). The positions of T^1 (–50.5 ppm), T^2 (–58 ppm), T^3 (–66 ppm), Q^2 (–92 ppm), Q^3 (–101 ppm), and Q^4 (–110 ppm) points were first fixed, and then adjusted the area of these subpeaks to fit the corresponding full area of Q^i and T^i subpeaks. The maximum error associated with the deconvolution of ^{29}Si spectra is expected to be ±3%. The degree of condensation (D_c) in the hybrid materials was determined by a quantitative analysis based on the peak areas of species. The D_c of the hybrid materials was obtained from the proportion of T^i and Q^i according to Equation (1) [30]:

$$D_c\,[\%] = \left[\frac{T^1 + 2T^2 + 3T^3}{3} + \frac{Q^1 + 2Q^2 + 3Q^3 + 4Q^4}{4}\right]\cdot 100 \qquad (1)$$

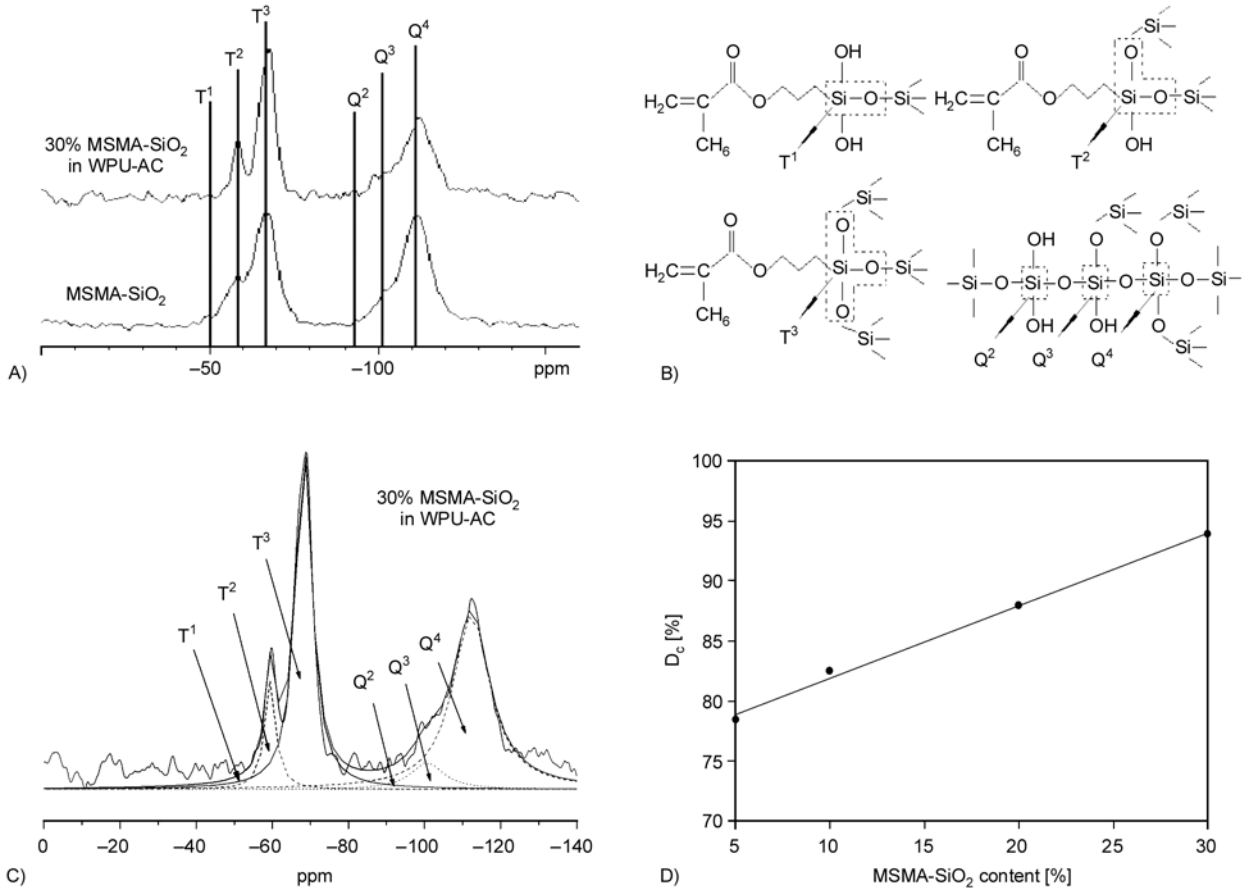

Figure 6. ^{29}Si CP/MAS NMR spectra of the hybrids with different MSMA-SiO_2 content: (A) wide scan, (B) theoretical structure, (C) deconvolution of T^1, T^2, T^3, Q^2, Q^3 and Q^4 components, and (D) the degree of condensation (D_c) of various MSMA-SiO_2 content in the hybrids

The proportion of T^i species decreases with increasing silica content in the prepared hybrid films but that of Q^i species and D_c shows the opposite trend from Figure 6D. Q^i directly depends on the Si–OH condensation of the silica. Hence, it is conceivable that it increases with increasing the silica content. Similar explanation can be used for the D_c because Q^i peaks corresponding to colloidal silica, whereas the weighting and power numbers of Q^i proportions are higher than T^i species (see Equation (1)). In comparison to our previous work [25], there exist significant differences in the ^{29}Si CP/MAS NMR results between the system in this work and the hybrid films of WPU and colloidal silica [25].

3.2. Micro-structure analysis

The size of the silica particle in the hybrid films was estimated from SEM micrographs. The size in the hybrids was generally larger than that in pure MSMA-SiO_2 (20–25 nm from TEM image in Figure 7A). It increased to more than 30–50 nm in the hybrid films of 30% MSMA-SiO_2/WPU-AC (Figure 7B). The large size of the silica particle might be due to the incomplete coverage of silica particle surface and results in aggregation. This reflects that the moiety of MSMA-SiO_2 plays an important role in the film quality of the prepared hybrid materials. There exists local concave form in the hybrid film in Figure 7B. This might be due to the difference on the thermal expansion coefficient between the WPU-AC and silica.

3.3. Thermal analysis

TGA and DTG curves of the hybrid with 30% are shown in Figure 8A. Notations on Figure 8A are: ΔY is the weight loss due to the thermal degradation of polymer and T_{onset} is the thermal degradation onset temperature for the polymer. Two weight loss points are observed in this TGA curve. Weight loss at 293–316°C (ΔY_1) is due to the degradation of WPU-AC. This process is ascribed to a complex procedure including depolymerization and decom-

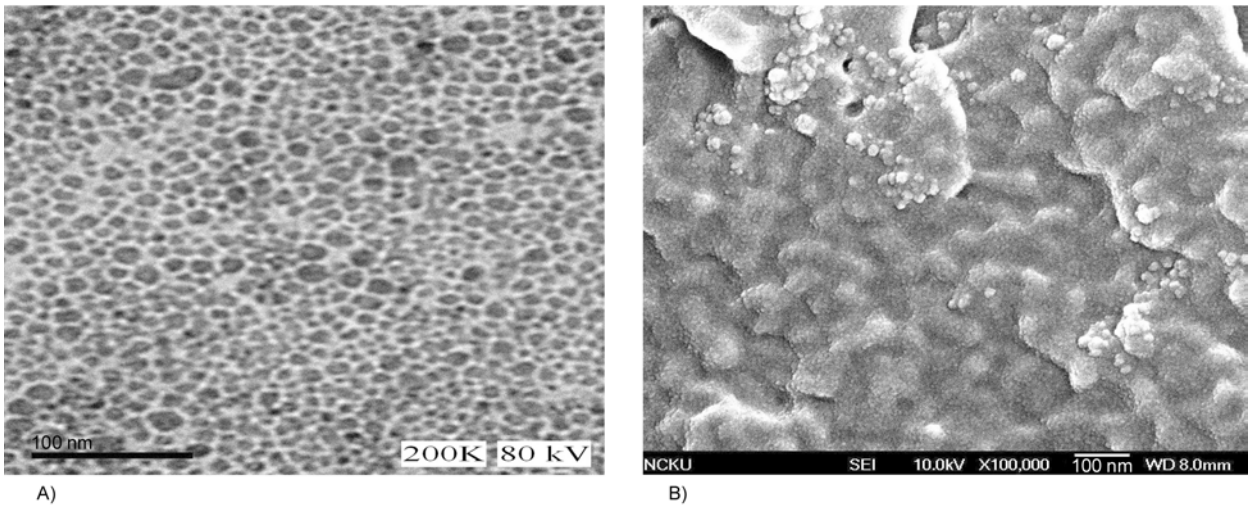

Figure 7. (A) TEM image of MSMA-SiO_2 and (B) FE-SEM image of 30% MSMA-SiO_2/WPU-AC

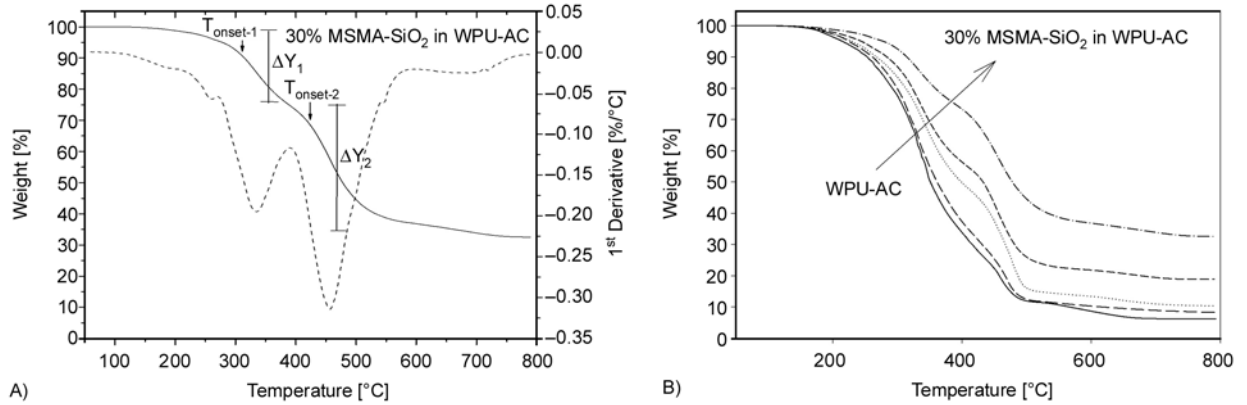

Figure 8. (A) TGA and DTG curves of the hybrid with 30% MSMA-SiO_2 in WPU-AC matrix and (B) TGA curve of the hybrids at a heating rate of 10°C/min under nitrogen flow; (—) WPU-AC, (– –) 5% MSMA-SiO_2/WPU-AC, (···) 10% MSMA-SiO_2/WPU-AC, (- - -) 20% MSMA-SiO2 /WPU-AC and (– · –) 30% MSMA-SiO_2/WPU-AC

position of the urethane and ester units of WPU-AC chains. Meanwhile, ΔY_2 at 427–454°C is due to the generation of delayed-degradation for WPU-AC-MSMA-SiO_2 cross-linked networks during the TGA thermal degradation process. Thermal degradation led to the production of aldehyde and alkene end-groups in the molten state. ΔY_1 decreases with increasing the MSMA-SiO_2 content, implying that the cross-linked density increases with increasing the MSMA-SiO_2 content. This cross-linked network needs higher temperature to decompose. Thus, the materials of higher MSMA-SiO_2 content remain more portion of cross-linked networks, resulting in the more MSMA-SiO_2 content the higherΔY_2 (Table 1). A shoulder at ca. 240°C may correspond to the degradation of un-reacted components. A series of TGA experiments and the thermal-analysis data of the hybrids are shown in Figure 8B and summarized in Table 1, respectively, revealing that

Table 1. Weight loss and degradation temperature of hybrid films with different MSMA-SiO_2 content in WPU-AC

Sample	$T_{onset-1}$ [°C]	$T_{onset-2}$ [°C]	ΔY_1 [%]	ΔY_2 [%]
WPU-AC	293	448	74.2	14.9
5% MSMA-SiO_2	301	454	69.8	19.3
10% MSMA-SiO_2	307	451	52.0	34.1
20% MSMA-SiO_2	310	435	44.9	36.1
30% MSMA-SiO_2	316	427	25.4	37.8

$T_{onset-1}$ increases with increasing MSMA-SiO_2 content in the hybrids, but ΔY_1 shows the opposite trend. This result is because the chemical bonding between WPU-AC and MSMA-SiO_2 increases with increasing MSMA-SiO_2 content in the hybrid films, leading to the enhancement of thermal stability by incorporating silica moiety in the hybrids. On the other hand, the second degradation process shows a complex result. The $T_{onset-2}$ first increased and then

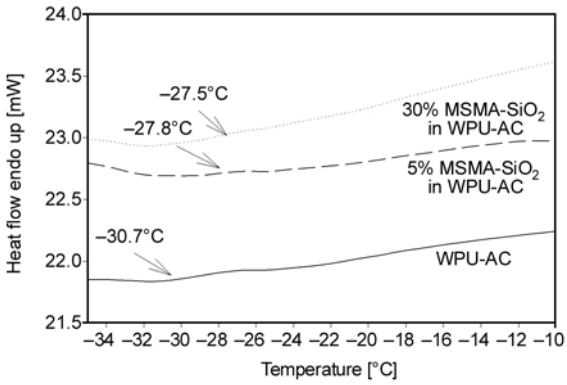

Figure 9. DSC curves of the hybrids with different MSMA-SiO_2 content in WPU-AC matrix

decreased with increasing MSMA-SiO_2 content in the hybrids. A close examination of ΔY_2 results revealed that this value decreased with increasing MSMA-SiO_2 content in the hybrids. This implies that the weight loss involves polymer degradation and silica phase transition.

The glass transition temperatures (T_g) of the hybrids can be carefully measured using DSC instrument. Figure 9 shows the T_g as a function of MSMA-SiO_2 content embedded in WPU-AC films after UV-curing. It is clear that the value of T_g increases with increasing MSMA-SiO_2 content. This is because the WPU-AC polymer is a linear molecule. With the addition of MSMA-SiO_2 in WPU-AC and UV-curing, the chemical bonding is achieved between WPU-AC and MSMA-SiO_2 to form a network structure, resulting in an increase in the T_g.

3.4. X-ray diffraction

Figure 10 shows the X-ray diffraction curves for the hybrid samples with varying the MSMA-SiO_2 content. For pure WPU-AC, nearly amorphous diffraction peak is seen near $2\theta = 200$ [31], indicating the crystalline of polyester segments. As the MSMA-SiO_2 content increases, the diffraction becomes weaker and broader, whereas this peak gradually shifts to the characteristics of pure silica. This implies that the orientation of polyester segments is significantly disturbed through the addition of MSMA-SiO_2 in WPU-AC matrix, suggesting that the influence of the chemical bonding exists between WPU-AC and MSMA-SiO_2 after UV-curing. This result is supported by previous FTIR and ^{13}C-NMR results.

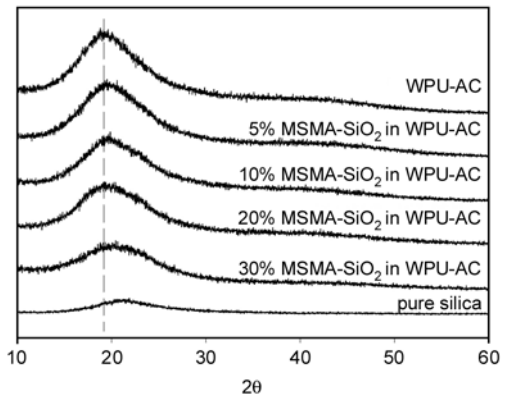

Figure 10. X-ray diffractograms of the hybrids with different MSMA-SiO_2 content in WPU-AC matrix

3.5. UV-Vis spectra

The transmittance of MSMA-SiO_2/WPU-AC hybrid films in the wavelength range of 200–1100 nm is shown in Figure 11, revealing that the transmittance of visible region (633 nm as a criterion) decreases from 92% of pure WPU-AC to 5% of the hybrid with 30% MSMA-SiO_2 content. It is because the smaller refractive index of pure silica than the WPU-AC. Hence, the refractive index can be decreased with increasing the MSMA-SiO_2 content, whereas the silica particle is isolated as a 'dispersive' heterogeneous phase in the hybrid matrix, which results in a serious light scattering. This leads to a hazy thin film. This is different from the simple WPU-silica hybrid films [25] which the transmittance at 633 nm decreases from 92% of pure WPU to 20% of the hybrid with 20% silica content, and then gradually increases from 20 to 87% of the hybrid with 50% silica content.

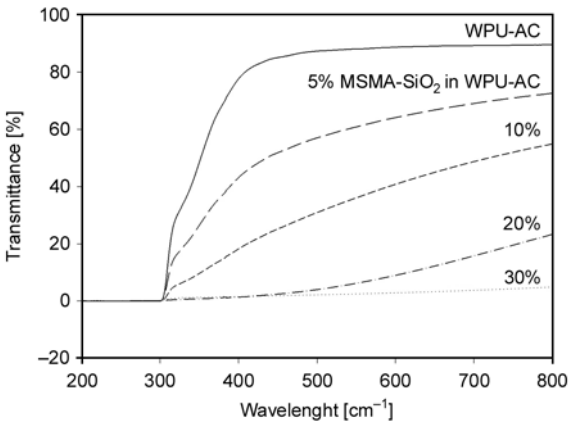

Figure 11. Transmittance variation of the MSMA-SiO_2/WPU-AC hybrid films (ca. 0.5 mm thickness) with different MSMA-SiO_2 content in the wavelength range of 200–1100 nm

3.6. Mechanical properties

The hardness of the prepared hybrid films was tested by a pencil test, as shown in Table 2. The hardness increases up to 4H with increasing the MSMA-SiO_2 content to 10 and more to 30%. It suggests the importance of incorporating the silica moiety on the mechanical properties. The mechanical properties of the hybrid films were obtained from stress-strain experiments. Figure 12 shows the variation of the Young's modulus as a function of the MSMA-SiO_2 content for the hybrids. There is a noticeable increase in the Young's modulus with the UV-curing, whereas the Young's modulus of the hybrid films increases with increasing MSMA-SiO_2 content. Evidently, the incorporation of MSMA-SiO_2 in WPU-AC polymer chains produces a network structure through the UV-curable cross-linking, leading to a significant improvement in the mechanical properties which is in agreement with the FTIR and NMR results. The mechanical strength of the UV-cured WPU-AC incorporating MSMA-SiO_2 films is higher than that of the simple WPU-silica hybrid films [25]. Also note that the plateau strength seems to be reached at 20% MSMA-SiO_2 content, reflecting that the aggregation of silica particles becomes more significant at MSMA-SiO_2 content higher than 20% (see Figure 7B). The high incorporation of MSMA-SiO_2 (20–30%) in WPU-AC polymer matrix produces a non-homogeneous network after the UV-curable cross-linking, which cannot contribute more enhancement in mechanical strength.

Table 2. Hardness of WPU-AC/MSMA-SiO_2 hybrid films

Sample	MSMA-SiO_2 content in hybrids				
	WPU-AC	5%	10%	20%	30%
before UV-curing	2B	B	B-HB	HB	HB
after UV-curing	H	2H	4H	4H	4H

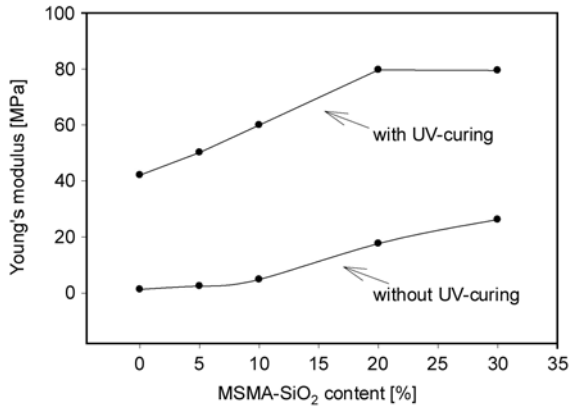

Figure 12. Dependence of the Young's modulus [MPa] on the MSMA-SiO_2 content

4. Conclusions

Cross-linked hybrid thin films containing nano-size inorganic materials have been prepared from incorporating reaction between acrylate-waterborne polyurethane and colloidal silica-bearing coupling agent. Experimental results show the aggregation of silica particles in the hybrid films. The incorporation of MSMA-SiO_2 in WPU-AC polymer chains produces a network structure through the UV-curable cross-linking, leading to a significant improvement in thermal decomposition temperature, hardness, and the mechanical properties (0–20 wt% MSMA-SiO_2). The hybrid also demonstrates a tunable transparence with the added silica fraction in the film.

Acknowledgements

Financial support from the National Science Council in Taiwan (NSC-99-2221-E-390-029-MY2) is gratefully acknowledged.

References

[1] Chten Y., Iroh J. O.: Synthesis and characterization of polyimide/silica hybrid composites. Chemistry of Materials, **11**, 1218–1222 (1999). DOI: 10.1021/cm9804281

[2] Ogoshi T., Itoh H., Kim K-M., Chujo Y.: Synthesis of organic−inorganic polymer hybrids having interpenetrating polymer network structure by formation of ruthenium−bipyridyl complex. Macromolecules, **35**, 334–338 (2002). DOI: 10.1021/ma010819c

[3] Shang X-Y., Zhu Z-K., Yin J., Ma X-D.: Compatibility of soluble polyimide/silica hybrids induced by a coupling agent. Chemistry of Materials, **14**, 71–77 (2002). DOI: 10.1021/cm010088v

[4] Matějka L., Dušek K., Pleštil J., Kříž J., Lednický F.: Formation and structure of the epoxy-silica hybrids. Polymer, **40**, 171–181 (1999). DOI: 10.1016/S0032-3861(98)00214-6

[5] Huang Z. H., Qiu K. Y.: The effects of interactions on the properties of acrylic polymers/silica hybrid materials prepared by the in situ sol-gel process. Polymer, **38**, 521–526 (1997). DOI: 10.1016/S0032-3861(96)00561-7

[6] Yu Y-Y., Chen C-Y., Chen W-C.: Synthesis and characterization of organic–inorganic hybrid thin films from poly(acrylic) and monodispersed colloidal silica. Polymer, **44**, 593–601 (2003). DOI: 10.1016/S0032-3861(02)00824-8

[7] Zhou S., Wu L., Sun J., Shen W.: The change of the properties of acrylic-based polyurethane via addition of nano-silica. Progress in Organic Coatings, **45**, 33–42 (2002).
DOI: 10.1016/S0300-9440(02)00085-1

[8] Ershad-Langroudi A., Mai C., Vigier G., Vassoille R.: Hydrophobic hybrid inorganic-organic thin film prepared by sol-gel process for glass protection and strengthening applications. Journal of Applied Polymer Science, **65**, 2387–2393 (1997).
DOI: 10.1002/(SICI)1097-4628(19970919)65:12<2387::AID-APP11>3.0.CO;2-Z

[9] Wang B., Wilkes G. L., Hedrick J. C., Liptak S. C., McGrath J. E.: New high-refractive-index organic/inorganic hybrid materials from sol-gel processing. Macromolecules, **24**, 3449–3450 (1991).
DOI: 10.1021/ma00011a063

[10] Chen W-C., Lee S-J., Lee L-H., Lin J-L.: Synthesis and characterization of trialkoxysilane-capped poly (methyl methacrylate)–titania hybrid optical thin films. Journal of Materials Chemistry, **9**, 2999–3003 (1999).
DOI: 10.1039/A906157F

[11] Lee L. H., Chen W. C.: High-refractive-index thin films prepared from trialkoxysilane-capped poly(methyl methacrylate)−titania materials. Chemistry of Materials, **13**, 1137–1142 (2001).
DOI: 10.1021/cm000937z

[12] Chang C-C., Chen W-C.: High-refractive-index thin films prepared from aminoalkoxysilane-capped pyromellitic dianhydride–titania hybrid materials. Journal of Polymer Science Part A: Polymer Chemistry, **39**, 3419–3427, (2001).
DOI: 10.1002/pola.1323

[13] Kagan C. R., Mitzi D. B., Dimitrakopoulos C. D.: Organic-inorganic hybrid materials as semiconducting channels in thin-film field-effect transistors. Science, **286**, 945–947 (1999).
DOI: 10.1126/science.286.5441.945

[14] Lee T-W., Park O. O., Yoon J., Kim J-J.: Polymer-layered silicate nanocomposite light-emitting devices. Advanced Materials, **13**, 211–213 (2001).
DOI: 10.1002/1521-4095(200102)13:3<211::AID-ADMA211>3.0.CO;2-H

[15] Huang W. Y., Ho S. W., Kwei T. K., Okamoto Y.: Photoluminescence behavior of poly(quinoline)s in silica glasses via the sol–gel process. Applied Physics Letters, **80**, 1162–1164 (2002).
DOI: 10.1063/1.1450040

[16] Tang J., Wang C., Wang Y., Sun J., Yang B.: An oligophenylenevinylene derivative encapsulatedin sol–gel silica matrix. Journal of Materials Chemistry, **11**, 1370–1373 (2001).
DOI: 10.1039/B009569I

[17] Huynh W. U., Dittmer J. J., Alivisatos A. P.: Hybrid nanorod-polymer solar cells. Science, **295**, 2425–2427 (2002).
DOI: 10.1126/science.1069156

[18] Yoshida M., Prasad P. N.: Sol−gel-processed SiO_2/TiO_2/poly(vinylpyrrolidone) composite materials for optical waveguides. Chemistry of Materials, **8**, 235–241 (1996).
DOI: 10.1021/cm950331o

[19] Xu C., Eldada L., Wu C., Norwood R. A., Shacklette L. W., Yardley J. T., Wei Y.: Photoimageable, low shrinkage organic−inorganic hybrid materials for practical multimode channel waveguides. Chemistry of Materials, **8**, 2701–2703 (1996).
DOI: 10.1021/cm9603009

[20] Biteau J., Chaput F., Lahlil K., Boilot J-P., Tsivgoulis G. M., Lehn J-M., Darracq B., Marois C., Lévy Y.: Large and stable refractive index change in photochromic hybrid materials. Chemistry of Materials, **10**, 1945–1950 (1998).
DOI: 10.1021/cm980106h

[21] Yao K. J., Song M., Hourston D. J., Luo D. Z.: Polymer/layered clay nanocomposites: 2 polyurethane nanocomposites. Polymer, **43**, 1017–1020 (2002).
DOI: 10.1016/S0032-3861(01)00650-4

[22] Jeon H. G., Mather P. T., Haddad T. S.: Shape memory and nanostructure in poly(norbornyl-POSS) copolymers. Polymer International, **49**, 453–457 (2000).
DOI: 10.1002/(SICI)1097-0126(200005)49:5<453::AID-PI332>3.0.CO;2-H

[23] Nunes R. C. R., Pereira R. A., Fonseca J. L. C., Pereira M. R.: X-ray studies on compositions of polyurethane and silica. Polymer Testing, **20**, 707–712 (2001).
DOI: 10.1016/S0142-9418(01)00007-1

[24] Cho J. W., Lee S. H.: Influence of silica on shape memory effect and mechanical properties of polyurethane–silica hybrids. European Polymer Journal, **40**, 1343–1348 (2004).
DOI: 10.1016/j.eurpolymj.2004.01.041

[25] Yang C-H., Liu F-J., Liu Y-P., Liao W-T.: Hybrids of colloidal silica and waterborne polyurethane. Journal of Colloid and Interface Science, **302**, 123–132 (2006).
DOI: 10.1016/j.jcis.2006.06.001

[26] Yang C-H., Lin S-M., Wen T-C.: Application of statistical experimental strategies to the process optimization of waterborne polyurethane. Polymer Engineering and Science, **35**, 722–730 (1995).
DOI: 10.1002/pen.760350812

[27] Wen T-C., Wu M-S., Yang C-H.: Spectroscopic investigations of poly(oxypropylene)glycol-based waterborne polyurethane doped with lithium perchlorate. Macromolecules, **32**, 2712–2720 (1999).
DOI: 10.1021/ma9804489

[28] Chan C-K., Peng S-L., Chu I-M., Ni S-C.: Effects of heat treatment on the properties of poly(methyl methacrylate)/silica hybrid materials prepared by sol–gel process. Polymer, **42**, 4189–4196 (2001).
DOI: 10.1016/S0032-3861(00)00817-X

[29] Joseph R., Zhang S., Ford W. T.: Structure and dynamics of a colloidal silica−poly(methyl methacrylate) composite by ^{13}C and ^{29}Si MAS NMR spectroscopy. Macromolecules, **29**, 1305–1312 (1996).
DOI: 10.1021/ma951111z

[30] Chang T. C., Wang Y. T., Hong Y. S., Chiu Y. S.: Organic–inorganic hybrid materials. V. Dynamics and degradation of poly(methyl methacrylate) silica hybrids. Journal of Polymer Science Part A: Polymer Chemistry, **38**, 1972–1980 (2000).
DOI: 10.1002/(SICI)1099-0518(20000601)38:11<1972::AID-POLA60>3.0.co;2-5

[31] Zhang T., Xi K., Yu X., Gu M., Guo S., Gu B., Wang H.: Synthesis, properties of fullerene-containing polyurethane–urea and its optical limiting absorption. Polymer, **44**, 2647–2654 (2003).
DOI: 10.1016/S0032-3861(03)00173-3

eXPRESS Polymer Letters Vol.6, No.1 (2012) 14–25
Available online at www.expresspolymlett.com
DOI: 10.3144/expresspolymlett.2012.3

Effects of partial replacement of silica with surface modified nanocrystalline cellulose on properties of natural rubber nanocomposites

S. H. Xu, J. Gu, Y. F. Luo, D. M. Jia*

College of Materials science and Engineering, South China University of Technology, Guangzhou 510640, China

Received 17 April 2011; accepted in revised form 11 July 2011

Abstract. Nanocrystalline cellulose was modified by 3-aminopropyl-triethoxysilane (KH550). The modified nanocrystalline cellulose (MNCC) was further investigated to partially replace silica in natural rubber (NR) composites via coagulation. NR/MNCC/silica and NR/nanocrystalline cellulose (NCC)/silica nanocomposites were prepared. Through the comparison of vulcanization characteristics, processing properties of compounds and mechanical properties, compression fatigue properties, dynamic mechanical performance of NR/MNCC/silica and NR/NCC/silica nanocomposites, MNCC was proved to be more efficient than NCC. MNCC could activate the vulcanization process, suppress Payne effect, increase 300% modulus, tear strength and hardness, and reduce the heat build-up and compression set. Moreover, fine MNCC dispersion and strong interfacial interaction were achieved in NR/MNCC/silica nanocomposites. The observed reinforcement effects were evaluated based on the results of apparent crosslinking density (V_r), thermo-gravimetric (TG) and scanning electron microscopic (SEM) analyses of NR/MNCC/silica in comparison with NR/NCC/silica nanocomposites.

Keywords: *rubber, nanocrystalline cellulose, silica, reinforcement, KH550*

1. Introduction

Silica has always been used as an important rubber reinforcing filler for its excellent reinforcing effect [1–3], the capability of reducing the heat build-up [4, 5] and rolling resistance of rubber [6, 7]. Therefore, silica as an indispensable filler in rubber products has been widely used and investigated. However, its high density (2.5 g/cm^3 compared to general raw rubber 1.1 g/cm^3) makes the density of silica filled vulcanized rubber relatively high, thus reversing an important property of polymer materials, namely their low density. Moreover, silica leads to a number of shortcomings such as long processing time, high energy consumption and environment pollution during processing. Therefore, it is a quite urgent issue for researchers to find some new materials which can overcome above mentioned shortcomings and partially replace silica applications in rubber.

Natural cellulose has similar chemical composition to starch [8, 9]. When used as a macromolecular rubber-reinforcing fillers, they exhibit many advantages like renewability, biodegradability, easy to process, low density, low cost, energy conservation and environmental friendliness. In addition, compared to starch, a number of improved properties such as observably increased mechanical properties [10, 12, 16], improved hot air aging performance [13], processing properties [11, 14], dynamic mechanical performance and reduced heat build-up [14] have been achieved in the applications of MCC and NCC derived from natural cellulose in rubber.

*Corresponding author, e-mail: psjgu@scut.edu.cn

Therefore, MCC and NCC have drawn increasing interest in recent years [10–18]. However, the nature of numerous hydroxyl groups and easy aggregation of NCC make it difficult to disperse NCC finely in a rubber matrix. Surface modification [19–22] and chemical grafting [23–26] have been used in the modifications of NCC. The main objectives of the modifications are improving the NCC dispersion and reinforcing the interfacial strength between NCC and rubber. Among them, surface modification is simple and one can select different surfactants according to needs.

Many researches have studied the applications of MCC and NCC in plastics matrices [27–31], while in rubber [10–16], there are only a few publications. Most of them mainly studied the influence of adding MCC [14] or chemical modified NCC [13, 15] on the structure and properties of rubber. Three kinds of coupling agents, namely, phenyl isocyanate (PI), alkenyl succinic anhydride (ASA), and 3-isopropenyl-α, α′-dimethylbenzyl isocyanate (TMI) were applied to chemically modify the surface of chitin whiskers and then prepared a kind of nanocomposite films. Even though there was an increase in filler matrix interaction, this did not contribute to the improvement in the mechanical properties of the resulting nanocomposite. It was concluded that this loss of performance was due to the partial destruction of the three-dimensional network of chitin whiskers assumed to be present in the unmodified composites [15]. Nevertheless, the attempting of applying surface modified NCC to rubber is rarely reported. Recently, the preparation, surface modification [32] of NCC and its applications in rubber [13] were discussed by our research group.

In this paper, NCC was firstly modified by KH550 and used as filler to partially replace silica. Two types of compounds and nanocomposites, NR/NCC/silica and NR/MNCC/silica were prepared by direct compounding with NRL, respectively. Properties and morphology of these compounds nanocomposites and corresponding NCC were investigated. The observed reinforcement effect of MNCC on NR/silica nanocomposites was discussed. The result exhibit that the way of using KH550 to modify NCC is simpler and more efficient than other methods. The comprehensive properties of NR/MNCC/silica composites have been largely improved, because KH550 can react with both NCC and rubber. Therefore, it makes a very real sense using the NCC as a new energy saving filler partly replacing silica.

2. Experiment

2.1. Materials

Natural rubber latex (NRL) with 59.4 wt% solid contents was purchased from 11 th Rubber Plant, Guangzhou, China. Microcrystalline Cellulose (MCC) was provided by Gaoyao Gaoli Additives Corp., Guangdong, China. Precipitated silica with trade name of ZQ356 was obtained from Zhuzhou xinglong chemical industrial Co., LTD., Hunan, China. KH550 was provided by Shuguang chemicals group Co., LTD. Nanjing, China. Other reagents and ingredients were commercially available and were used as received.

2.2. Preparation of NCC suspension

MCC was stirred for 30 min at 45°C with 64 wt% H_2SO_4. The amount of H2SO4 was set to 10 ml per 1 g MCC. After hydrolysis, the suspension was repeatedly washed with distilled water by centrifugation until the pH approached 7.0. Then 1.0 wt% NaOH solution was added to the suspension with stirring to adjust the suspension pH to 7.0 and then kept at room temperature for 24 h.

2.3. Preparation of MNCC suspension

NCC was mixed with ethanol (95 wt%) under stirring at ambient temperature. After an addition of KH550, the reaction lasted 2 h under refluxing. MNCC was then obtained after a filtering and dried. Deionized water was added to the final product to prepare a MNCC suspension.

2.4. Preparation of NR/NCC and NR/MNCC compounds

NCC suspension or MNCC suspension was mixed with NRL and stirred vigorously at room temperature for 15 min, and then 10 wt% $CaCl_2$ solution was added to co-coagulate the mixture. The coagulum was washed by water and then dried in oven at 70ºC until a constant weight was obtained.

2.5. Preparation of NR/NCC/silica and NR/MNCC/silica nanocomposites

NR/NCC/silica and NR/MNCC/silica nanocomposites were prepared by the following procedure. Basic formulation of all compounds is shown in

Table 1. compounding formulation (phr)

	NCC	Silica	KH550
U-1	0	30	0
U-2	5	25	0
U-3	10	20	0
U-4	15	15	0
U-5	20	10	0
U-6	25	5	0
M-1	0	30	0.9
M-2	5	25	0.9
M-3	10	20	0.9
M-4	15	15	0.9
M-5	20	10	0.9
M-6	25	5	0.9

Note: The other ingredients of U-1–U-6 and M-1–M-6 are as following(phr): NR 100, Sulphur 2, Zinc oxide 5, Stearic acid 2, N-cyclohexyl-2-benzothiazole 1.5, sulfenamide2,2'-dibenzothiazole disulfide 0.5, N-isopropyl-N′-phenyl-p-phenylenediamine 1.5.

Table 1. Compounding was carried out on a two-roll mill by the well-known method. The rubber compound sheets were compressed and vulcanized at 143ºC for t_{c90}.

2.6. The morphology analysis of NCC

NCC and silica suspension was diluted and then treated by ultrasound. Transmission electron microscopy (TEM) observations were made with a Philip Tecnai 12 TEM (Eindhoven, Netherlands) electron microscope. A droplet of a treated suspension of NCC and silica was deposited and allowed to dry on a copper mesh.

2.7. Characterization of NR/NCC/silica and NR/MNCC/silica compounds

Vulcanization parameters and curing curve for NR/NCC/silica and NR/MNCC/silica compounds were tested in a standard testing procedure according to ISO 3417:1991 using a U-CAN UR2030 vulcameter (U-CAN DYNATEX INC, Taiwan).

The strain dependence of G' for NR/NCC/silica and NR/MNCC/silica compounds was determined by RPA (GÖTTFERT VISCO – ELASTOGRAPH, Germany). The condition of measurement is at a frequency of 1 Hz, a temperature of 60ºC, and a strain range from 1.4 to 420%.

2.8. Properties of NR/NCC/silica and NR/MNCC/silica nanocomposites tests

The mechanical properties, such as modulus at 300%, tensile strength, and tear strength, were measured according to ISO/DIS37-1994 and ISO 34-1-1994 specifications. U-CAN electron tensile testing machine (U-CAN DYNATEX INC, Taiwan) was used with the crosshead speed of 500 mm/min. Three to five specimens were measured for each particular sample and the average values were reported with standard deviation showing the error range. The hardness of the samples was measured by a Shore A Durometer.

To study the heat build-up and compression set at dynamic situation of these materials, U-CAN UD-380 (U-CAN DYNATEX Inc., Taiwan) was used according to ISO 4666/3-1982. Cylindrical rubber specimens (25 mm in height and 17.5 mm in diameter) were subjected to repeated compression using a grip. The frequency of loading was 30 Hz, and the stroke (double amplitude) of imposed oscillation was 4.45 mm. The severity of the test was adjusted by varying the static compressive load applied to the sample, and compressive loadings of 24.5 kg were treated. The test procedures were terminated when the sample carried out about 25 min constant load or constant displacement fatigue. Three specimens were measured for each particular sample and the average values were reported with standard deviation showing the error range.

The dynamic mechanical analysis of the samples was obtained by using an EPLEXOR 500N DMA Analyzer (GABO Corp. Germany). The specimens were analyzed in tensile mode at a constant frequency of 10 Hz, and a temperature range from −80 to 10°C at a heating rate of 2.5°C/min. Mechanical loss factor ($\tan\delta$) was measured as a function of temperature for the samples under identical conditions.

2.9. Structure of NR/NCC/silica and NR/MNCC/silica nanocomposites [33]

Crosslinking density was determined by equilibrium swelling method. The samples were swollen in hexane at room temperature to an equilibrium state and then removed from the solvent, and the hexane on the surface was quickly blotted off with tissue paper. The samples were immediately weighed on an analytical balance to the tolerance of 1 mg and then dried at vacuum. Assuming the mass loss of the rubber during swelling is the same for all the samples, the volume fraction of rubber in swollen gel (V_r), which was used to represent the crosslink-

ing density of the vulcanizates, was determined by the Equation (1):

$$V_r = \frac{1}{1 + \left(\frac{m_b}{m_a} - 1\right) \cdot \frac{\rho_r}{\alpha \rho_s}} \quad (1)$$

where m_a and m_b is the sample masses before and after swelling, ρ_r and ρ_s is the density of rubber and solvent, respectively, and α is the mass fraction of rubber in the vulcanizates.

The TGA of vulcanized rubber were detected on TGAR5000IR TA Analyzer produced by TA Corp. (USA). Test condition: heating rate of 10ºC/min, temperature range from room temperature to 600ºC, nitrogen atmosphere.

Scanning electron microscopy (SEM) was performed to investigate the morphology of the NR/NCC, NR/MNCC and NR/MNCC/silica and nanocomposites with a LEO 1530 VP (LEO Company, Germany) SEM. The specimens were stretch-fractured, and then fractured, mounted, coated with thin film of gold, and observed. SEM micrographs were obtained using 5 kV.

3. Results and discussion

3.1. Influence of MNCC on properties of NR/MNCC/silica compounds

Vulcanization curves and parameters of the compounds are shown in Figure 1 and Table 2. It can be seen that t_{c90} exhibit constant decrease trends as the amount of NCC or MNCC increased from 5 to 25 phr. Meanwhile, the vulcanization rate constant k was gradually increased. The results prove that the addition of NCC or MNCC can promote rubber vulcanization and accelerate vulcanization rate [14]. As seen from Table 2, k was raised with the same amount MNCC compared to NCC. This is because KH550 can adsorb activator, promoting agents and sulphur, leading to activation of vulcanization. M_L and M_H of the compounds were decreased as the increasing of NCC. It is probably owing to the fact that NCC can act as a plasticizer, lead to better liquidity and improve the processing performance of the compounds [14]. However, M_L and M_H were nearly unchanged with the increasing of MNCC, but much higher than those of adding NCC. These are attributed to that KH550 can chemically react with both NCC and rubber, improve filler–rubber interactions therefore increase crosslinking density of nanocomposites. The modification effect of KH550 was confirmed by the following crosslinking density analysis results.

Table 2. Curing parameters of NR/NCC/silica and NR/MNCC/silica compounds (143ºC)

Sample numbers	t_{c10} [s]	t_{c90} [s]	M_L [dN·m]	M_H [dN·m]	k [min^{-1}]
U-1	279	504	1.04	25.57	26.7
U-2	320	646	0.87	19.08	18.4
U-3	293	623	0.87	17.41	18. 2
U-4	276	565	0.56	16.77	20.8
U-5	269	554	0.42	16.79	21.1
U-6	286	534	0.28	16.86	24.2
M-1	205	312	2.83	29.02	56.1
M-2	235	368	2.57	29.00	45.1
M-3	229	360	2.27	28.42	45.8
M-4	207	326	2.21	30.75	50.4
M-5	191	303	2.21	27.76	53.6
M-6	157	267	2.56	27.18	54.5

Vulcanization rate constant, $k = 100/(t_{c90} - t_{c10})$ [min^{-1}]

Figure 2 shows a plot of elastic modulus versus the logarithm of strain of unvulcanized compounds. As can be seen, the modulus of the compounds decreases gradually and shows a typical nonlinear behavior

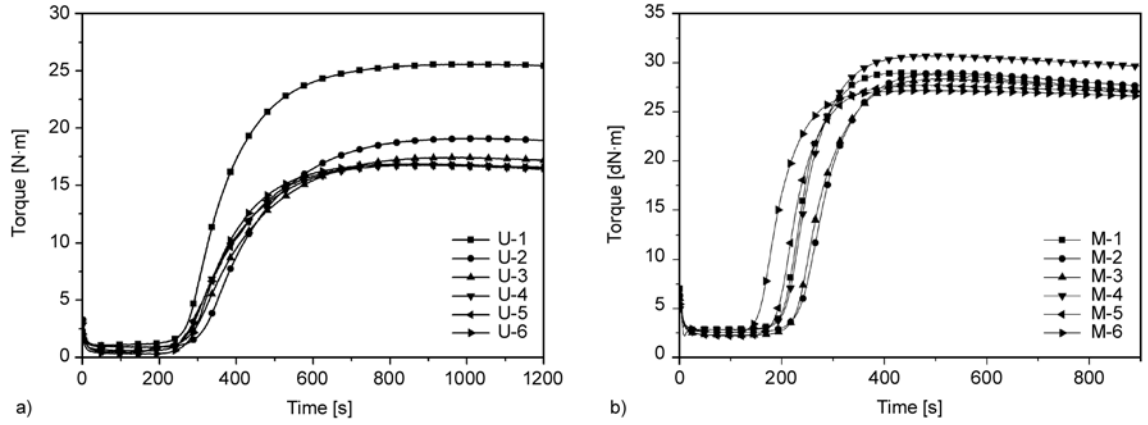

Figure 1. Curing curves of (a) NR/NCC/silica and (b) NR/MNCC/silica compounds (143°C)

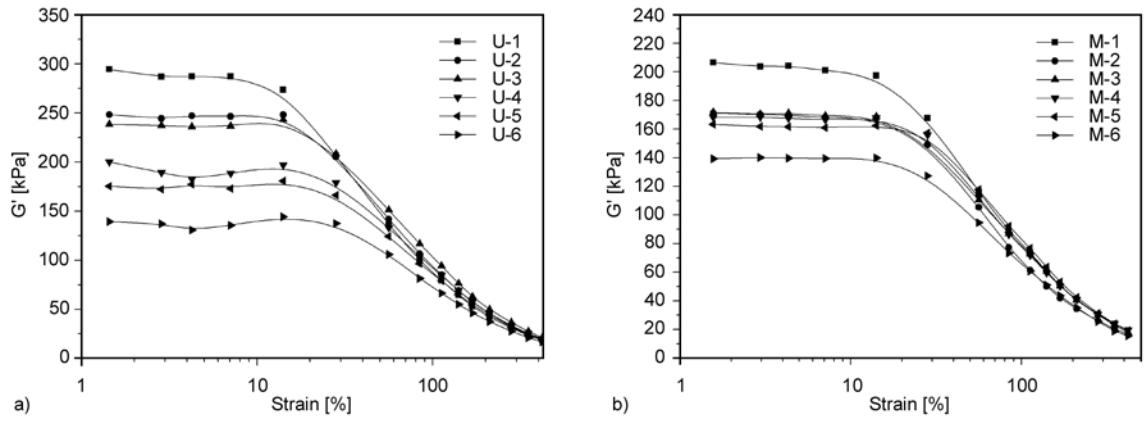

Figure 2. *G′*-Strain curves of (a) NR/NCC/silica and (b) NR/MNCC/silica compounds

with increasing strain, which is generally termed the 'Payne effect'. It is also observed that the 'Payne effect' obviously decreased with the NCC or MNCC increasing and changed significantly with the same amount of NCC compared to MNCC. The Payne effect is mainly related to the filler network formed in the rubber matrix which has been widely accepted. The rubber trapped or caged in the filler network would at least be partially 'dead,' behaving like a filler. Therefore, the effective volume of the silica would increase substantially upon filler networking. However, with the addition of NCC, especially MNCC, the networking of silica is weakened and so is the Payne effect. Likely because the addition of NCC or MNCC can reduce the interaction of filler aggregates and the degree of the network, enhance the interaction between NR and filler, and improving the processing performance of compounds [14].

3.2. Influence of MNCC on structure and properties of NR/MNCC/silica nanocomposites

The mechanical properties of nanocomposites with different NCC or MNCC were examined and shown in Figure 3, the total amount of NCC or MNCC and silica was 30 phr. It can be seen that the tensile strength, elongation at break and tear strength were almost kept constant with the increasing of NCC or MNCC. While the modulus at 300% increased significantly. This improvement may be explained by the high stiffness and rod-like structure of NCC, whereas a significant increase of Young's modulus was achieved by using NCC to reinforce nanocomposites, which is consistent with the reports by Cao *et al.* [30] and Ten *et al.* [31]. It can also be observed that the mechanical properties of nanocomposites were obviously improved by using MNCC compare to NCC, especially on 300% modulus, tear strength and hardness [34]. When the NCC was modified by KH550, more uniform distribution of MNCC particles in the NR matrix was obtained (as shown in the following SEM photograph) as well as the stronger interfacial interaction between rubber and fillers, which would allow an improvement of mechanical properties of the nanocomposites. And these results were in accordance with the following crosslinking density analysis.

As shown in Figure 4, heat build-up and compression set at dynamic compression of nanocomposites were significantly decreased with the increasing NCC or MNCC. Moreover, with the addition of MNCC, they show further decreases than with NCC. It is believed that the heat build-up of reinforced rubber is mainly came from lag, which is caused by deformation and reorganization of secondary aggregates of filler under the action of high gravitational field in the rubber. The better the dispersion of filler, the lower the heat build-up and the smaller the deformation [4, 5]. Heat build-up and compression set were reduced with the increasing of NCC content because the hydroxyl groups on the surface of NCC were less than on silica, which were easily agglomerated. It is consistent with the report results of Bai and Li [14]. Moreover, the heat build-up and compression set are also due to the friction between filler and matrix and between filler particles [35]. As the distribution of MNCC gets even, the agglomeration tendency between particles decreases (as shown in the following SEM photographs) which weakens the filler network. Thus, it reduces

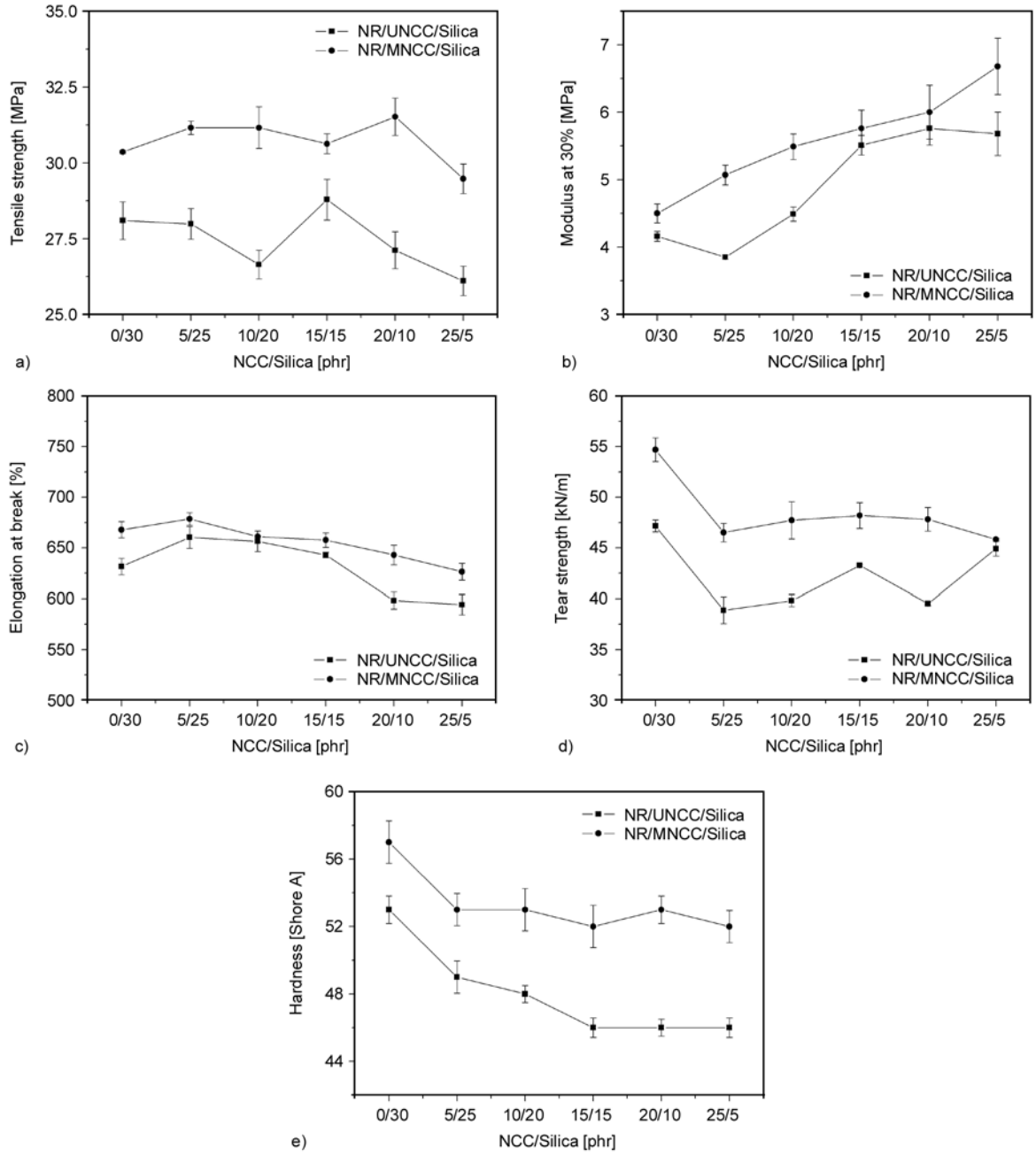

Figure 3. Variation of mechanical properties of NR/NCC/silica and NR/MNCC/silica nanocomposites via NCC/silica content. The values are given by average and the error ranges are given by standard deviation as evaluated by results from 3–5 parallel samples. (a) Tensile strength, (b) 300% modulus, (c) elongation at break, (d) tear strength and (e) hardness (Shore A). Lines are to guide the eye.

the repeatedly breakdown and reforming of the network, and leads to lower heat build-up and compression set.

It is well-known that the rolling resistance and skid resistance of tires play an important role in the running of an automotive. From the viscoelastic property point of view, an ideal material, which is able to meet the requirements of a high-performance tire, should give a lower tanδ at 60ºC and demonstrate high lag at 0ºC to reduce rolling resistance and obtain high-skid resistance. Figure 5 and Table 3 show tanδ-T curves and its data of nanocomposites. It can be seen that glass transition temperature (T_g) was nearly unchanged and the tanδ peak of nanocomposites became much higher as the increasing of NCC or MNCC. Moreover, the tanδ peak was further enhanced when NCC was modified. This can be explained by the rubber shell theory [36]. NCC can

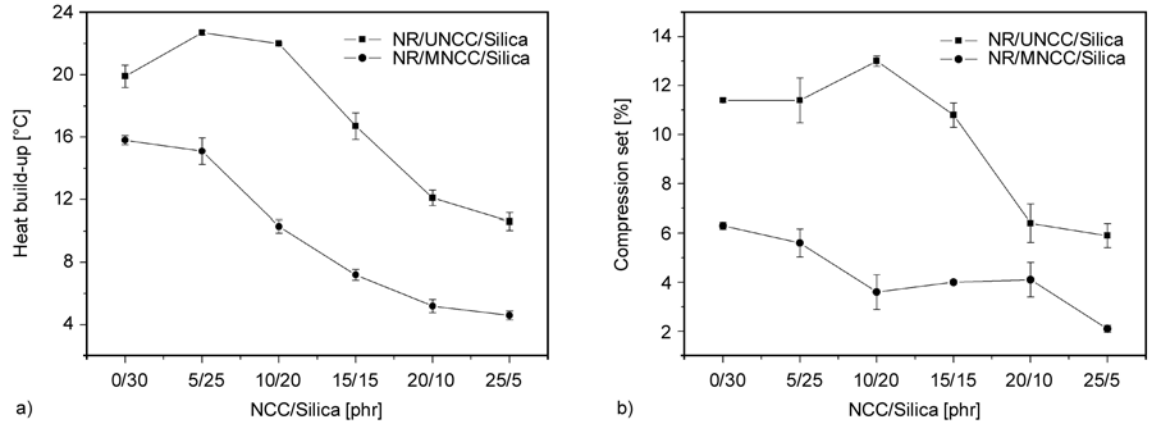

Figure 4. The heat effect of the compression fatigue of the NR/NCC/silica and NR/MNCC/silica nanocomposites via NCC/silica content. The values are given by average and the error ranges are given by standard deviation as evaluated by results from 3 parallel samples. (a) Heat build-up and (b) compression set. Lines are to guide the eye.

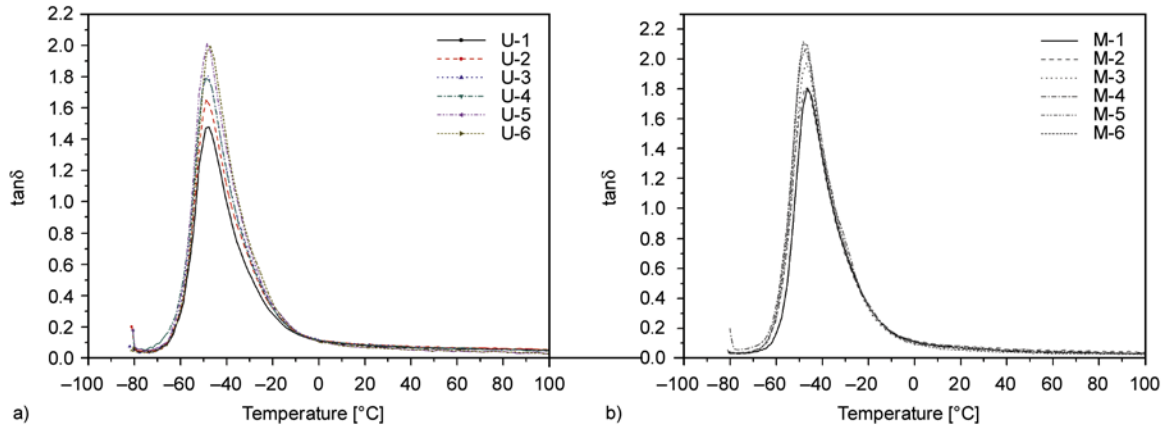

Figure 5. tan δ-T curves of (a) NR/NCC/silica and (b) NR/MNCC/silica nanocomposites

physically absorb rubber chain due to the large surface area to volume ratio. The bound rubber chains that are absorbed by NCC, are still in the glassy state while the other rubber chains stay in the elastic state. With the help of KH550, more rubber chains can be chemically absorbed by NCC because of the reactivity of KH550 with rubber and NCC. Which means more rubber chains will stay in the glass transition area and result in the increase of tan δ. As can be seen from Table 3, it gets the lower tan δ at 60ºC, while the same tan δ at 0ºC when the NCC was modified. It means that if nanocomposites were applied to the tire tread, low- rolling resistance can be achieved accompanied with maintained skid resistance [6–7, 14].

Table 3. Data of the tan δ-T curves of NR/NCC/silica nanocomposites and NR/MNCC/silica nanocomposites

Sample numbers	T_g [ºC]	0ºC–tan δ	60ºC–tan δ
U-1	–47.7	0.115	0.060
U-2	–49.0	0.116	0.064
U-3	–47.9	0.119	0.062
U-4	–49.0	0.113	0.060
U-5	–48.5	0.111	0.049
U-6	–47.2	0.103	0.047
M-1	–46.5	0.110	0.040
M-2	–47.5	0.123	0.046
M-3	–46.8	0.095	0.037
M-4	–47.3	0.117	0.045
M-5	–48.4	0.104	0.039
M-6	–48.4	0.097	0.031

Apparent crosslink density of nanocomposites is shown in Figure 6. With an increase of NCC, the apparent crosslink density shows a slight downtrend for NR/NCC/silica nanocomposites. However, the apparent crosslink density of NR/MNCC/silica nanocomposites improved to a different degree. These results are in accordance with that the MH reduced slightly with adding NCC, while MH improved when the NCC was modified. Since KH550 can chemically react with both NCC and rubber. The readily hydrolysable ethoxy group ($–OC_2H_5$) will react with hydroxyl groups on the

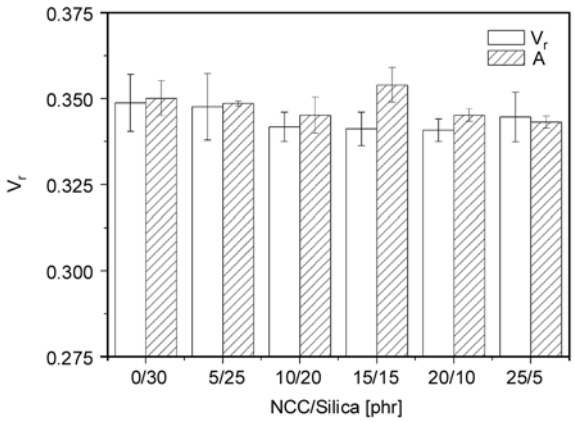

Figure 6. Apparent crosslinking density of NR/NCC/silica and NR/MNCC/silica nanocomposites. The values are given by average and the error ranges are given by standard deviation as evaluated by results from 4 parallel samples. Lines are to guide the eye.

NCC surface to form stable linkage. The γ-Aminopropyl ($–H_2NCH_2CH_2$) can form covalent bonds with the rubber. As a result, KH550 can connect NCC to rubber and increase crosslinking density. The other reason for the increase is that MNCC can reduce the adsorption of accelerator and sulfur by silica. Therefore, KH550 can strengthen the combination of rubber and filler, which shows apparent crosslink density, the mechanical properties and the dynamic mechanical properties increase, accompanied by the reduction of the heat build-up and permanent deformation.

Table 4. TG data of NR/NCC/silica and NR/MNCC/silica nanocomposites

Sample numbers	Temperature of 5% weight loss [ºC]	Temperature of maximum weight loss rate [ºC]	Residual mass [%]
U-1	307.86	365.69	23.05
U-2	302.37	362.79	20.16
U-3	295.03	362.40	17.52
U-4	276.37	361.96	14.75
U-5	276.57	362.24	12.13
U-6	266.94	362.54	9.28
M-1	306.68	363.06	23.29
M-2	301.40	362.09	20.46
M-3	296.07	361.45	17.93
M-4	283.68	361.49	15.1
M-5	279.37	362.23	12.7
M-6	280.19	361.56	9.00

Figure 7 and Table 4 show the TG curves and its data of nanocomposites, respectively. It can be seen that the temperature of maximum weight loss rate was nearly unchanged, while both the temperature at 5% weight loss and residual mass were gradually decreased with the increases of NCC or MNCC. These results may be originated from that the NCC or MNCC was fully decomposed to the end before 700ºC, but silica was still stable. The temperature at 5% weight loss as well as residual mass improved as the NCC modified. The reasons can be owing to the fine dispersion of filler and the intensive combination between rubber and filler. The increase of temperature at 5% weight loss may be due to the strong combination between NR and NCC, whereas the enhancement of residual mass is attributed to the increased combination between NR and silica. These results can also explain the previous conclusion: the heat build-up and permanent deformation are reduced as the increases of mechanical properties and the dynamic mechanical properties.

3.3. Micrographs of NCC suspension and in the nanocomposites

3.3.1. Micrographs of NCC and silica

Figure 8 shows the TEM micrographs of a dilute suspension of NCC and silica, the length of NCC

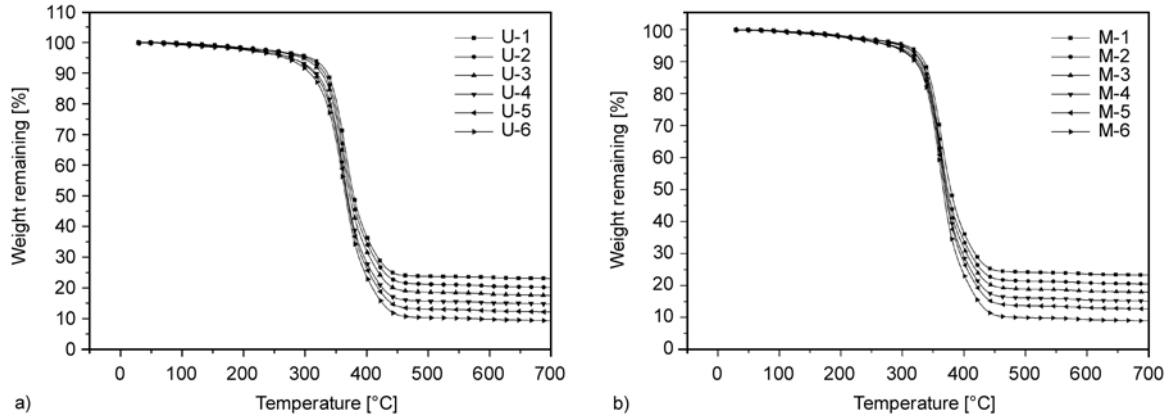

Figure 7. TG curves of NR/NCC/silica and NR/MNCC/silica nanocomposites

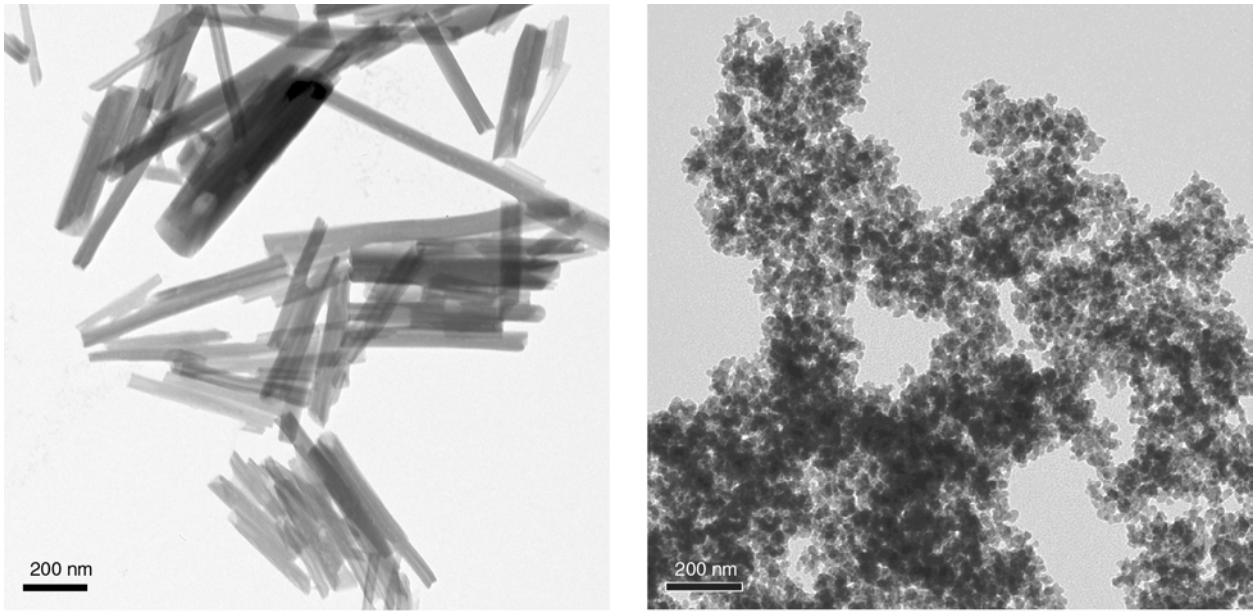

Figure 8. TEM micrographs of (a) NCC and (b) silica suspension

mostly for 300–600 nm, diameter was 40~60 nm. This confirm results observed by some scholars [32, 37]. Figure 8b shows that silica original size was below 100 nm, while the silica aggregates reach micro-scales in diameter. Therefore, comparing to silica, NCC aggregates can be easily separated due to the following two factors. Geometrically, the rod-like NCC aggregates are more easily dispersed than the spherial particles. Chemically, these are recognized as with low hydroxyl density on the surface compared with silica.

3.3.2. Morphology of NCC in the nanocomposites

Figure 9 shows the SEM photos for the stretch broken surface of the NR/NCC, NR/MNCC (0.3 phr KH550 per 10 phr NCC) and NR/MNCC/silica nanocomposites. It can be seen from pictures (a) and (c) that NCC aggregates gathered more seriously, distributed unevenly and lots of them were exposed on the NR matrix surface. There were obvious cracks due to pull out on the cross section, which was relatively smooth. On the contrary, as shown in the picture (b) and (d), MNCC aggregates gathered fewer, dispersed uniformly and most of them embedded in the NR matrix. There were no obvious pull out cracks, which was continuity of cracks. The same phenomenon was shown in pictures (e) and (f) with 10 phr MNCC replacing silica. These results indicated that the addition of MNCC reinforced the bonding between rubber matrix and filler and led to more firmly. Therefore, a very good comprehensive performance was reflected on the macro properties.

4. Conclusions

When NCC was modified by KH550, NR/MNCC/silica compounds showed an accelerated curing rate, reduced Payne effect and better processing performance. Tear strength, 300% modulus, hardness, heat build-up, compression set and dynamic mechanical performance of NR/MNCC/silica nanocomposites were greatly improved. MNCC and NR/silica compatibility was reinforced. Meanwhile, the apparent crosslinking density analysis, TGA, TEM and SEM images show the dispersion of in the matrix and interfacial strength of between MNCC and NR/silica nanocomposites was enhanced. In addition, a number of advantages such as renewable, biodegradable, broadly obtained, low density, low-cost and environmentally friendly, make NCC become a new energy saving filler to partly replace silica.

Acknowledgements

The authors would like to acknowledge the support of the National Natural Science Foundation of China (51173046).

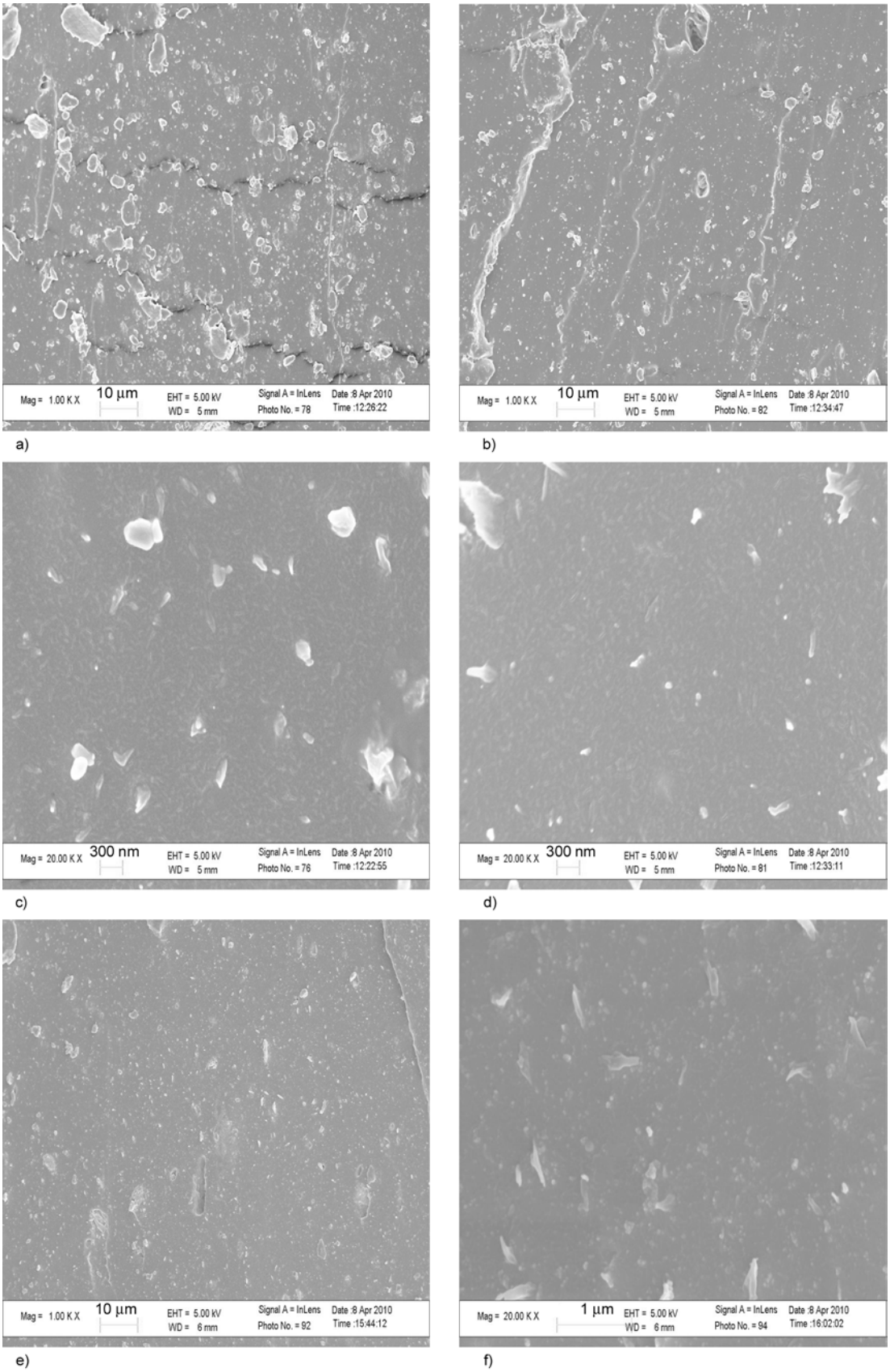

Figure 9. SEM micrographs of stretch broken surface of the (a, c) NR/NCC (100/10), (b, d) NR/MNCC (100/10) and (e, f) NR/MNCC/silica (100/10/20) nanocomposites

References

[1] Castellano M., Conzatti L., Costa G., Falqui L., Turturro A., Valenti B., Negroni F.: Surface modification of silica: 1. Thermodynamic aspects and effect on elastomer reinforcement. Polymer, 46, 695–703 (2005). DOI: 10.1016/j.polymer.2004.11.010

[2] Bokobza L., Chauvin J-P.: Reinforcement of natural rubber: Use of in situ generated silicas and nanofibres of sepiolite. Polymer, **46**, 4144–4151 (2005). DOI: 10.1016/j.polymer.2005.02.048

[3] Ansarifar A., Wang L., Ellis R. J., Haile-Meskel Y.: Using a silanized silica nanofiller to reduce excessive amount of rubber curatives in styrene-butadiene rubber. Journal of Applied Polymer Science, **119**, 922–928 (2011). DOI: 10.1002/app.32772

[4] Esch H., Goerl U., Kuhlmann R., Rausch R.: Precipitated silicas. European Patent 0647591, Germany (1995).

[5] Rattanasom N., Prasertsri S., Ruangritnumchai T.: Comparison of the mechanical properties at similar hardness level of natural rubber filled with various reinforcing-fillers. Polymer Testing, **28**, 8–12 (2009). DOI: 10.1016/j.polymertesting.2008.08.004

[6] Peng H., Liu L., Luo Y., Wang X., Jia D.: Effect of 3-propionylthio-1-propyltrimethoxylsilane on structure, mechanical, and dynamic mechanical properties of NR/silica composites. Polymer Composites, **30**, 955–961 (2009). DOI: 10.1002/pc.20640

[7] Stöckelhuber K. W., Das A., Jurk R., Heinrich G.: Contribution of physico-chemical properties of interfaces on dispersibility, adhesion and flocculation of filler particles in rubber. Polymer, **51**, 1954–1963 (2010). DOI: 10.1016/j.polymer.2010.03.013

[8] Qi Q., Wu Y., Tian M., Liang G., Zhang L., Ma J.: Modification of starch for high performance elastomer. Polymer, **47**, 3896–3903 (2006). DOI: 10.1016/j.polymer.2006.03.095

[9] Liu C., Shao Y., Jia D.: Chemically modified starch reinforced natural rubber composites. Polymer, **49**, 2176–2181 (2008). DOI: 10.1016/j.polymer.2008.03.005

[10] Favier V., Chanzy H., Cavaille J. Y.: Polymer nanocomposites reinforced by cellulose whiskers. Macromolecules, **28**, 6365–6367 (1995). DOI: 10.1021/ma00122a053

[11] Nair K. G., Dufresne A.: Crab shell chitin whisker reinforced natural rubber nanocomposites. 1. Processing and swelling behavior. Biomacromolecules, **4**, 657–665 (2003). DOI: 10.1021/bm020127b

[12] Nair K. G., Dufresne A.: Crab shell chitin whisker reinforced natural rubber nanocomposites. 2. Mechanical behavior. Biomacromolecules, **4**, 666–674 (2003). DOI: 10.1021/bm0201284

[13] Gu J., Li X-H., Jia D-M., Luo Y-F., Cheng R-S.: Reinforcement of natural cellulose whisker on natural rubber. Acta Polymerica Sinica, **7**, 595–598 (2007). DOI: 10.3724/SP.J.1105.2009.00595

[14] Bai W., Li K.: Partial replacement of silica with microcrystalline cellulose in rubber composites. Composites Part A: Applied Science and Manufacturing, **40**, 1597–1605 (2009). DOI: 10.1016/j.compositesa.2009.07.006

[15] Nair K. G., Dufresne A., Gandini A., Belgacem M. N.: Crab shell chitin whiskers reinforced natural rubber nanocomposites. 3. Effect of chemical modification of chitin whiskers. Biomacromolecules, **4**, 1835–1842 (2003). DOI: 10.1021/bm030058g

[16] Bendahou A., Kaddami H., Dufresne A.: Investigation on the effect of cellulosic nanoparticles' morphology on the properties of natural rubber based nanocomposites. European Polymer Journal, **46**, 609–620 (2010). DOI: 10.1016/j.eurpolymj.2009.12.025

[17] Samir M. A. S. A., Alloin F., Dufresne A.: Review of recent research into cellulosic whiskers, their properties and their application in nanocomposite field. Biomacromolecules, **6**, 612–626 (2005). DOI: 10.1021/bm0493685

[18] Eichhorn S. J., Dufresne A., Aranguren M., Marcovich N. E., Capadona J. R., Rowan S. J., Weder C., Thielemans W., Roman M., Renneckar S., Gindl W., Veigel S., Keckes J., Yano H., Abe K., Nogi M., Nakagaito A. N., Mangalam A., Simonsen J., Benight A. S., Bismarck A., Berglund L. A., Peijs T.: Review: Current international research into cellulose nanofibres and nanocomposites. Journal of Materials Science, **45**, 1–33 (2010). DOI: 10.1007/s10853-009-3874-0

[19] Ljungberg N., Bonini C., Bortolussi F., Boisson C., Heux L., Cavaillé J. Y.: New nanocomposite materials reinforced with cellulose whiskers in atactic polypropylene: Effect of surface and dispersion characteristics. Biomacromolecules, **6**, 2732–2739 (2005). DOI: 10.1021/bm050222v

[20] Ljungberg N., Cavaillé J-Y., Heux L.: Nanocomposites of isotactic polypropylene reinforced with rod-like cellulose whiskers. Polymer, **47**, 6285–6292 (2006). DOI: 10.1016/j.polymer.2006.07.013

[21] Berlioz S., Molina-Boisseau S., Nishiyama Y., Heux L.: Gas-phase surface esterification of cellulose microfibrils and whiskers. Biomacromolecules, **10**, 2144–2151 (2009). DOI: 10.1021/bm900319k

[22] Braun B., Dorgan J. R.: Single-step method for the isolation and surface functionalization of cellulosic nanowhiskers. Biomacromolecules, **10**, 334–341 (2009). DOI: 10.1021/bm8011117

[23] Goussé C., Chanzy H., Excoffier G., Soubeyrand L., Fleury E.: Stable suspensions of partially silylated cellulose whiskers dispersed in organic solvents. Polymer, **43**, 2645–2651 (2002). DOI: 10.1016/S0032-3861(02)00051-4

[24] Yuan H., Nishiyama Y., Wada M., Kuga S.: Surface acylation of cellulose whiskers by drying aqueous emulsion. Biomacromolecules, **7**, 696–700 (2006). DOI: 10.1021/bm050828j

[25] de Menezes A. J., Siqueira G., Curvelo A. A. S., Dufresne A.: Extrusion and characterization of functionalized cellulose whiskers reinforced polyethylene nanocomposites. Polymer, **50**, 4552–4563 (2009). DOI: 10.1016/j.polymer.2009.07.038

[26] Yi J., Xu Q., Zhang X., Zhang H.: Chiral-nematic self-ordering of rodlike cellulose nanocrystals grafted with poly(styrene) in both thermotropic and lyotropic states. Polymer, **49**, 4406–4412 (2008). DOI: 10.1016/j.polymer.2008.08.008

[27] Ljungberg N., Cavaillé J-Y., Heux L.: Nanocomposites of isotactic polypropylene reinforced with rod-like cellulose whiskers. Polymer, **47**, 6285–6292 (2006). DOI: 10.1016/j.polymer.2006.07.013

[28] Lu J., Askeland P., Drzal L. T.: Surface modification of microfibrillated cellulose for epoxy composite applications. Polymer, **49**, 1285–1296 (2008). DOI: 10.1016/j.polymer.2008.01.028

[29] Chang C., Duan B., Zhang L.: Fabrication and characterization of novel macroporous cellulose–alginate hydrogels. Polymer, **50**, 5467–5473 (2009). DOI: 10.1016/j.polymer.2009.06.001

[30] Cao X., Dong H., Li C. M.: New nanocomposite materials reinforced with flax cellulose nanocrystals in waterborne polyurethane. Biomacromolecules, **8**, 899–904 (2007). DOI: 10.1021/bm0610368

[31] Ten E., Turtle J., Bahr D., Jiang L., Wolcott M.: Thermal and mechanical properties of poly(3-hydroxybutyrate-*co*-3-hydroxyvalerate)/cellulose nanowhiskers composites. Polymer, **51**, 2652–2660 (2010). DOI: 10.1016/j.polymer.2010.04.007

[32] Wang N., Ding E., Cheng R.: The surface modification of nanocrystalline cellulose. Acta Polymerica Sinica, **8**, 982–987 (2006). DOI: 10.3724/SP.J.1105.2006.00982

[33] Liu L., Jia D., Luo Y., Guo B.: Preparation, structure and properties of nitrile–butadiene rubber–organoclay nanocomposites by reactive mixing intercalation method. Journal of Applied Polymer Science, **100**, 1905–1913 (2006). DOI: 10.1002/app.22614

[34] Haghighat M., Zadhoush A., Khorasani S. N.: Physicomechanical properties of α-cellulose–filled styrene–butadiene rubber composites. Journal of Applied Polymer Science, **96**, 2203–2211 (2005). DOI: 10.1002/app.21691

[35] Maridass B., Gupta B. R.: Effect of carbon black on devulcanized ground rubber tire–natural rubber vulcanizates: Cure characteri stics and mechanical properties. Journal of Elastomers and Plastics, **38**, 211–229 (2006). DOI: 10.1177/0095244306063480

[36] Wolff S., Wang M. J., Tan E. H.: Surface-energy of fillers and its effect on rubber reinforcement, 1. Kautschuk und Gummi Kunststoffe, **47**, 780–798 (1994).

[37] Bondeson D., Mathew A., Oksman K.: Optimization of the isolation of nanocrystals from microcrystalline cellulose by acid hydrolysis. Cellulose, **13**, 171–180 (2006). DOI: 10.1007/s10570-006-9061-4

eXPRESS Polymer Letters Vol.6, No.1 (2012) 26–40
Available online at www.expresspolymlett.com
DOI: 10.3144/expresspolymlett.2012.4

Shape-memory properties of magnetically active triple-shape nanocomposites based on a grafted polymer network with two crystallizable switching segments

*U. Narendra Kumar, K. Kratz, M. Behl, A. Lendlein**

Center for Biomaterial Development and Berlin-Brandenburg Center for Regenerative Therapies, Institute of Polymer Research, Helmholtz-Zentrum Geesthacht, Kantstr. 55, 14513 Teltow, Germany

Received 20 May 2011; accepted in revised form 19 July 2011

Abstract. Thermo-sensitive shape-memory polymers (SMP), which are capable of memorizing two or more different shapes, have generated significant research and technological interest. A triple-shape effect (TSE) of SMP can be activated e.g. by increasing the environmental temperature (T_{env}), whereby two switching temperatures (T_{sw}) have to be exceeded to enable the subsequent shape changes from shape (A) to shape (B) and finally the original shape (C).
In this work, we explored the thermally and magnetically initiated shape-memory properties of triple-shape nanocomposites with various compositions and particle contents using different shape-memory creation procedures (SMCP). The nanocomposites were prepared by the incorporation of magnetite nanoparticles into a multiphase polymer network matrix with grafted polymer network architecture containing crystallizable poly(ethylene glycol) (PEG) side chains and poly(ε-caprolactone) (PCL) crosslinks named CLEGC.
Excellent triple-shape properties were achieved for nanocomposites with high PEG weight fraction when two-step programming procedures were applied. In contrast, single-step programming resulted in dual-shape properties for all investigated materials as here the temporary shape (A) was predominantly fixed by PCL crystallites.

Keywords: *polymer composites, smart polymers, nanocomposites, shape-memory polymer, magnetically active polymer*

1. Introduction

Shape-memory polymers (SMP) and composites thereof belong to the class of actively moving polymers, which have the capability of storing one (dual-shape) [1–6], two (triple-shape) [7–13] or multiple (multiple-shape) [14] stable temporary shapes and recover their original or other temporary shapes when exposed to an external stimulus.
The field of SMP research has developed rapidly over the last years [6, 15–25] and it has become apparent that these functional polymers are motivating novel applications.
Thermo-sensitive SMP contain physical or chemical network-points, which determine their original shape, while each temporary shape is fixed by switching domains associated to a thermal transition temperature T_{trans}, that can be a glass transition (T_g) or a melting transition (T_m) [16, 17]. The process for programming of a temporary shape is called 'shape-memory creation procedure' (SMCP) and can be realized e.g. by deforming the material to an extension of ε_m at $T > T_{trans}$ and cooling to $T < T_{trans}$ while keeping the deformation, which then is fixed temporarily by solidification of the related set of switching domains [26]. The recovery of the original shape is named shape-memory effect (SME), which is typically induced by increasing the environmental temperature (T_{env}) [3, 5, 27, 28], where the shape changes

*Corresponding author, e-mail: andreas.lendlein@hzg.de

can be characterized by the switching temperature T_{sw} [26], that needs to be exceeded. Non contact initiation of SME was realized by irradiation with infrared light [29–31], applying radio-frequency (RF) [32], or an alternating magnetic field [4, 10, 33–36]. The magnetically triggered SME can be characterized by a specific switching magnetic field strength H_{sw}, which needs to be exceeded to induce the shape change [10]. The inductive heating capability of SMP composites is a result of energy absorption by the embedded magnetic particles from the alternating magnetic field, which is transformed into heat. Three different mechanisms of heat generation have to be considered; eddy current losses (which are a minor effect as e.g. magnetite has very low electrical conductivity), hysteresis losses (during reversal of magnetization), and rotational losses (related to rotation of magnetic moments relative to the surrounding described by Neel and Brownian effects) [37, 38].

In the current study, we explored, whether the shape-memory properties of triple-shape nanocomposites achieved by thermal and indirectly by magnetical stimulation of SME could be adjusted by variation of the applied programming protocols.

Magnetically-induced triple-shape nanocomposites, with different switching segment ratios and various nanoparticle contents (2.5, 5 and 10 wt%) were synthesized from crystallizable poly(ε-caprolactone) diisocyanatoethyl methacrylate (PCLDIMA; M_n = 8300 g·mol^{-1}, $T_{m,PCL}$ = 55°C), crystallizable poly(ethylene glycol) monomethyl ether monomethacrylate (PEGMA; M_n = 1000 g·mol^{-1}, $T_{m,PEG}$ = 38°C) and silica coated magnetite nanoparticles (SNP), named CLEGC, [39, 40] according to a procedure previously described in ref. [41]. The matrix material is a grafted polymer network structure based on covalently crosslinked PCL chains with grafted PEG side chains as previously reported [8, 42, 43]. Silica coated nanoparticles were chosen showing improved compatibility with the polymer matrix in comparison to uncoated fillers. To minimize changes in the surface to volume ratio (S/V) during shape recovery and thus ensuring precise control of the temperatures achieved for the nanocomposites during application of an alternating magnetic field, bending experiments were chosen for both thermal and indirect magnetical stimulation according to the method reported in ref. [10]. As it was demonstrated that a triple-shape effect could be achieved for multiphase AB polymer networks programmed by a one-step or two-step SMCP [44], here we want to investigate the influence of different SMCPs on the shape-memory properties of polymer network nanocomposites with grafted polymer network architecture.

2. Experimental section

2.1. Materials

The telechelic crosslinker poly(ε-caprolactone) diisocyanatoethyl dimethacrylate (PCLDIMA) was synthesized from poly(ε-caprolactone)diol (Solvay chemicals, Warrington, UK) with a number average molecular weight of M_n = 8.300 g·mol^{-1} and 2-isocyanatoethyl methacrylate (Sigma-Aldrich, Taufkirchen, Germany) according to the method described in ref. [10]. Poly(ethylene glycol) monomethyl ether monomethacrylate (PEGMA) (Polysciences, Warrington, PA, USA), benzyl peroxide (Sigma-Aldrich, Taufkirchen, Germany) and silica coated magnetite nanoparticles (AdNano MagSilica 50, Degussa, Hanau, Germany), mean aggregate size (photon correlation spectroscopy of an aqueous dispersion) was 90 nm, the mean domain size (X-ray diffraction) was 20–26 nm, and the domain content (X-ray fluorescence analysis) was 50–60 wt% were used as received.

2.1.1. Synthesis of polymer network nanocomposites

The nanocomposite preparation was following a method described in [41]. Here the synthesis is exemplarily described for CLEG040C05 containing 40 wt% of PCLDIMA relative to the organic components and a filler content of 5 wt% in the starting reaction mixture. A mixture of 2.8 g of PCLIDMA and 4.2 g of PEGMA were heated to 80°C, and then 0.37 g silica-coated nanoparticles were incorporated to the prepolymer melt by mechanical stirring. This mixture was kept at 80°C under vacuum for 30 min to remove volatile components, which could generate bubbles during polymerization. The polymerization was started thermally by decomposition of 10.6 mg benzyl peroxide, which was added under stirring. The reaction mixture is placed between two glass plates separated with a 1 mm thick PTFE spacer and kept at 80°C for 24 hours.

2.2. Methods

2.2.1. Swelling experiments

For evaluation of the crosslinking reaction, polymer network nanocomposites were extracted with chloroform and water. The gel content G was calculated according to Equation (1), as quotient of the mass of the extracted and dried films (m_d) to the mass of the original sample (m_c):

$$G = \frac{m_d}{m_c} \cdot 100\,\% \tag{1}$$

Additionally, the volumetric degree of swelling (Q), which is a measure for the crosslinking density of a polymer network, was calculated using Equation (2), determined from m_c and m_s and the specific densities of the solvent (ρ_s) and the network material (ρ_m):

$$Q = \left[1 + \frac{\rho_m}{\rho_s} \cdot \left(\frac{m_s}{m_c} - 1\right)\right] \cdot 100\,\% \tag{2}$$

2.2.2. Thermogravimetric analysis (TGA)

TGA experiments for determination of the incorporated amount of magnetite particles were performed on Netzsch TGA 204 Phoenix (Selb, Germany). All experiments were conducted with a constant heating rate of 20 K·min^{-1}. The network samples were heated from 25 to 500°C under N_2 atmosphere and then from 500 to 900°C under O_2 atmosphere. Temperature was kept constant for 2 min at 500°C.

2.2.3. Differential scanning calorimetry (DSC)

DSC experiments were performed on a Netzsch DSC 204 Phoenix (Netzsch, Selb, Germany). All experiments were conducted in the temperature range from –100 to 100°C with a constant heating and cooling rate of 10 K·min^{-1} and with a waiting period of 2 min at the maximum and minimum temperature. Melting and glass transition temperatures were determined from the second heating run. The overall heat of fusion ΔH_m as well as the partial heat of fusion $\Delta H_{m,PXX}$ representing the crystalline PCL and PEG phases respectively, which was calculated from ΔH_m and the weight fraction of PCL and PEG phase in the polymer network matrix, were averaged from DSC runs of three different samples.

2.2.4. Dynamic mechanical analysis at varied temperature (DMTA)

DMTA analysis was performed on a Gabo Eplexor 25 N (Gabo, Ahlden, Germany) using standard test specimen (ISO 527-2/1BB) punched from the polymer network films. All experiments were performed in temperature sweep mode with a constant heating rate of 2 K·min^{-1}. The oscillation frequency was 10 Hz. The network samples were investigated in an temperature interval from –100 to 100°C.

2.2.5. Tensile tests

Tensile tests at different temperatures (0, 40, 70°C and ambient temperature) were performed on Zwick Z 1.0 tensile testers (Zwick, Ulm, Germany) equipped with a thermo chamber and temperature controller (Eurotherm Regler, Limburg, Germany) using standard test specimen (ISO 527-2/1BB). In each experiment the strain rate was 5 mm·min^{-1}.

2.2.6. Shape-memory creation procedures

Bending of the nanocomposite samples (size: 30×2×1 mm^3) was performed using a custom built device. For controlled heating of the samples to T_{high} = 70°C and T_{mid} = 40°C a thermal oven VD 23 Vacuum Oven, type 21023200002000 (WTB Binder GmbH, Tuttlingen, Germany) was utilized, whereas for cooling to T_{low} = 0°C the freezer of a refrigerator comfort KT1430 (Liebherr, Ochsenhausen, Germany) was applied. A one-step programming (SMCP-1s) and two different two-step shape-memory creation procedures (SMCP-2s-I, SMCP-2s-II) were applied, which are schematically illustrated in Figure 1a. The molecular mechanism of the temporary shape fixation is schematically shown in Figure 1b.

SMCP-1s

The original straight samples (shape (C)) were heated to T_{high} = 70°C and deformed by bending to an angle of 180°, which was fixed afterwards by cooling to T_{low} = 0°C while the bending strain was kept constant. After a waiting period of 10 minutes, the external stain was removed and shape (A) was achieved.

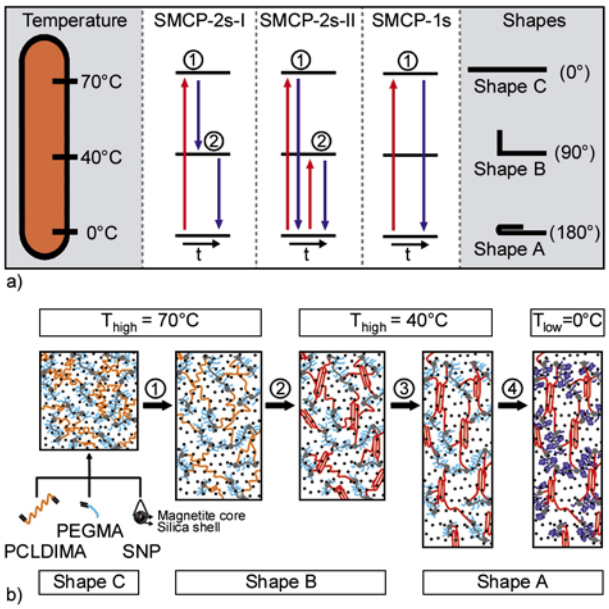

Figure 1. (a) Schematic representations of the different shape-memory creation procedures applied for bending of the nanocomposites. Two-step programming methods: SMCP-2s-I, SMCP-2s-II as well as single-step programming procedure SMCP-1s. (b) Molecular mechanism for graft polymer network composites during shape-memory creation procedure where the color indicating the different phases of the polymer segments. Orange: amorphous PCL chain segments, Light blue: amorphous PEG chain segments, Red: crystalline PCL chain segments, Dark blue: crystalline PEG chain segments, grey: amorphous poly(methacrylate) chain segments.

SMCP-2s-I

In step 1 the original sample was heated to T_{high} = 70°C and bent to an angle of 90°, which was fixed by cooling to T_{mid} = 40°C while keeping the bending strain. After a waiting period of 3 hours, the external strain was removed, and the shape (B) was obtained. Subsequent bending to 180° at T_{mid}, followed by cooling under bending strain to T_{low} = 0°C and equilibration at T_{low} resulted in shape (A) after removal of the strain.

SMCP-2s-II

First the sample was heated to T_{high} = 70°C and deformed by bending to an angle of 90°, which was fixed by cooling to T_{low} = 0°C while the bending strain was kept constant. After equilibration for 1 minute, the external strain was removed and step 1 was completed, while shape (B) was achieved. In step 2 the sample was heated to T_{mid} and bent to 180°, which was fixed by cooling to T_{low} = 0°C under keeping the bending strain. After equilibration at T_{low} the strain was removed to obtain shape (A).

2.2.7. Indirect magnetic heating experiments

Inductive heating of the nanocomposites samples was realized by positioning original and programmed nanocomposite samples in an alternating magnetic field at a frequency of f = 258 kHz. The experimental set-up consisted of a high-frequency generator (TIG 5/300; Huettinger Electronic, Freiburg, Germany), a water-cooled coil with 6 loops with a diameter of 4 cm, for application of magnetic field and an IR pyrometer (Metis MY84, Sensortherm; Frankfurt, Germany) for online non-contact measurement of the sample's surface temperature (T_{max}). By adjusting the generator power output the magnetic field strength H in the centre of the coil could be varied. The magnetically induced shape change was recorded with a digital compact camera (Canon PowerShot A460) and the change in recovery angle was determined with the help of the single photographs taken every 10 s.

Two different kinds of indirect magnetic heating experiments were conducted. In a first set of experiments the magnetic field strength was increased step-wise (≈1 kA·m^{-1}) from H_0 = 0 kA·m^{-1} to H = 29.4 kA·m^{-1} and from the obtained recovery curves H_{sw} was determined. In a second recovery experiment H was subsequently switched from H_0 to H_{mid} = 22.2 kA·m^{-1} and after a waiting period of 3 minutes H was again increased from H_{mid} = 22.2 kA·m^{-1} to H_{high} = 29.4 kA·m^{-1}.

2.2.8. Environmental heating experiments

Heating of nanocomposites was performed by utilization of a thermochamber equipped with a temperature controller (2216E for the Z005, Eurotherm Regler, Limburg, Germany). Heating in the thermochamber was realized by increasing T_{env} from 25 to 70°C with a heating rate of 3 K·min^{-1}, while T_{env} was measured by a Cu–CuNi thermocouple, which was placed close to the sample. The shape changes were recorded with a video camera (Canon Powershot A 460) and the recovery angle was determined with the help of single photographs taken at different T_{env}.

3. Results and discussion

3.1. Composition and morphology of the composites

CLEGC triple-shape nanocomposites with 30 to 70 wt% PCLDIMA in the starting material mixture of organic compounds and a nanoparticle content from 0, 2.5, 5 or 10 wt% SNP were synthesized by thermally initiated radical polymerization. The nomenclature of the different nanocomposites as well as the composition related results are given in Table 1.

The gel content G determined in swelling experiments by extraction with chloroform was used to quantify the yield of the crosslinking reaction. Constant high values for $G(CHCl_3)$ in the range around 92 to 96% were obtained for all materials independent from the network composition indicating an almost complete reaction. The obtained degree of swelling values $Q(CH_3Cl)$ and $Q(H_2O)$ decreased with increasing crosslinker content from 1020 to 890% and from 270 to 130%, respectively. The composition of the polymer network was confirmed by water extraction method according Equation (3), where $\omega_{PCL,initial}$ is the initial PCL-wt% in the starting composition and ω_{PCL} is the incorporated PCL-wt%, $G(H_2O)$ and $G(CHCl_3)$ are the gel content values determined in water and chloroform:

$$\omega_{PLC}=\left(\frac{\omega_{PLC,initial}-[G(H_2O)-G(CHCl_3)]}{G(CHCl_3)}\right)\cdot 100\,\% \quad (3)$$

The amount of incorporated SNP for the nanocomposites determined by thermo gravimetric analysis was found to be close to the initial incorporated amount. The distribution of the nanoparticles within the polymer matrices was investigated by means of SEM. The SEM micrographs obtained from cryo-microtomed cross sections of the nanocomposites confirmed a similar filler distribution for samples with 5 wt% SNP, independent from the composition of the polymer matrix.

3.2. Thermal and mechanical properties

The thermal properties of the networks were investigated by DSC and DMTA. The DSC thermograms of the CLEGC samples are shown in Figure 2. All CLEGC exhibited two distinct T_m, whereby the T_m

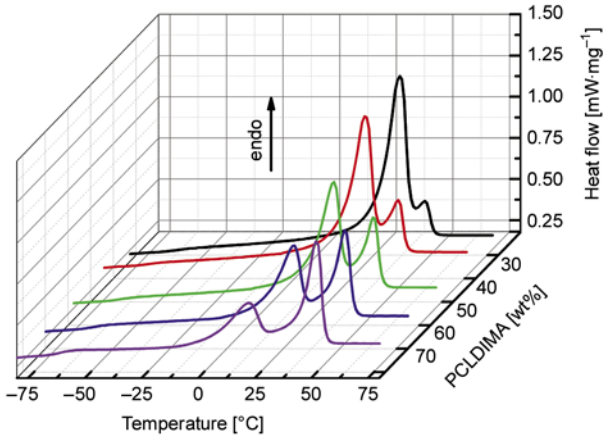

Figure 2. DSC thermograms for nanocomposites with different switching segment ratios and 5 wt% SNP content taken from the second heating run with a heating rate of 10 K·min^{-1}. CLEG(030)C05 (black line); CLEG(040)C05 (red line); CLEG(050)C05 (green line); CLEG(060)C05 (blue line); CLEG(070)C05 (pink line).

Table 1. Gel content G, swelling degree Q, SNP content and PCL content of CLEG nanocomposites and pure polymer networks

Sample ID[a]	G ($CHCl_3$)[b] [%]	Q ($CHCl_3$)[b] [%]	G (H_2O)[c] [%]	Q (H_2O)[c] [%]	SNP content[d] [wt%]	ω_{PCL}[e] [wt%]
CLEG(030)C05	94.1±0.7	1018±4	97.9±0.3	266±0	5.2±1.0	28±1
CLEG(040)C05	94.6±0.3	1007±5	97.6±1.0	211±1	5.2±0.4	39±1
CLEG(050)C05	94.2±0.3	991±8	98.2±0.6	173±0	5.1±0.4	49±1
CLEG(060)C05	92.0±0.4	998±8	97.4±0.5	148±2	5.1±0.3	60±1
CLEG(070)C05	92.5±0.1	954±2	99.0±1.2	131±2	5.0±0.3	69±1
CLEG(030)C00	93.5±1.2	974±18	96.6±0.2	272±3	–	29±1
CLEG(040)C00	94.4±0.2	947±3	97.6±0.4	213±1	–	38±1
CLEG(050)C00	93.9±0.0	938±4	98.0±0.7	174±2	–	49±1
CLEG(060)C00	93.2±0.3	913±14	98.4±0.8	147±1	–	59±1
CLEG(070)C00	93.0±0.6	888±7	99.3±0.7	128±1	–	69±1

[a]Sample ID: the three-digit number in brackets gives the weight content of PCLDIMA in the starting material mixture of the organic compounds in wt% and the last two digits represent the wt% of added nanoparticles (0, 2.5, 5, 10).

Gel content (G) and swelling degree (Q) determined by swelling experiment in [b]$CHCl_3$, [c]H_2O.

[d]Particle content in wt% determined by TGA.

[e]The weight content of PCL in the polymer network matrix determined by water extraction method.

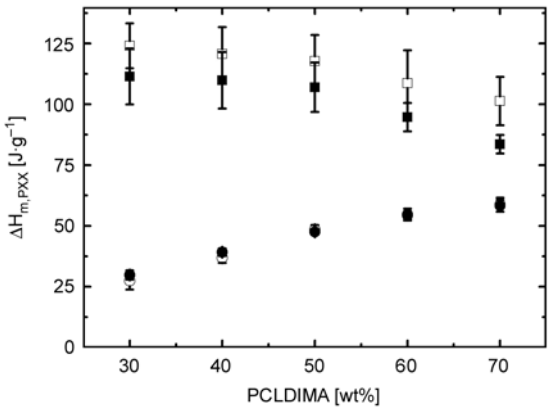

Figure 3. Partial heat of fusion ($\Delta H_{m,PXX}$) determined by DSC for crystalline PCL and PEG domains of nanocomposites and pure multiphase polymer networks. Nanocomposites: $\Delta H_{m,PEG}$ (solid squares); $\Delta H_{m,PCL}$ (solid circles); pure polymer networks: $\Delta H_{m,PEG}$, (open squares); $\Delta H_{m,PCL}$ (open circles).

at lower temperatures (20–40°C) can be related to the melting of the crystalline PEG phase ($T_{m,PEG}$) and at higher temperatures (≥50°C) to the melting of PCL crystallites ($T_{m,PCL}$). The $T_{m,PCL}$ remains constant at around 50°C, whereas $T_{m,PEG}$ was found to decrease with increasing switching segment content from 38 to 20°C for both nanocomposites and the pure networks. The overall heat of fusion ΔH_m was found to decrease with increasing PCL content from $\Delta H_m = 80\ J \cdot g^{-1}$ to $\Delta H_m = 64\ J \cdot g^{-1}$. While $\Delta H_{m,PEG}$ decreased with increasing switching segment content, $\Delta H_{m,PCL}$ was found to increase (Figure 3).

The storage modulus (E') vs. temperature curves obtained from DMTA analysis, are shown in Figure 4. The observed glass transition obtained as maximum of the tan δ versus temperature curve can be attributed to the amorphous PCL chains and was found in the range from –52 to –58°C for all composites. Both, pure polymer networks as well as nanocomposites, show a systematical decrease of the storage modulus E' with increasing temperature (Figure 4a). At temperatures above –50°C the values for E' decrease gradually to a level that is strongly dependent on the switching segment content, starting around 25°C. At 40°C above $T_{m,PEG}$ the storage modulus of the samples start to decrease sharply until the melting of the PCL crystallites is completed at around 60°C. Figure 4b shows that an incorporation of SNP of 2.5 to 10 wt% does not significantly alter the thermomechanical properties, whereby E' for composites with 5 and 10 wt% SNP was slightly higher.

Mechanical testing was performed by uniaxial tensile testing at four different temperatures (ambient temperature, $T_{high} = 70$°C; $T_{mid} = 40$°C and $T_{low} = 0$°C) and the obtained data are summarized in Figure 5 and Table 2. At 0°C, where PCL and PEG segments form crystalline as well as amorphous domains, the values of the Young's modulus decreased systematically with increasing switching segment content. This is related to the strong contribution of the crystalline PEG side chains to the overall mechanical properties below the onset of $T_{m,PEG}$ at 0°C (see Figure 2) which is in good agreement with results for $\Delta H_{m,PEG}$. For PEG contents in the range of 50–70 wt% the crystalline PEG domains dominate the overall mechanical proper-

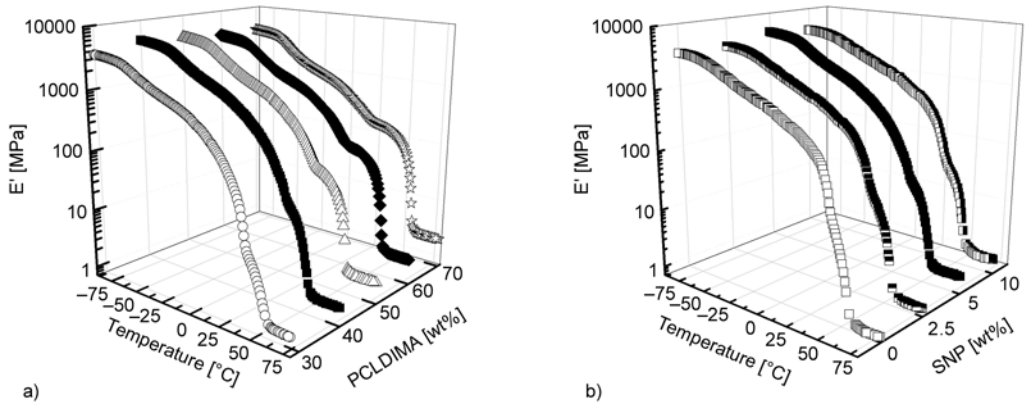

Figure 4. Storage modulus (E') versus temperature curves obtained for nanocomposites with different switching segment ratios by DMTA measurements. (a) nanocomposites differing in PCL content CLEG(30)C05 (open circles), CLEG(40)C05 (filled squares), CLEG(50)C05 (open triangles), CLEG(60)C05 (filled diamonds), CLEG(70)C05 (open stars), (b) nanocomposites prepared with 40 wt% PCLDIMA in the starting material mixture with different SNP content CLEG(40)C00 (open squares), CLEG(40)C02 (horizontally half-filled squares), CLEG(40)C05 (solid squares) and CLEG(40)C10 (vertically half-filled squares).

Table 2. Mechanical properties of pure CLEG polymer networks with various compositions at different temperatures (T_{high} = 70°C, T_{mid} = 40°C and T_{low} = 0°C).

Sample ID[a]	T_{high} = 70°C		T_{mid} = 40°C		T_{low} = 0°C	
	E [MPa]	ε_B [%]	E [MPa]	ε_B [%]	E [MPa]	ε_B [%]
CLEG(030)C00	0.49±0.01	100±30	4.2±0.2	100±30	430±50	7±4
CLEG(040)C00	0.70±0.02	100±30	14.7±0.6	120±60	420±20	50±30
CLEG(050)C00	0.87±0.01	100±30	31.1±1.5	170±60	310±30	120±90
CLEG(060)C00	1.05±0.03	150±10	46.5±2.1	240±10	130±20	200±60
CLEG(070)C00	1.23±0.03	160±20	62.7±10.4	270±20	160±10	240±90

[a]The three-digit numbers in parentheses given for the sample IDs are the content of PCLDIMA in the starting material mixture of the organic compounds in wt%, whereby C00 indicates that no nanoparticles were incorporated. Elongation at break (ε_B) and Young's Modulus (E) determined by tensile tests at different temperatures, T_{low} = 0°C, T_{mid} = 40°C and T_{high} = 70°C.

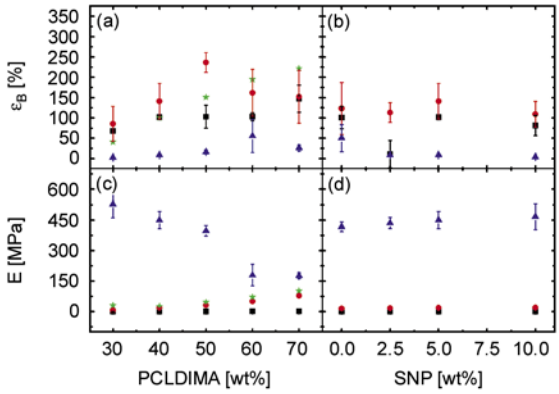

Figure 5. Mechanical properties of nanocomposites CLEG(XX)C05 with 5 wt% SNP depending on the PCLDIMA content in the starting material mixture and for CLEG(40)C with different SNP content determined by tensile tests at 0°C (blue triangles); 40°C (red circles); 70°C (black squares); ambient temperature (green stars). (a) Elongation at break ε_B for nanocomposites differing in PCL content; (b) Elongation at break ε_B for CLEG(40)C with different SNP content; (c) Young's modulus E for nanocomposites with different PCL content; (d) Young's modulus E for CLEG(40)C with different SNP content.

ties, while for the other compositions somehow a balance between PEG and PCL was reached. Therefore, the Young´s modulus decreased significantly with decreasing PEG content in the polymer network. The elongation at break ε_B at T_{low} = 0°C increased with increasing switching segment content, as the PCLDIMA content in the starting mixture is related to the number of covalent crosslinks in the polymer network. At T_{low} = 0°C both composites and pure networks exhibited almost similar mechanical properties. At ambient temperature, where some of the crystalline PEG domains are already molten, an increase in E and ε_B with increasing switching segment content could be observed, whereby the E values are significantly lower compared to T_{low} = 0°C. At 40°C the PEG phase was completely amorphous and the PCL phase still remained crystalline. Therefore the PEG phase could not contribute to the mechanical properties. At 70°C, which is above the melting temperature of both PEG and PCL, all samples are completely amorphous and only the covalent crosslinks introduced by PLCDIMA determine the overall mechanical behavior. While the incorporation of nanoparticles up to a content of 5 wt% did not significantly alter ε_B and E, for CLEG(040)C10 especially at 0°C higher values for the Young's modulus and lower ε_B-values were obtained, which we attribute to the higher filler concentration.

3.3. Magnetic heating experiments

Prior to the investigation of shape-memory properties a series of preliminary magnetic field experiments were conducted exemplarily for CLEG(040)C samples with different SNP content, where the maximal achievable temperature T_{max} was determined increasing H from H = 0 to H = 29.4 kA·m^{-1} at constant frequency of f = 258 kHz (details are given in the experimental section). For magnetic nanocomposites the specific absorption rate (SAR) or specific loss power is a key parameter, which is defined as the amount of heat released by a unit weight of the composite material per unit time [38, 40]. It was further reported that SAR is proportional to the observed temperature difference $\Delta T = T_{max} - T_{env}$, which can be correlated to the square of the magnetic field strength (H^2) (Equation (4)), where k is a material related constant, which depends on several factors (e.g. size and shape of the magnetic particles, their magnetic properties and the particle content or the heat conductivity of the composite) and the frequency f of the alternating mag-

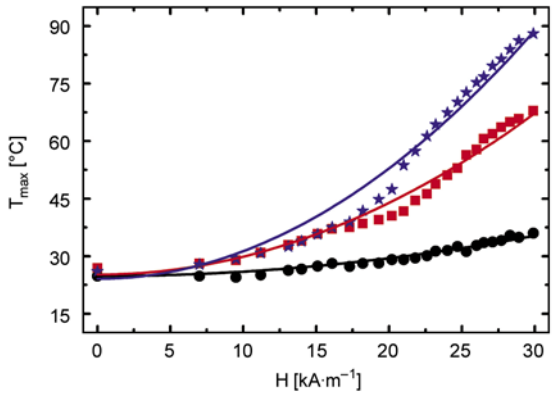

Figure 6. T_{max} achieved in magnetic heating experiments by continuously increasing H from $H = 0$ kA·m^{-1} to $H = 29.4$ kA·m^{-1} for CLEG(040)C with three different SNP contents; CLEG(040)C02 (black circles), CLEG(040)C05 (red squares) and CLEG(040)C10 (blue stars) and $T_{bulk} = k \cdot H^2 + <T_{env}>$ model analysis (solid lines)

netic field [38]. As in our case a constant frequency of $f = 258$ kHz was used and the investigated composites differ only in the amount of SNP.

$$SAR \cong \Delta T \cong k \cdot H^2 \quad (4)$$

As shown in Figure 6 the obtained T_{max} achieved by magnetic heating of the composites increased almost significantly with increasing the filler content and increasing H. At $H_{high} = 29.4$ kA·m^{-1} only for nanocomposites with 5 and 10 wt% SNP the required temperatures $T_{max} > T_{m,PCL}$ could be reached. CLEG(040)C05 was selected for performing magnetic recovery experiments, as the thermomechanical properties were almost similar to that of the pure polymer networks. In addition H required for indirect heating to $T_{mid} = T_{max} > T_{m,PEG} = 40$°C and $T_{high} = T_{max} > T_{m,PCL} = 70$°C were determined for CLEG(040)C05 to $H_{mid} = 22.2$ kA·m^{-1} and $H_{high} = 29.4$ kA·m^{-1}. The inserted model calculation based on Equation (4) showed that T_{max} correlated with H^2 as previously reported for other composite systems [38, 40]. Here it becomes apparent, that for CLEG(040)C02 the obtained data and the theoretical prediction of the model calculation were in good agreement, while CLEG(040)C05 and CLEG(040)C10 showed a significant deviation in the H-range of 15 kA·m^{-1} to $H = 22.4$ kA·m^{-1}, which might be related to the higher particle loading. The k values obtained by the model analysis were $k = 0.012$ K·m^2·kA^{-2} for CLEG(040)C02, $k = 0.047$ K·m^2·kA^{-2} for CLEG(040)C05 and $k = 0.072$ K·m^2·kA^{-2} for CLEG(040)C10.

3.4. Shape-memory properties

Bending experiments were performed for studying the shape-memory properties. Here three different thermomechanical shape-memory creation procedures were applied, the two-step creation procedures SMCP-2s-I and SMCP-2s-II as well as the single-step programming SMCP-1s (details are given in Experimental section). In Figure 1a the different SMCPs are presented schematically. In Figure 1b, the molecular mechanisms of the temporary shape fixation during SMCP-2s-I is shown schematically. The PCL phase is used for the fixation of the temporary shape B, the sample is deformed at 70°C (step 1), which leads to an orientation of the amorphous, flexible PCL chain segments. Cooling to 40°C results in a crystallization of PCL chain segments (step 2), so that the temporary shape (B) is fixed when the sample is unloaded. At 40°C, the elasticity of a sample is determined by remaining amorphous PCL chain segments, which can be oriented by applying a deforming stress. This allows further a deformation of the polymer network (step 3), cooling to 0°C leads to a crystallization of pendant PEG chain segments (step 4), leading to a fixation of the temporary shape A by the crystalline PEG phase.

Shape recovery experiments were conducted with programmed samples by increasing the environmental temperature T_{env} and application of two different indirect magnetic heating experiments: stepwise increasing of H and subsequently switching from H_0 to H_{mid} and from H_{mid} to H_{high} (for details see Experimental section).

For quantification of the shape-memory properties the change in deformation angle θ was measured during programming and recovery. The shape fixity ratios R_f(X→Y) were determined after completion of SMCP according to Equation (5), while the shape recovery ratios R_r(Y→X) were calculated according to Equation (6). Samples programmed with SMCP-1s were quantified by R_f(C→A) and R_r(A→C), whereas samples programmed by dual-step procedures are characterized by R_f(C→B), R_f(B→A) and the overall fixity ratio R_f(C→A), as well as the recovery ratios R_r(A→B), R_r(A→C).

Additionally, the change in bending angle $\Delta\theta_{rec}$ during recovery with temperature or H was analysed for determination of T_{sw} and H_{sw}.

$$R_f(X \rightarrow Y) = \frac{\theta_X - \theta_Y}{\theta_X^0 - \theta_Y} \quad (5)$$

$$R_r(Y \rightarrow X) = \frac{\theta_Y - \theta_X^{rec}}{\theta_Y - \theta_X} \quad (6)$$

3.4.1. Recovery by inductive magnetic heating

All CLEGC nanocomposites exhibited good shape-memory properties when activated in alternating magnetic field (see Table 3). An almost complete fixation of shape (B) by crystallization of PCL domains was achieved for all investigated materials independent of the applied SMCP. In contrast the R_f(B→A) obtained during two-step SMCPs was found to decrease with increasing PCL content from 99±3% to 73±3%, because the fixation of shape (A) was mainly supported by the grafted PEG chains. In all magnetic recovery experiments a complete total recovery R_r(A→C) was obtained, while the recovery of shape (B) decreased with increasing PCLDIMA content down to R_r(A→B) < 49%. Excellent triple-shape properties were obtained for the network compositions with 30, 40 and 50 wt% PCLDIMA content in the starting material mixture. Such composites exhibited R_r(A→B) values above 63% when SMCP-2s-I was applied and lower values of R_r(A→B) > 55% for SMCP-2s-II, which can be explained by an additional contribution to fixation of shape (A) caused by cold-drawing of the PCL crystallites during SMCP-2s-I. For nanocomposites programmed with SMCP-1s a complete fixation of the temporary shape (A) and recovery of the original shape (C) was observed. Moreover in Table 4 the shape-memory properties achieved for CLEGC programmed with different SMCPs in magnetic recovery experiments using subsequent switching from H_0 to H_{mid} to H_{high} are summarized.

To determine the switching magnetic field strength $H_{sw,1}$(A→B) and $H_{sw,2}$(B→C), inductive magnetic heating was conducted by step-wise increasing of H. As apparent from Figure 7a–c representing the $\Delta\theta_{rec}$ versus H curves depending on the PCLDIMA content, the obtained recovery behavior of the nanocomposites was strongly influenced by the composition of the polymer matrix and the applied SMCP. When SMCP-2s-I and SMCP-2s-II was applied, a distinct two-step change in $\Delta\theta_{rec}$ with increasing H was observed for materials with a PCLDIMA content ranging from 30 to 50 wt%, which is characteristic for triple-shape capability. $H_{sw,1}$(A→B) increased with decreasing PCLDIMA content, which we attribute to the changes in $T_{m,PEG}$ with composition of the polymer matrix as confirmed in DSC measurements. A further difference in $H_{sw,1}$(A→B) for CLEG(030)C05 and CLEG(040)C05 samples can be related to the difference in the two programming procedures. Here $H_{sw,1}$(A→B) ≈ 15 kA·m^{-1} was determined for samples programmed with SMCP-2s-II, while a higher $H_{sw,1}$(A→B) > 20 kA·m^{-1} was achieved by SMCP-2s-I. This difference in $H_{sw,1}$(A→B) can be related to the difference in the two programming procedures. In SMCP-2s-I shape (A) was fixed by PEG crystallites and 'low' melting PCL crystallites resulting in higher values for $H_{sw,1}$(A→B), whereas during SMCP-2s-II only PEG crystallites are responsible for fixation of shape (A), as previously reported for photo-crosslinked CLEG polymer networks [8, 43, 44]. For samples programmed by SMCP-2s-I $H_{sw,2}$(B→C) ≈ 25 kA·m^{-1} could be determined, while slightly lower values for $H_{sw,2}$(B→C) were obtained when SMCP-2s-II was applied. Here, the lower values observed for SMCP-2s-II programmed samples can be related to the contribution of 'low' melting PCL crystallites to the fixation of shape (B) at T_{low} = 0°C. When one-step programming SMCP-1s was used for programming, a single transition, which is characteristic for a dual-shape effect, was achieved for all nanocomposites in the $\Delta\theta_{rec}$–H curves with H_{sw} ≈ 23 kA·m^{-1}, because the temporary shape is predominantly fixed by PCL crystallites during SMCP-1s, while crystallization of the grafted PEG chains did contribute to the fixation of shape (A) [43, 44].

3.4.2. Recovery by environmental heating

In thermal recovery experiments, the shape-memory capability of CLEGC composites with different composition was investigated by increasing T_{env} from 25 to 70°C (for details see Experimental section). From the obtained $\Delta\theta_{rec}$ versus T_{env} curves $T_{sw,1}$(A→B) related to the shape change from A→B and $T_{sw,2}$(B→C) related to the shape change from B→C were determined. As apparent from Fig-

Table 3. Shape-memory properties of CLEGC determined in bending experiments either recovered by inductive magnetic heating (f = 258 kHz) or recovered by thermally heating by increasing T_{env} (T_{low} = 0°C, T_{mid} = 40°C, T_{high} = 70°C).

Sample ID*			Recovery by inductive magnetic heating						Recovery by environmental heating					
			R_f(C→B) [%]	R_f(B→A) [%]	R_r(A→B) [%]	R_r(A→C) [%]	H_{sw1}(A→B) [kA·m^{-1}]	H_{sw2}(B→C) [kA·m^{-1}]	R_f(C→B) [%]	R_f(B→A) [%]	R_r(A→B) [%]	R_r(A→C) [%]	$T_{sw,PEG}$ [°C]	$T_{sw,PCL}$ [°C]
Two-step programming	SMCP-2s-I	CLEG(030)C05	89±3	99±3	116±3	96±2	20.8±0.2	25.3±0.2	89±3	99±3	127±3	100±2	43±2	55±2
		CLEG(040)C05	100±3	93±3	132±4	100±2	22.7±0.2	25.8±0.2	100±3	98±3	123±3	100±2	44±2	54±2
		CLEG(050)C05	100±3	86±3	64±4	98±2	15.2±0.2	25.5±0.2	100±3	88±3	88±4	100±2	38±2	55±2
		CLEG(060)C05	100±3	82±3	60±4	97±2	14.6±0.2	25.7±0.2	100±3	64±3	59±5	99±2	33±2	55±2
		CLEG(070)C05	100±3	75±3	48±5	99±2	14.3±0.2	24.0±0.2	100±3	66±3	48±5	99±2	36±2	54±2
	SMCP-2s-II	CLEG(030)C05	100±3	96±3	75±3	96±2	15.6±0.2	22.9±0.2	100±3	100±3	82±3	100±2	37±2	51±2
		CLEG(040)C05	100±3	85±3	68±4	100±2	14.9±0.2	24.0±0.2	100±3	86±3	71±4	100±2	34±2	51±2
		CLEG(050)C05	100±3	82±3	56±4	99±2	14.9±0.2	25.3±0.2	100±3	76±3	63±4	100±2	31±2	51±2
		CLEG(060)C05	100±3	74±3	51±5	98±2	16.1±0.2	24.3±0.2	100±3	61±3	45±5	100±2	27±2	51±2
		CLEG(070)C05	100±3	73±3	39±5	98±2	17.2±0.2	24.5±0.2	100±3	56±3	30±6	100±2	33±2	51±2
Single-step programming	SMCP-1s	CLEG(030)C05	99±2#		–	99±2	22.0±0.2#		100±2#		–	100±2	51±2#	
		CLEG(040)C05	95±2#		–	99±2	23.4±0.2#		100±2#		–	100±2	51±2#	
		CLEG(050)C05	99±2#		–	99±2	23.7±0.2#		100±2#		–	100±2	51±2#	
		CLEG(060)C05	100±2#		–	98±2	23.1±0.2#		100±2#		–	100±2	51±2#	
		CLEG(070)C05	99±2#		–	98±2	23.2±0.2#		100±2#		–	100±2	54±2#	

*The three-digit numbers in parentheses given for the sample IDs are the content of PCLDIMA in the starting material mixture of the organic compounds in wt% and the last two digit of the sample ID represent the wt% of nanoparticles in the starting reaction mixture.

#represent the values determined from one-step programming protocol (C→A)

The errors denoted in the table, for the determined H_{sw} were estimated related by the accuracy of the adjustment of the magnetic filed strength ±1 kA·m^{-1}.

The errors denoted in the table, for the determined temperatures T_{sw} were estimated related by the accuracy of the temperature control in the incubator.

The errors denoted in the table, for R_f and R_r values are related to the accuracy of recovery angle determination (estimation: ±3°) and were calculated according error propagation rules.

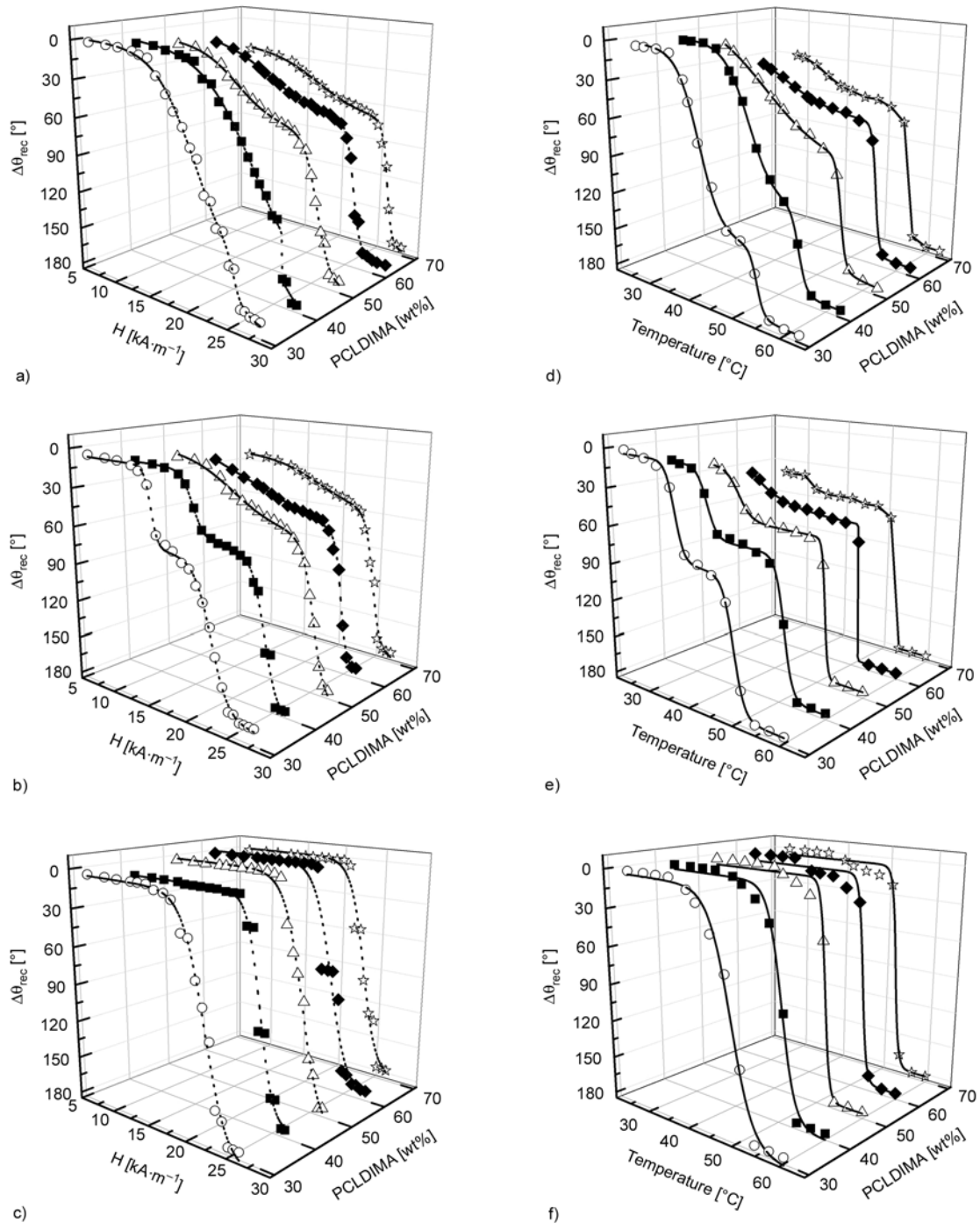

Figure 7. Recovery curves of CLEGC differing in switching segment ratio achieved for different programming procedures either under magnetic activation by step-wise increasing H from $H = 0$ to 29.4 kA·m^{-1} (a), (b), (c) and under thermal stimulation by step-wise increasing T_{env} from 25 to 70°C (d), (e), (f). Samples programmed with programming procedure SMCP-2s-I: (a and d), SMCP-2s-II: (b and e) and SMCP-1s: (c and f). CLEG(030)C05 (open circles); CLEG(040)C05 (filled squares); CLEG(050)C05 (open triangles); CLEG(060)C05 (filled diamonds); CLEG(070)C05 (open stars).

ure 7d–f also the recovery behavior of the nanocomposites, when thermally initiated, was strongly dependent on both the composition of the polymer matrix and the applied SMCP. A pronounced triple-shape behavior characterized by two well separated shape changes with T_{env} was achieved for all CLEGC composites with PCLDIMA content up to 50 wt% when programmed with SMCP-2s-I and SMCP-2s-II. The observed increase in $T_{sw,1}$(A→B) with decreasing PCLDIMA content could be attributed to the

Table 4. Shape-memory properties of CLEGC determined in inductive magnetic heating experiments where subsequently two different magnetic fields strength H_{mid} = 22.2 kA·m^{-1} and H_{high} = 29.4 kA·m^{-1} were applied (f = 258 kHz, T_{low} = 0°C, T_{mid} = 40°C, T_{high} = 70°C).

		Sample ID*	R_f(C→B) [%]	R_f(B→A) [%]	R_r(A→B) [%]	R_r(A→C) [%]
Two-step programming	SMCP-2s-I	CLEG(030)C05	89±3	94±3	99±3	100±2
		CLEG(040)C05	100±3	84±3	72±4	100±2
		CLEG(050)C05	100±3	80±3	63±4	100±2
		CLEG(060)C05	100±3	59±3	51±6	100±2
		CLEG(070)C05	100±3	56±3	46±6	100±2
	SMCP-2s-II	CLEG(030)C05	94±3	100±3	78±3	100±2
		CLEG(040)C05	97±3	77±3	69±4	100±2
		CLEG(050)C05	100±3	76±3	60±4	100±2
		CLEG(060)C05	100±3	54±3	41±6	100±2
		CLEG(070)C05	100±3	57±3	63±6	100±2
Single-step programming	SMCP-1s	CLEG(030)C05	100±2#		–	100±2
		CLEG(040)C05	100±2#		–	100±2
		CLEG(050)C05	100±2#		–	100±2
		CLEG(060)C05	100±2#		–	100±2
		CLEG(070)C05	100±2#		–	100±2

The errors denoted in the table, for R_f and R_r values are related to the accuracy of recovery angle determination (estimation: ±3°) and were calculated according error propagation rules.

*The three-digit numbers in parentheses given for the sample IDs are the content of PCLDIMA in the starting material mixture of the organic compounds in wt% and the last two digit of the sample ID represent the wt% of nanoparticles in the starting reaction mixture.

#represent the values determined from one-step programming protocol (C→A)

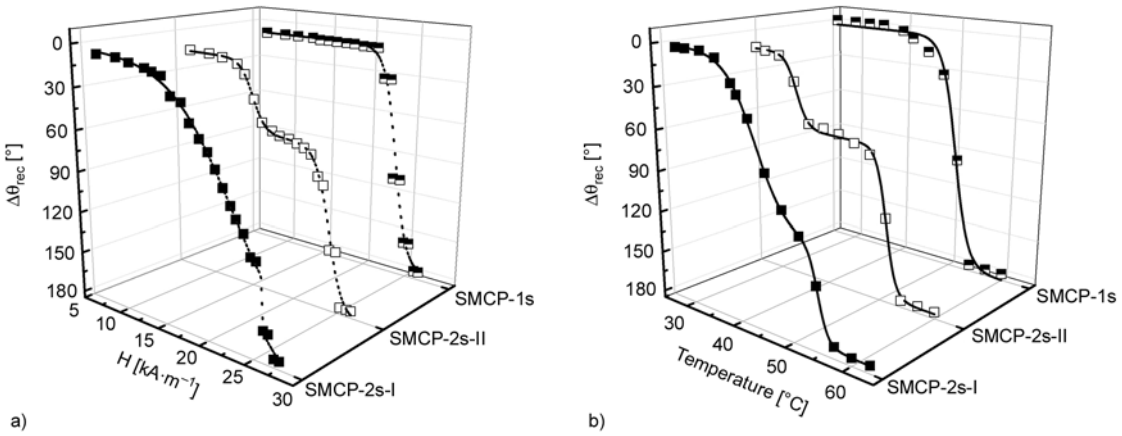

Figure 8. Comparison of thermally- and magnetically-stimulated recovery of CLEG(040)C05 after application of different programming procedures. SMCP-2s-I (filled squares); SMCP-2s-II (open squares); SMCP-1s (horizontally half-filled squares). (a) magnetic activation by step-wise increasing H from 0 to 29.4 kA·m^{-1} (b) step-wise increasing T_{env} from 25°C to 70°C.

changes in $T_{m,PEG}$ with composition of the polymer matrix as seen in DSC measurements. Whereby slightly higher values of $T_{sw,1}$(A→B) obtained for SMCP-2s-I could be related to the contribution of 'low' melting PCL crystallites during fixation of shape (A) as aforementioned. In contrast $T_{sw,2}$(B→C) was found to be independent from the composition of the polymer matrix, while application of SMCP-2s-I resulted in slightly higher values of $T_{sw,2}$(B→C) = 54°C, because the fixation of shape (B) is not supported by 'low' melting PCL crystallites. Finally, in Figure 8 the achieved environmental and magnetic recovery curves obtained for CLEG040C05 using different SMCPs are displayed to illustrate the aforementioned impact of the applied programming procedure on $T_{sw,1}$(A→B), $T_{sw,2}$(B→C), $H_{sw,1}$(A→B) and $H_{sw,2}$(B→C).

4. Conclusions

A series of CLEGC nanocomposites based on grafted polymer networks with various ratios of two crystallizable switching segments (PCL segments

acting as covalent crosslinker and grafted PEG segments) and different SNP contents from 2.5 to 10 wt% were synthesized. High values for gel content > 92% indicated an almost complete conversion of the starting materials. All nanocomposites exhibited two well separated thermal transitions, $T_{m,PCL}$ = 51°C attributed to the crystalline PCL domains and $T_{m,PEG}$ ranging from 38 to 20°C related to crystalline PEG domains, which decreased with increasing in PCL content. The incorporation of SNP up to 5 wt% did not significantly alter the thermomechanical properties of the grafted polymer network matrix.

The shape-memory properties of the nanocomposites were quantified by bending experiments using three different programming procedures, while activation of the thermally-induced shape effect was realized by indirect magnetic or environmental heating. The results achieved in the different heating experiments were in good accordance. Application of two-step programming procedures SMCP-2s-I and SMCP-2s-II resulted in a distinct triple-shape effect, whereby for nanocomposites with a PCLDIMA weight fraction of 30 and 40 wt% in the starting reaction mixture excellent triple-shape properties were obtained. In contrast, a pronounced dual-shape effect with an almost complete fixation and recovery were achieved when one-step programming was utilized, because here the temporary shape (A) in this case was predominantly fixed by PCL crystallites, while crystallization of the grafted PEG chains could not contribute to the fixation of shape (A). As for grafted polymer networks with two crystallizable switching segments the application of single-step programming did not lead to triple-shape capability. In a next step AB polymer networks with two crystallizable switching segments should be explored.

References

[1] Gall K., Dunn M. L., Liu Y., Finch D., Lake M., Munshi N. A.: Shape memory polymer nanocomposites. Acta Materialia, **50**, 5115–5126 (2002). DOI: 10.1016/S1359-6454(02)00368-3

[2] Kim B. K., Lee J. S., Lee Y. M., Shin J. H., Park S. H.: Shape memory behavior of amorphous polyurethanes. Journal of Macromolecular Science Part B: Physics, **40**, 1179–1191 (2001). DOI: 10.1081/MB-100107809

[3] Lendlein A., Langer R.: Biodegradable, elastic shape-memory polymers for potential biomedical applications. Science, **296**, 1673–1676 (2002). DOI: 10.1126/science.1066102

[4] Mohr R., Kratz K., Weigel T., Lucka-Gabor M., Moneke M., Lendlein A.: Initiation of shape-memory effect by inductive heating of magnetic nanoparticles in thermoplastic polymers. Proceedings of the National Academy of Sciences of the United States of America, **103**, 3540–3545 (2006). DOI: 10.1073/pnas.0600079103

[5] Tobushi H., Hayashi S., Ikai A., Hara H.: Thermomechanical properties of shape memory polymers of polyurethane series and their applications. Journal De Physique IV, **6**, 377–384 (1996). DOI: 10.1051/jp4:1996136

[6] Vaia R., Baur J.: Adaptive composites. Science, **319**, 420–421 (2008). DOI: 10.1126/science.1152931

[7] Behl M., Lendlein A.: Triple-shape polymers. Journal of Materials Chemistry, **20**, 3335–3345 (2010). DOI: 10.1039/B922992b

[8] Bellin I., Kelch S., Langer R., Lendlein A.: Polymeric triple-shape materials. Proceedings of the National Academy of Sciences of the United States of America, **103**, 18043–18047 (2006). DOI: 10.1073/pnas.0608586103

[9] Luo X., Mather P. T.: Triple-shape polymeric composites (TSPCs). Advanced Functional Materials, **20**, 2649–2656 (2010). DOI: 10.1002/adfm.201000052

[10] Narendra Kumar U., Kratz K., Wagermaier W., Behl M., Lendlein A.: Non-contact actuation of triple-shape effect in multiphase polymer network nanocomposites in alternating magnetic field. Journal of Materials Chemistry, **20**, 3404–3415 (2010). DOI: 10.1039/b923000a

[11] Pretsch T.: Durability of a polymer with triple-shape properties. Polymer Degradation and Stability, **95**, 2515–2524 (2010). DOI: 10.1016/j.polymdegradstab.2010.07.037

[12] Xie T., Xiao X., Cheng Y-T.: Revealing triple-shape memory effect by polymer bilayers. Macromolecular Rapid Communications, **30**, 1823–1827 (2009). DOI: 10.1002/marc.200900409

[13] Zotzmann J., Behl M., Hofmann D., Lendlein A.: Reversible triple-shape effect of polymer networks containing polypentadecalactone- and poly(ε-caprolactone)-segments. Advanced Materials, **22**, 3424–3429 (2010). DOI: 10.1002/adma.200904202

[14] Kolesov I. S., Radusch H-J.: Multiple shape-memory behavior and thermal-mechanical properties of peroxide cross-linked blends of linear and short-chain branched polyethylenes. Express Polymer Letters, **2**, 461–473 (2008). DOI: 10.3144/expresspolymlett.2008.56

[15] Kim B. K.: Shape memory polymers and their future developments. Express Polymer Letters, **2**, 614 (2008). DOI: 10.3144/expresspolymlett.2008.73

[16] Behl M., Razzaq M. Y., Lendlein A.: Multifunctional shape-memory polymers. Advanced Materials, **22**, 3388–3410 (2010). DOI: 10.1002/adma.200904447

[17] Behl M., Zotzmann J., Lendlein A.: Shape-memory polymers and shape-changing polymers. Advances in Polymer Science, **226**, 1–40 (2010). DOI: 10.1007/12_2009_26

[18] Hu J., Chen S.: A review of actively moving polymers in textile applications. Journal of Materials Chemistry, **20**, 3346–3355 (2010). DOI: 10.1039/b922872a

[19] Huang W. M., Ding Z., Wang C. C., Wei J., Zhao Y., Purnawali H.: Shape memory materials. Materials Today, **13**, 54–61 (2010). DOI: 10.1016/S1369-7021(10)70128-0

[20] Lendlein A., Behl M., Hiebl B., Wischke C.: Shape-memory polymers as a technology platform for biomedical applications. Expert Review of Medical Devices, **7**, 357–379 (2010). DOI: 10.1586/ERD.10.8

[21] Liu Y., Lv H., Lan X., Leng J., Du S.: Review of electro-active shape-memory polymer composite. Composites Science and Technology, **69**, 2064–2068 (2009). DOI: 10.1016/j.compscitech.2008.08.016

[22] Madbouly S. A., Lendlein A.: Shape-memory polymer composites. Shape-Memory Polymers, **226**, 41–95 (2010). DOI: 10.1007/12_2009_28

[23] Mather P. T., Luo X., Rousseau I. A.: Shape memory polymer research. Annual Review of Materials Research, **39**, 445–471 (2009). DOI: 10.1146/annurev-matsci-082908-145419

[24] Ratna D., Karger-Kocsis J.: Recent advances in shape memory polymers and composites: A review. Journal of Materials Science, **43**, 254–269 (2008). DOI: 10.1007/s10853-007-2176-7

[25] Gunes I. S., Jana S. C.: Shape memory polymers and their nanocomposites: A review of science and technology of new multifunctional materials. Journal of Nanoscience and Nanotechnology, **8**, 1616–1637 (2008). DOI: 10.1166/jnn.2008.038

[26] Wagermaier W., Kratz K., Heuchel M., Lendlein A.: Characterization methods for shape-memory polymers. Advances in Polymer Science, **226**, 1–49 (2010). DOI: 10.1007/12_2009_25

[27] Hayashi S.: Properties and applications of polyurethane-series shape memory polymer. in 'International progress in urethanes, Vol. 6' (eds.: Ashida K., Frisch K. C.) CRC Press, Boca Raton, 90–115 (1993).

[28] Huang W. M., Yang B., Zhao Y., Ding Z.: Thermo-moisture responsive polyurethane shape-memorypolymer and composites: A review. Journal of Materials Chemistry, **20**, 3367–3381 (2010). DOI: 10.1039/b922943d

[29] Koerner H., Price G., Pearce N. A., Alexander M., Vaia R. A.: Remotely actuated polymer nanocomposites–stress-recovery of carbon-nanotube-filled thermoplastic elastomers. Nature Materials, **3**, 115–120 (2004). DOI: 10.1038/nmat1059

[30] Leng J., Zhang D., Liu Y., Yu K., Lan X.: Study on the activation of styrene-based shape memory polymer by medium-infrared laser light. Applied Physics Letters, **96**, 111905/1–111905/3 (2010). DOI: 10.1063/1.3353970

[31] Maitland D. J., Wilson T., Schumann D. L., Baer G.: Laser-activated shape memory polymer microactuators for treating stroke. in 'Lasers and Electro-Optics Society, 2002. LEOS 2002. The 15th Annual Meeting of the IEEE, Glasgow, UK' Vol 1, 359–360 (2002). DOI: 10.1109/LEOS.2002.1134078

[32] Hazelton C. S., Arzberger S. C., Lake M. S., Munshi N. A.: RF actuation of a thermoset shape memory polymer with embedded magnetoelectroelastic particles. Journal of Advanced Materials, **39**, 35–39 (2007).

[33] Buckley P. R., McKinley G. H., Wilson T. S., Small W., Benett W. J., Bearinger J. P., McElfresh M. W., Maitland D. J: Inductively heated shape memory polymer for the magnetic actuation of medical devices. IEEE Transactions on Biomedical Engineering, **53**, 2075–2083 (2006). DOI: 10.1109/TBME.2006.877113

[34] Vialle G., Di Prima M., Hocking E., Gall K., Garmestani H., Sanderson T., Arzberger S. C.: Remote activation of nanomagnetite reinforced shape memory polymer foam. Smart Materials and Structures, **18**, 115014/1–115014/10 (2009). DOI: 10.1088/0964-1726/18/11/115014

[35] Yu X., Zhou S., Zheng X., Guo T., Xiao Y., Song B.: A biodegradable shape-memory nanocomposite with excellent magnetism sensitivity. Nanotechnology, **20**, 235702/1–235702/9 (2009). DOI: 10.1088/0957-4484/20/23/235702

[36] Zheng X., Zhou S., Xiao Y., Yu X., Li X., Wu P.: Shape memory effect of poly(D,L-lactide)/Fe_3O_4 nanocomposites by inductive heating of magnetite particles. Colloids and Surfaces B: Biointerfaces, **71**, 67–72 (2009). DOI: 10.1016/j.colsurfb.2009.01.009

[37] Razzaq M. Y., Anhalt M., Frormann L., Weidenfeller B.: Thermal, electrical and magnetic studies of magnetite filled polyurethane shape memory polymers. Materials Science and Engineering: A, **444**, 227–235 (2007). DOI: 10.1016/j.msea.2006.08.083

[38] Lao L. L., Ramanujan R. V.: Magnetic and hydrogel composite materials for hyperthermia applications. Journal of Materials Science: Materials in Medicine, **15**, 1061–1064 (2004).
DOI: 10.1023/B:JMSM.0000046386.78633.e5

[39] Pacull J., Gonçalves S., Delgado Á. V., Durán J. D. G., Jiménez M. L.: Effect of polar interactions on the magnetorheology of silica-coated magnetite suspensions in oil media. Journal of Colloid and Interface Science, **337**, 254–259 (2009).
DOI: 10.1016/j.jcis.2009.04.083

[40] Weigel T., Mohr R., Lendlein A.: Investigation of parameters to achieve temperatures required to initiate the shape-memory effect of magnetic nanocomposites by inductive heating. Smart Materials and Structures, **18**, 025011/1–025011/23 (2009).
DOI: 10.1088/0964-1726/18/2/025011

[41] Narendra Kumar U., Kratz K., Behl M., Lendlein A.: Triple-shape capability of thermo-sensitive nanocomposites from multiphase polymer networks and magnetic nanoparticles. Materials Research Society Proceedings, **1190**, 55–61 (2009).
DOI: 10.1557/PROC-1190-NN03-21

[42] Behl M., Bellin I., Kelch S., Wagermaier W., Lendlein A.: One-step process for creating triple-shape capability of AB polymer networks. Advanced Functional Materials, **19**, 102–108 (2009).
DOI: 10.1002/adfm.200800850

[43] Wagermaier W., Zander T., Hofmann D., Kratz K., Narendra Kumar U., Lendlein A.: In situ X-ray scattering studies of poly(ε-caprolactone) networks with grafted poly(ethylene glycol) chains to investigate structural changes during dual- and triple-shape effect. Macromolecular Rapid Communications, **31**, 1546–1553 (2010).
DOI: 10.1002/marc.201000122

[44] Bellin I., Kelch S., Lendlein A.: Dual-shape properties of triple-shape polymer networks with crystallizable network segments and grafted side chains. Journal of Materials Chemistry, **17**, 2885–2891 (2007).
DOI: 10.1039/b702524f

eXPRESS Polymer Letters Vol.6, No.1 (2012) 41–53
Available online at www.expresspolymlett.com
DOI: 10.3144/expresspolymlett.2012.5

A simple approach for synthesis, characterization and bioactivity of bovine bones to fabricate the polyurethane nanofiber containing hydroxyapatite nanoparticles

F. A. Sheikh[1], M. A. Kanjwal[2], J. Macossay[1], N. A. M. Barakat[3], H. Y. Kim[3]*

[1]Department of Chemistry, University of Texas Pan American, Edinburg, TX 78539, USA
[2]Technical University of Denmark, DTU Food, Soltofts Plads, B 227. 2800. Kgs. Lyngby, Denmark
[3]Department of Textile Engineering, Chonbuk National University, Jeonju 561-756, Republic of Korea

Received 1 June 2011; accepted in revised form 26 July 2011

Abstract. In the present study, we had introduced polyurethane (PU) nanofibers that contain hydroxyapatite (HAp) nanoparticles (NPs) as a result of an electrospinning process. A simple method that does not depend on additional foreign chemicals had been employed to synthesize HAp NPs through the calcination of bovine bones. Typically, a colloidal gel consisting of HAp/PU had been electrospun to form nanofibers. In this communication, physiochemical aspects of prepared nanofibers were characterized by FE-SEM, TEM and TEM-EDS, which confirmed that nanofibers were well-oriented and good dispersion of HAp NPs, over the prepared nanofibers. Parameters, affecting the utilization of the prepared nanofibers in various nano-biotechnological fields have been studied; for instance, the bioactivity of the produced nanofiber mats was investigated while incubating in simulated body fluid (SBF). The results from incubation of nanofibers, indicated that incorporation of HAp strongly activates the precipitation of the apatite-like particles, because of the HAp NPs act as seed, that accelerate crystallization of the biological HAp from the utilized SBF.

Keywords: *biocompatible polymers, biocompatible polymers, nanomaterials*

1. Introduction

Hydroxyapatite (HAp) is the main inorganic solid component of the hard tissues in bones and can also be used as a vital implant component, because of its excellent biocompatibility, bioactivity, nonimmunogenicity and osteoconductive nature [1]. The scientific community is facing a major challenge to formulate an ideal strategy to form new bone tissue for patients suffering from various bone defects. Thus, a significant amount of attention had been focused on different ways to produce HAp, so as to meet the world-wide requirements of these important biomaterials [2–4]. However, HAp cannot be used directly as an implant because of its free powder-like nature or needle-like particles which hinders its densification, resulting in brittle films, which therefore, make it difficult to process [5]. It is worth mentioning, that scaffolds used in tissue engineering should have good mechanical support, which eventually should transfer stress back to the healing tissue; and this process is difficult to achieve with HAp alone. Therefore, nano-sized composites of biodegradable polymers and HAp NPs are being developed to improve the mechanical properties, biodegradability, and the tissue interaction for artificial implants.

Since the advent of tissue engineering, HAp has been widely utilized for bone tissue regeneration, especially in the form of scaffolds. HAp has also been used frequently to meet specific requirements,

*Corresponding author, e-mail: sheikhfa@utpa.edu

such as a suitable environment to facilitate cell seeding and proper diffusion of nutrients for healthy growth of osteoblasts during the initial implant period, which is considered to be a crucial time [6]. For this aesthetic purpose, the most common strategy employed is to utilize the properties of web-like structures made from biodegradable polymers fabricated by electrospinning of polymers [7]. This electrospinning technique had been the focus of considerable attention, because it can produce fibers with diameters in the range of a few microns to the nanometer scale by applying high electric fields [8–9]. In a typical electrospinning process, the electrostatically driven polymer jet is ejected from the polymer solution, which experiences bending instability. Furthermore, the solvent evaporates and ultra fine stretched fibers are deposited on the grounded collector [10]. Nanofibers generated with this technique have drawn a considerable attention, because of their web-like structures, which exactly mimics the topology of the extracellular matrix present in the human body; thus, these nanofiber mats provide a favorable environment for growth of new tissues [10–11].

Polyurethane (PU) is a thermoplastic polymer with excellent mechanical properties and is insoluble in water; moreover, it can be used as a biomaterial [12–13]. A nano-fibrous shape strongly modifies the characteristics of any polymer, to make it utilizable for proper area of use. Therefore, polymer nanofibers of PU have also been utilized in various fields: biosensors, protective cloths, and epithelial enhancing material [14–16]. Thus, given the advantageous features of electrospinning, there are some reports that use this versatile technique to form nanofibers consisting of HAp. For instance, various polymers, such as poly (DL-lactide-co-glycolide), polycaprolactone, collagen and chitosan, have been produced by blending HAp NPs [17–20]. However, to our knowledge, there is no prior report that addresses production of biologically safe HAp produced by using high temperature sintering and mechanically strong polymer (PU) to form nanofibers as a future implants. Given these facts, the present work deals with production of PU nanofibers containing HAp NPs that are successfully produced using the electrospinning technique. In addition to morphological properties and the crystalline structure of nanofiber matrices, the bioactivity of obtained nanofibers was also investigated.

It is worth in mentioning, that chemically synthesized HAp nanopowder (particle size almost <50 nm) was utilized in the aforementioned polymer/HAp nanofiber mats to facilitate the electrospinning process; thus, the HAp NPs were imprisoned in the obtained polymer nanofibers [17–20]. Similarly, some researchers have focused on hydrogen bonding and improving the shape memory effect by adding HAp NPs in poly (D,L-lactide) nonocomposites [21, 22]. However, the bioactivity has not been investigated for those reported nanofiber mats or nanocomposites. We think the main reason is the complete encapsulation of the HAp NPs inside the polymer nanofibers or nanocomposites, which reveals no difference between the pristine and HAp-incorporated composites, when subjected to the simulated body fluid (SBF). In addition to this, some researchers have modified polymers, such as gelatin, polycaprolactone, and poly (D,L-lactide) acid, with the precursor materials of HAp; however, the final cell culture results were not well acceptable [23–26]. We believe that the materials used to form HAp were chemically contaminated, because there syntheses processes requires harsh chemicals, therefore, these materials did not reveal good results after the osteoblast culture [23–26]. In this study, we have utilized the HAp that was obtained from calcination of bovine bone, which is economically and environmentally preferable and biologically safe compared with the chemically synthesized one, which might be chemically contaminated as detailed in our previous studies [27–28]. Moreover, it is worthy to mention, that obtained HAp NPs used in this study had been obtained from the high temperature sintering of (850°C), which leads to cause denaturation of all antigenic proteins associated from their natural bovine origin, therefore rendering the product safe for the implant applications. Moreover, the particle size of the utilized HAp was relatively in broad size range, which demonstrates HAp NPs alone in/on PU nanofibers can be associated. Therefore, the introduced PU/HAp nanofiber mats revealed better bioactivity compared with the pristine mats, while incubation in SBF. Moreover, incubation of the introduced PU/HAp in the SBF led to the formation of excessive apatite, because of the

biological apatite crystallization, which causes the incorporated HAp particles in the nanofiber mats to act as nuclei, so as to lead the formation of these excessive apatites. Furthermore, detailed further study of these nanofibers in presence of osteoblast cells for checking cell viability are in progress.

2. Experimental work

2.1. Materials

Polyurethane (PU), ChronoFlex® MW of 110.000, medical grade was purchased from Cardio Tech. Intern., Japan. Tetrahydrofuran (THF) and *N,N*-dimethylformamide (DMF) (analytical grade, Showa Chemicals Ltd., Japan) were used as solvents without further purification.

2.2. Preparation of HAp NPs

Preparation of HAp NPs was done according to our previously established methodologies [25, 26]. In general, bone is 65–70% of HAp and 30–35% organic compounds (on a dry weight basis). Collagen is the main organic compound present in natural bone (95%); in addition, there are other organic compounds that exist in small concentrations, such as chondroitin sulfate, keratin sulfate and lipids (e.g., phospholipids, triglycerides, fatty acids and cholesterol) [29]. Keeping in consideration, the aforementioned compounds present in bones, the bovine bones taken from the femur of Egyptian cows were carefully washed with water and acetone to remove the solid impurities and other fats associated with them. After washing, the bones were dried at 160°C for 48 h. The cleaned bones were ground to particle sizes less than 100 μm. The ground bones were placed in an open alumina crucible and then heated in the furnace (Lenton Thermal Designs Ltd., South Korea). The ground bone sample was heated to 850°C at a heating rate of 10°C/min with a soaking time of 1 h. The obtained calcined bone powder was further ground with ball milling to decrease the particle size down to nano-scale level.

2.3. Electrospinning process

10 wt% of PU solution was prepared by dissolving PU in THF and DMF. Initially, PU pellets were dissolved overnight in THF, and DMF was added to produce the final concentration that contained 10 wt% of PU in THF/DMF (1:1, w/w). To prepare the colloidal solutions containing HAp, a stepwise

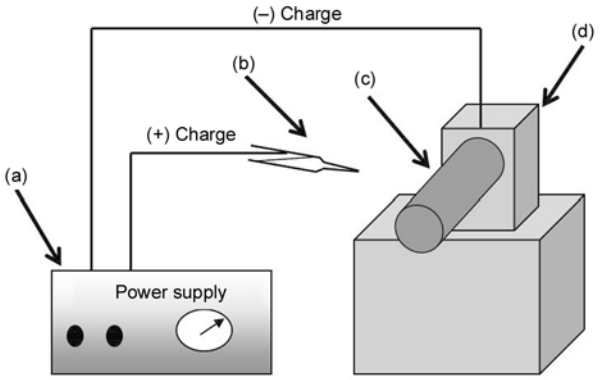

Figure 1. Schematic diagram of a simple electrospinning spinning apparatus: (a) dc power supply (b) Syringe (e) Rotating collector (d) Electric motor

methodology was adopted. Briefly, the colloidal of HAp/DMF were prepared and added to the previously prepared PU solution in THF to have final mixtures containing 3, 5 and 7 wt% of HAp with respect to the polymer concentration and with a final polymer concentration of 10 wt% of PU in THF/DMF (1:1, w/w). Figure 1 shows conceptual illustration for the used electrospinning set-up. A high voltage power supply (CPS-60 K02V1, Chungpa EMT Co., Republic of Korea) that is capable of generating voltages up to 60 kV was used as the electric field source for spinning of nanofibers. Polymer solutions to be electrospun were supplied through a glass syringe attached to a capillary tip. The wire originating from the positive electrode (anode), which was connected with the copper pin, was inserted into the colloidal solution, and a negative electrode (cathode) was attached to the rotating metallic collector. Finally, the solutions were electrospun at 15 kV with a 15 cm working distance (the distance between the needle tip and the collector). The as-spun nanofibers were dried *in vacuo* for 24 h in the presence of P_2O_5 to remove the residual moisture from used solvents.

2.4. *In-vitro* bioactivity test

To verify the advantage of incorporating HAp NPs in PU nanofibers, *in-vitro* bioactivity of both of pristine PU and PU/HAp nanofiber mats had been examined. Briefly, the *in-vitro* bioactivity study was performed using SBF solution, which was prepared by using the method described elsewhere [30]. The salt components, like NaCl, $NaHCO_3$, KCl, K_2HPO_4, $MgCl_2$ $6H_2O$, HCl, $CaCl_2$, Na_2SO_4, and $(CH_2OH)_3CNH_2$, were added in the same propor-

tions, as those described in the reference, so to give the final ionic concentration of human plasma. The pH of the ionic buffer was adjusted to 7.4 by adding 0.1 M HCl or 0.1 M NaOH. The nanofiber mats were soaked in SBF and were incubated at room temperature with a rotary shaker at a speed of 40 rpm. The SBF was replaced with a fresh one, for every 2 days for a total period of 10 days. Further on, to investigate the formation of the bone-like apatite on the nanofiber surfaces, samples were vacuum dried and observed under FE-SEM.

2.5. Characterization

The morphology of the nanofiber mats was analyzed with a field emission scanning electron microscope (FE-SEM) Hitachi S-7400, Japan with an operating voltage at 200 kV combined with the energy dispersive X-ray (EDS). Transmission electron microscopy (TEM) was performed with JEOL JEM 2010 operating at 200 kV, (JEOL Ltd., Japan) and was combined with the energy dispersive X-ray. Both the FE-SEM and TEM instruments, were obtained directly from the company located at branch offices in South Korea. Additionally, scanning electron microscope (SEM) (Leo 435 VP) obtained from Carl Zeiss SMT Ltd., equipped with EDS operating at accelerating voltage of 3 kV was also used. The Information about the phases and crystallinity was obtained using Rigaku X-ray diffractometer (XRD, Rigaku Co., Japan) with Cu K_α (λ = 1.54056 Å) radiation over Bragg angles ranging from 10 to 80°. The spectroscopic characterization was investigated with Fourier-transform infrared (FT-IR); the spectra were recorded by grinding samples with KBr pellets using a Varian FTS 1000 FT-IR, Mid-IR spectral range, cooled DTGS detector, and Scimitar series (Varian Inc., Australia). The thermal stability and influence upon incubation of nanofiber mats before and after incubation in SBF was carried out with a Pyris TGA (Perkin Elmer Co., USA) by heating from 50 to 800°C under a continuous oxygen purge of 20 ml/min. The heating rate was 20°C/min.

3. Results and discussion

Electrospinning of colloidal solution that contains various amounts of HAp (0 to 7%) generated membranes that consist of well-defined nanofibers. As shown in Figure 2a and 2e, the FE-SEM images of nanofibers in low and high magnifications had been obtained after performing the electrospinning process. Figures 2a and 2e, obtained from electrospinning pure PU solution, demonstrates that smooth, uniform and bead-free nanofibers were produced. It is clear from the high magnification micrograph, that smooth and continuous fibers are formed by pristine PU. Moreover, its counterparts, containing various amounts of HAp (i.e., 3, 5 and 7%) are presented in Figure 2b, 2c and 2d, respectively. The morphology of the polymer nanofibers (in terms of general nanofibrous morphology) has not been affected by the addition of HAp in these electrospun mats. However, it can be observed that small decrease in diameter of nanofibers while analyzing Figures 2a, 2b, 2c and 2d. Furthermore, one can easily observe that the amount of HAp NPs increases as the concentration of HAp increases in the original colloidal solution used in electrospinning. In more details, the high magnification from the former figures are represented in Figures 2f, 2g and 2h. Actually, the observed NPs in (Figure 2f, 2g and 2h) are the large sized HAp particles; in other words, the particles with diameters larger than the average nanofiber diameter could not be embedded inside the nanofibers, and instead, they attach to the nanofiber threads or in simpler words they remain non-encapsulated. Moreover, the small sized NPs are encapsulated inside the nanofibers, analogously to the polymer/HAp in electrospun nanofiber mats that were previously reported [17–20].

XRD is a highly trustable technique utilized to investigate the nature of any crystalline compounds. The XRD pattern of pure HAp and nanofiber mats is presented in Figure 3. In this figure, the vertical base lines represent the standard HAp according to the JCPDS data base [31, 32]. As shown in this figure, all the corresponding peaks originating from the base line (i.e., standard HAp) and synthesized HAp NPs generally match with each other, which satisfy that the produced HAp is purely crystalline. Strong diffraction peaks at 2θ values for HAp can be seen at 31.77, 32.90, 34.08, 40.45, 46.71, 48.62, 49.46, 51.28, 52.10 and 53.14° that correspond to the crystal planes (211), (300), (202), (310), (222), (320), (213), (410), (402) and (004) [31, 32]. Therefore, it can be concluded that the calcination processes have eliminated the other impurities from the bovine bones [29], and the obtained molecular skeleton consists of pure HAp. Further on, the spec-

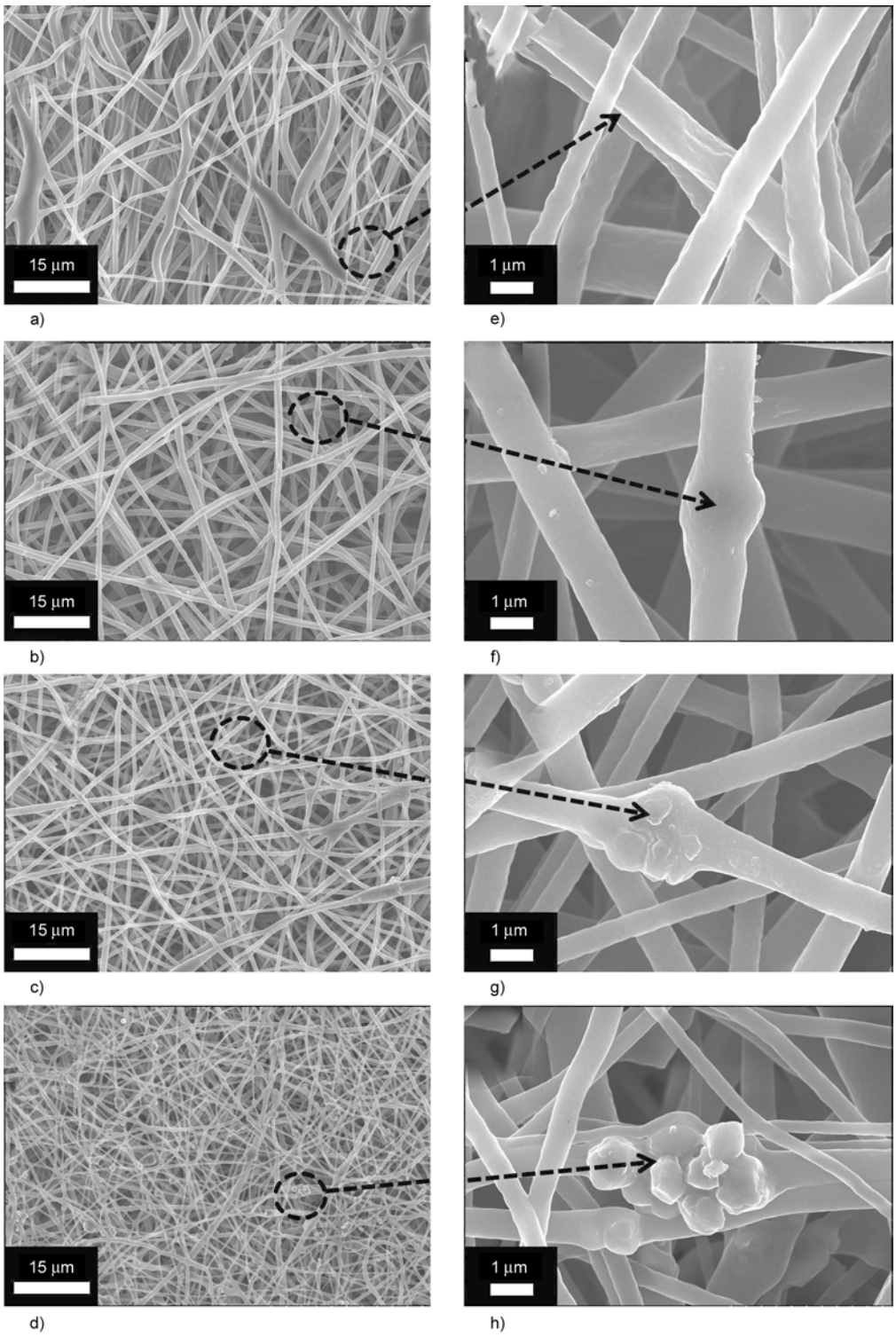

Figure 2. FE-SEM images for nanofibers that contain different amounts of HAp: 0% (a), 3% (b), 5% (c) and 7% (d) at low magnification. Corresponding figures containing 0% (e), 1% (f), 3% (g) and 7% (h) at high magnification from the encircled areas of low magnification images are also included.

tra of the pure PU, which is also represented in this figure, because the PU is amorphous in nature, it can be observed that the spectra do not possess any such reasonable peak to indicate its non-crystalline nature. However, compared with its other modified counterparts obtained from electrospinning the HAp-containing colloids, the spectra possess reasonable peaks, which are located at the same diffraction angles, that of standard HAp peaks and the used HAp in these nanofibers. These findings con-

firm that nanofibers involve HAp NPs within them and simultaneously support the FE-SEM results. It is interesting to note, that the intensities of the peaks obtained from XRD analysis increased as the concentration of original HAp used in the colloidal solutions was increased.

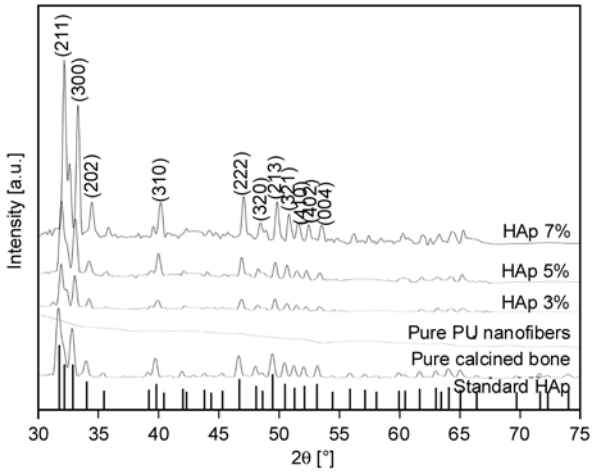

Figure 3. XRD results for the standard (the vertical base lines) and prepared hydroxyapatite (calcined). Also, the spectra of pristine PU and the prepared hydroxyapatite/PU nanofiber mat with different concentrations of hydroxyapatite.

To ensure that the added HAp particles are really present in/on nanofibers, FE-SEM equipped with EDS analysis was utilized for one of the modified nanofibers containing HAp NPs; the results are presented in Figure 4. As shown in Figure 4a and its corresponding EDS data, originating from the area analyses of the nanofibers. The evident presence of Ca and P peaks, from the (area analyses) indicates the presence of HAp, from this marked area (Figure 4a). For point EDS, from a specific area, the results are shown in Figure 4b, and its corresponding EDS is also presented. From this figure, we can clearly find the increase in concentration of the Ca to P ratios compared to the area EDS (Figure 4a). The Ca to P ratio from both areas (one with swelled and whole area) was in the range of 1:50±10, which is more or less equal to natural HAp. The presence of HAp at this (specific area) indicates that this part is rich in HAp and additionally this discussion, clarifies the dilemma that these

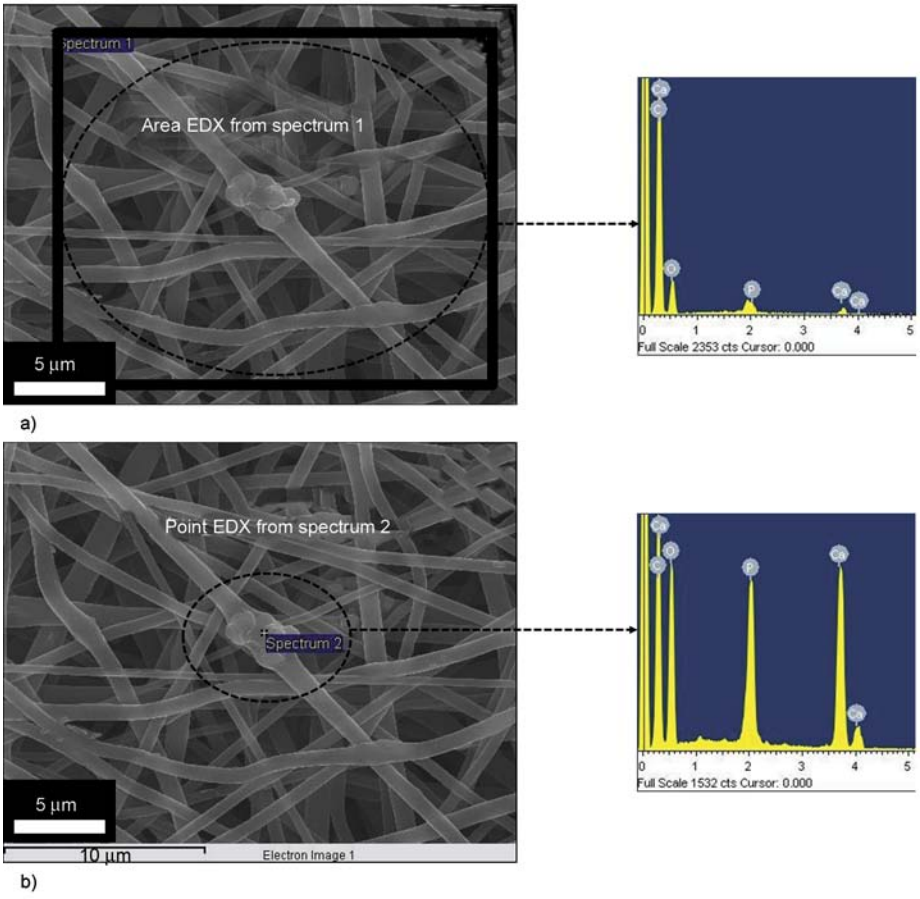

Figure 4. FE-SEM equipped with EDS images from one of the nanofibers containing HAp NPs. Area EDS of the nanofiber mat from the encircled area and its corresponding EDS scan results (a). Point EDS of the nanofiber mat from the point area that contains HAp NP and its corresponding EDS scan results (b).

swelled areas are beads, which is an electrospinning defect. It is worth mentioning, that presence of beads can be favorable in certain applications, for instance to increase the superhydrophobicity of nanofiber mats. In particular, this type of finding was observed when nanofibers of poly(3-hydroxybutyrate-co-3-hydroxyvalerate) (PHBV) was fabricated with various beads by electrospinning [33]. However, in our case we have obtained completely bead-free nanofibers which is favorable in general application of nanofibers, when nanofibers are to be used for implant purposes.

It is well known fact, that transmission electron microscope (TEM) analysis can be utilized to differentiate between crystalline and amorphous structures of materials. To investigate this phenomenon, the sampling was achieved by placing the TEM grid very close to the tip opening of the syringe needle for a few seconds during electrospinning process. In Figure 5 it can be observed that the nanofiber morphology is consistent with FE-SEM images in morphology. Figure 5a, also draws our attention to an interesting finding that the PU nanofibers can capture some large HAp NPs, which leads to more naked HAp NPs, which is beneficial in hard tissue applications. For further investigation, Figure 5b demonstrates the HR-TEM results for the black area; this image clearly shows apparent strips, which indicate high crystallinity for the marked area, considering the approved non-crystalline nature of the PU; this black area can be confidently attributed to HAp. The lattice image of an individual HAp from HR-TEM indicates that the HAp particle is an absolute crystal, with well-defined lattice fringes, and the lattice spacing of 0.47 nm, corresponds to the (110) HAp plane. The selected area electron diffraction (SAED) image in the (upper inset Figure 5b) reveals good crystallinity because there are no imperfections observed in the lattice planes. The atoms are arranged in a unique crystal lattice shape: the lattice shape of the standard HAp is hexagonal [31]. Moreover, the inverse Fast Fourier Transformation (FFT) of the (lower inset Figure 5b) image also confirms the good crystallinity in accordance with HR-TEM results.

It is noteworthy to mention, that used HAp NPs in this study were of different diameters, however, the exact size of used HAp NPs used in these experiments was not fully studied. Knowing this fact, it was expected that small sized NPs will reside inside the nanofibers and large one will remain partially captured on nanofibers surfaces. As indicated in case of FE-SEM results, (Figure 1 and Figure 5) which successfully proved the presence of bead-free nanofibers in obtained nanofibers after blending with HAp NPs. The occurrence of bead-like structure was due to large sized HAp NPs which remain partially encapsulated inside nanofibers. In those results, the location and presence of small sized NPs, over the nanofibers could not be discussed at that point. In order to find out the occurrence of small sized NPs inside the nanofibers and simultaneously to abolish this dilemma, that some of the used NPs are really small in size and therefore, are encapsulated inside the nanofibers. In this context, Figure 6 shows a TEM micrograph of the

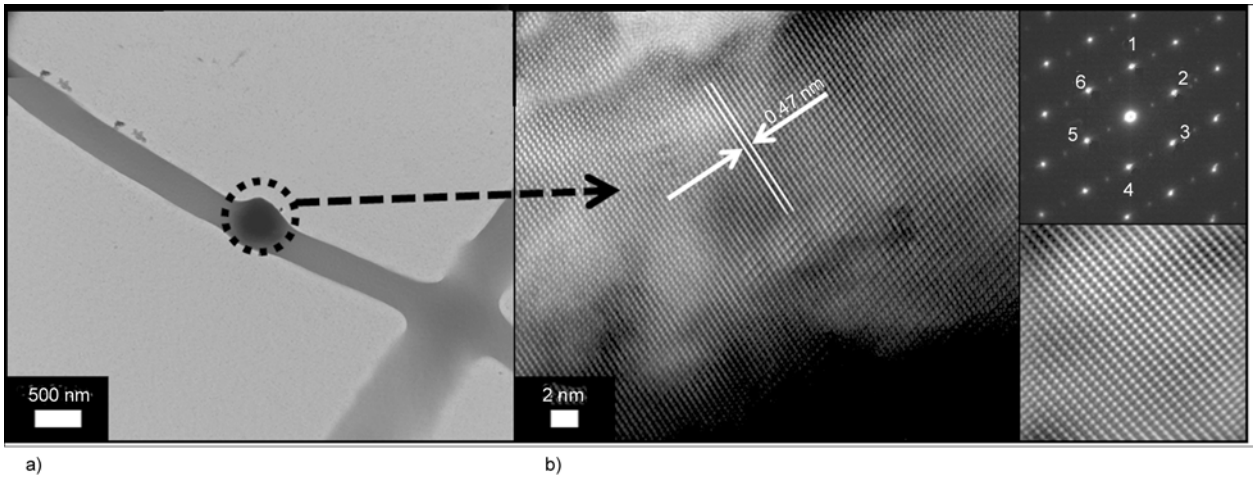

Figure 5. TEM of an individual nanofiber prepared from HAp/PU colloid (7 wt%): (a) high resolution transmission electron microscope (HR TEM) for the encircled area; (b) the (upper inset) selected area diffraction pattern (SAED) for the encircled area and the (lower inset) fast Fourier transformation (FFT) image

PU nanofibers containing 7 wt% HAp (showing small sized Hap NPs). In this figure it can be observed that PU which is non-crystalline in nature appeared as white in color, while the highly crystalline HAp NPs looks darker in color. Also, from this figure, it can be clearly observed that small sized NPs are encapsulated inside the nanofibers, which abolish the dilemma that used NPs are large in size, which simultaneously support the finding that small sized NPs can be accommodated inside the nanofibers. The inset in Figure 6 shows the SAED ring pattern of the nanofiber with encapsulated HAp NP. There are no stacking faults observed in the lattice planes, which confirms the good crystallinity of the present NPs inside nanofibers. The d spacing at 8.14, 4.72, 4.07, 3.44 and 1.94 Å can be indexed to the (211), (300), (202), (310) and (222) planes, which are close to the XRD results.

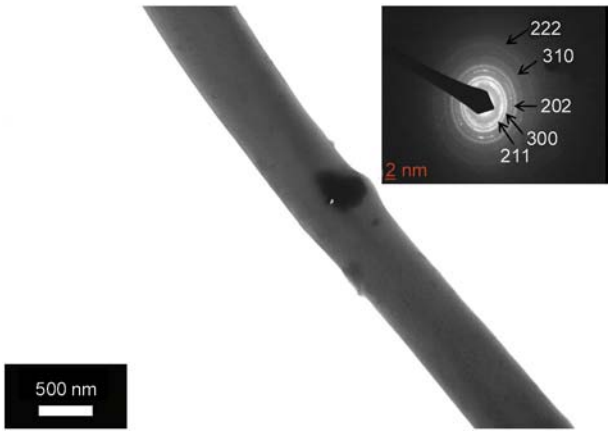

Figure 6. TEM of an individual nanofiber prepared from HAp/PU colloid (7 wt%), the inset figure shows selected area diffraction ring pattern from the edge of HAp NP

To check insightful understanding and chemical nature of NPs over nanofibers precisely, transmission electron microscopy (TEM) combined with the energy dispersive X-ray (EDS) analysis was done. For TEM-EDS analysis, the small nanofiber mats were ultrasonically dispersed in ethanol, and a drop of ethanol, which contained well dispersed nanofibers, was placed on the TEM grid and examined under microscope. In this regard, Figure 7 shows a low-magnification TEM-EDS image of the nano-

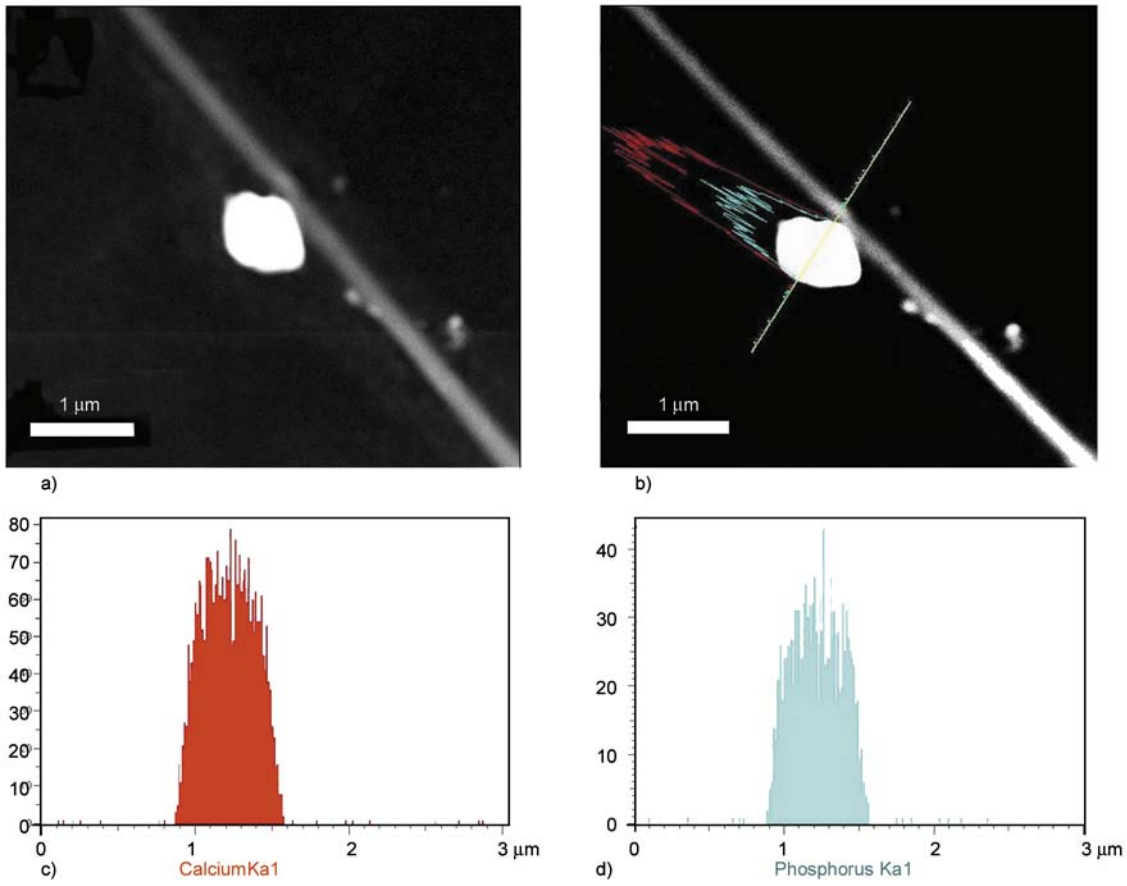

Figure 7. TEM-EDS image of nanofibers prepared from a HAp/PU colloid (7 wt%) (a); the linear EDS analysis along the line appearing in the figure (b); results of line mapping for two compounds analyzed as calcium in red (c) and phosphorous in cyan (d).

fiber from 7% PU/HAp nanofiber combination. From this image, it can be seen that the NPs are likely to be pulled away from main nanofiber stem because of the ultrasonication (Figures 7a and 7b). The EDS results from corresponding compound mapping results are shown in (Figures 7c and 7d). From these figures, one can clearly reveal the presence of Ca and P, which overall account the presence of HAp NPs. Therefore, these results strongly confirm the FE-SEM analyses that the naked NPs originate from HAp in the chemical composition present over the nanofibers.

Figure 8 shows the FT-IR spectra of nanofibers derived after electrospinning colloidal solutions. Absorbance, resulting from vibrational modes from phosphates and hydroxyl groups is present in the spectra. For instance, the PO_4^{3-} asymmetric stretching mode of vibration is characterized by a strong and complex band in the 1732–1037 cm^{-1} range and a medium intensity band at about 961 cm^{-1} that results from symmetric stretching vibrations [34]. The crystalline HAp generates characteristic OH bands at about 3446 cm^{-1}, and this phenomenon is noted in all the nanofiber combinations containing HAp. The small peaks at 1700–1450 cm^{-1}, indicate the existence of a Ca–O phase in the structure. A medium sharp peak at 628–635 cm^{-1}, is assigned to the O–H bending deformation mode. The intensity of these peaks increases as the amount of original HAp used to make colloidal solution for electrospinning increases.

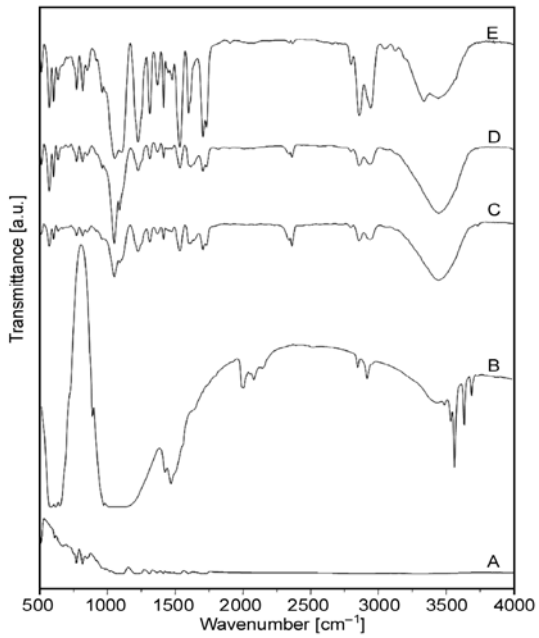

Figure 8. FT-IR spectra of pure PU nanofiber: (A) Calcined bones; (B) PU nanofiber containing 3% HAp; (C) PU nanofiber containing 5% HAp; and (D) PU nanofiber containing 7% HAp; (E)

Generally, it is believed that the formation of apatite nuclei requires a seed to facilitate the formation of bone-like apatite. It worth mentioning, that the utilized SBF was previously exploited to precipitate biological apatite on proposed hard tissue materials [35, 36]. To prove these findings, the nanofibers were incubated in the presence of SBF, which resembles with the human physiological conditions (i.e., T = 37°C and pH = 7.4) for 10 days. During the incubation period, the SBF solution was refreshed every 2 days by refilling the new solution. After 10 days of incubation, the nanofiber mats were washed with triply distilled water to remove the associated SBF and dried in the presence of P_2O_5 in a vacuum dryer to remove the residual moisture associated from the incubation media. Thus, after the drying process, nanofiber mats were subjected to FE-SEM analysis; the results are shown in Figure 9. It can be concluded from Figure 9a that the pristine PU nanofibers cannot be utilized as hard tissue because no apatite-like materials were precipitated within 10 days of incubation. However, it can be deduced from Figures 9b, 9c and 9d that the structure, as indicated by arrows, incorporates HAp NPs in/on nanofibers and strongly activates precipitation of the HAp on the nanofibers mats. Moreover, to get the further confirmation about the induction of biological entities on the nanofibers, after the incubation in SBF, the EDS on apatite-like materials from one of nanofiber combination is presented in Figure 10. In this figure, and its point EDS graph from the indicated marked place, from this figure the presence of Ca and P peaks in the spectra can be clearly visualized. These findings clearly indicate the presence of induction of apatite-like materials at the specific indicated areas. This finding overall suggests utilizing the prepared PU/HAp mats for medical fields because both of PU and HAp are biologically safe. It is worth mentioning, that the rate at which the implant degradation occurs has to coincide, as much as possible with the rate of new bone formation. Considering that PU is biodegradable, and in a nanofibrous shape, which mimics the extra cellular matrix present in body, it will be an ideal site of cell seeding and basis for apatite prolif-

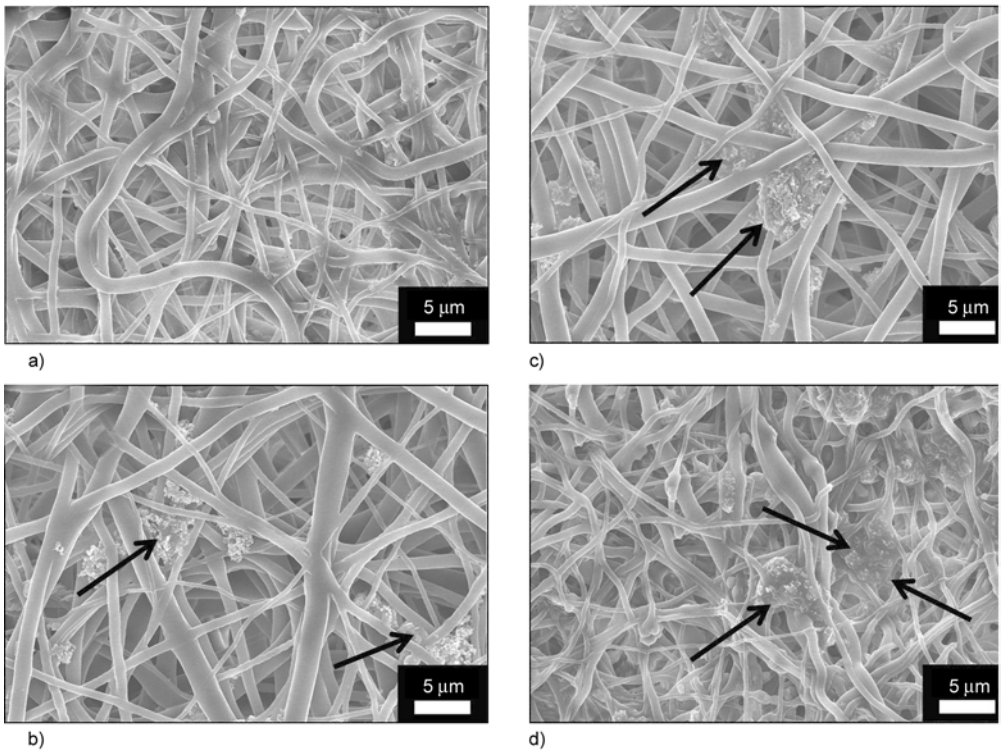

Figure 9. FE-SEM images for the PU nanofibers containing different amounts of hydroxyapatite: 0% (a), 3% (b), 5% (c) and 7% (d) with respect to polymer solution after incubation in SBF at 37°C for 10 days

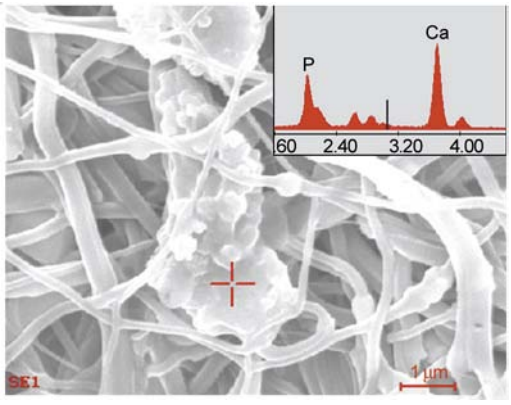

Figure 10. The EDS results from one of the modified nanofiber combination after incubation in SBF

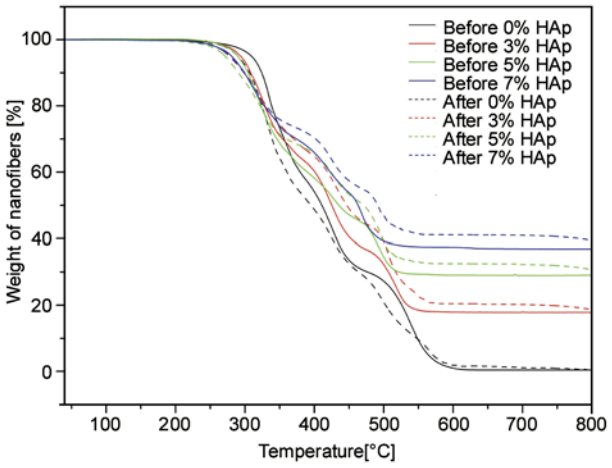

Figure 11. Thermal behavior and gain in residual weight of the PU nanofibers containing different amounts of hydroxyapatite before and after incubation in SBF at 37°C for 10 days

eration in the initial step after the implant replacement.

To get full confirmation that prepared nanofibers play a role in the formation of extra apatite upon incubation in SBF, and simultaneously support the FE-SEM and EDS results (i.e., Figure 9 and Figure 10). The TGA analyses of nanofibers for before and after incubation in SBF are represented in Figure 11. It was expected, that induction of biological apatite on nanofibers surfaces would result in increases of the residual weights during TGA analyses. Accordingly, from TGA analyses it was observed that the nanofibers before incubation in SBF show low residual weights remaining after exposure to a temperature of 550°C (marked by the complete lines). The nanofibers analyzed after incubation in SBF (marked by dashed lines) show higher residual weights remaining than the nanofibers used without incubation in SBF. It is interesting to note, that the residual weight of the nanofibers (i.e., 3, 5, and 7% HAp) that were incubated in SBF gained more residual weight compared with the pristine nano-

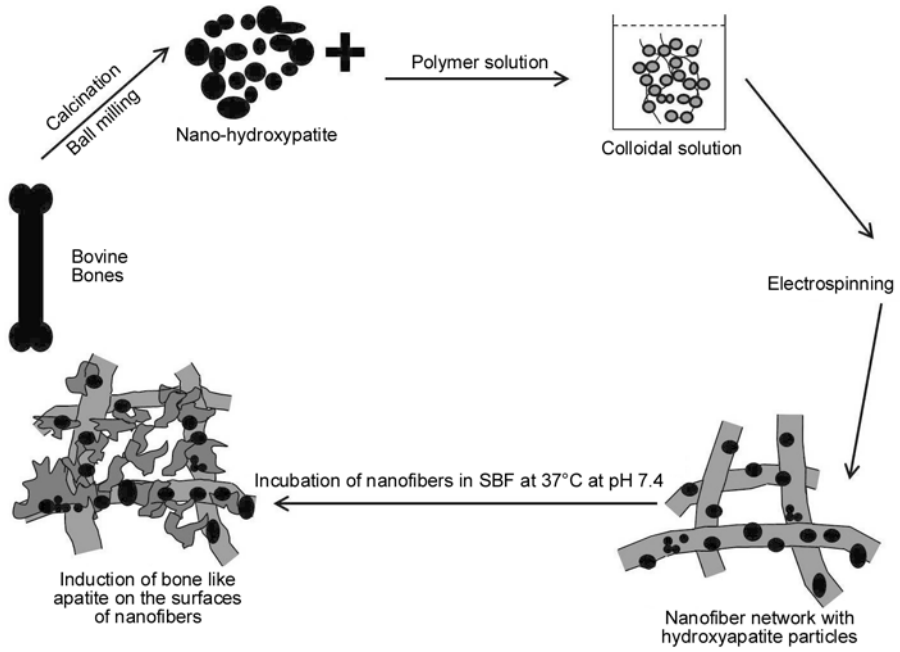

Figure 12. The systematic presentation for this novel strategy

fibers (i.e., 0% HAp). The presence of HAp in nanofibers might motivate the apatite formation process during incubation in SBF. Furthermore, these results confidently affirms, the hypothesis of apatite induction on surfaces of nanofibers upon the presence of apatite nuclei and confidently supports the results shown in FE-SEM (Figure 9 and Figure 10).

The whole procedure for making the ideal implants was described carefully. We introduce a generalized scheme to summarize the procedure and to justify that nanofibers bearing HAp NPs will act as favorable candidates for induction of apatite nuclei; therefore, they will be used as suitable candidates for future implant applications. Briefly, (Figure 12) indicates that the HAp NPs were obtained from calcination of bovine bones that were ground with a ball milling to obtain nanoparticulate size. Further step, involve the formation of the colloidal solution, which was electrospun to form nanofibers. These nanofibers containing HAp NPs were subjected to incubation in SBF. The presence of HAp around the nanofibers acted as seed, which promoted apatite particles to rest on the surfaces of nanofibers.

4. Conclusions

In conclusion, economically promising, environmentally desirable and biologically safe natural HAp NPs can be obtained from high temperature calcination of bovine bone. Electrospinning of a colloid solution comprised of the prepared HAp NPs and PU produces electrospun polymeric mats that include attached HAp NPs and partially captured NPs in the PU nanofibers. Nanofibrous shapes with a high structural space offer a bio-mimicking environment to accommodate and induce biological apatites on nanofiber surfaces. The HAp NPs alone strongly enhance the precipitation of biological apatites from the SBF solution during the incubation process because the NPs act as nuclei for the crystallization process. The SBF can be used to induce the formation of apatite on the nanofiber surfaces. The FE-SEM and TGA analyses can be utilized to differentiate the formation of excessive apatite on the surface of nanofibers upon incubation of SBF. In addition, the biological properties of both natural HAp and PU polymer and the results obtained in this study strongly suggest utilizing the proposed PU/HAp in hard tissue engineering applications.

Acknowledgements

This work was supported by a grant from the Korean Ministry of Education, Science and Technology (The Regional Core Research Program/Center for Healthcare Technology & Development, Chonbuk National University, Jeonju 561-756 Republic of Korea). Faheem A. Sheikh and Javier Macossay are thankful for the partial financial support for this work from NIH-NIGMS-NIA grant # 1SC2AG036825-01.

References

[1] LeGeros R. Z.: Calcium phosphates in oral biology and medicine. Karger, Basel (1991).

[2] Joschek S., Nies B., Krotz R., Göpferich A.: Chemical and physicochemical characterization of porous hydroxyapatite ceramics made of natural bone. Biomaterials, **21**, 1645–1658 (2000).
DOI: 10.1016/S0142-9612(00)00036-3

[3] Lü X. Y., Fan Y. B., Gu D., Cui W.: Preparation and characterization of natural hydroxyapatite from animal hard tissues. Key Engineering Materials, **342–343**, 213–342 (2007).
DOI: 10.4028/www.scientific.net/KEM.342-343.213

[4] Ozawa M., Suzuki S.: Microstructural development of natural hydroxyapatite originated from fish-bone waste through heat treatment. Journal of the American Ceramic Society, **85**, 1315–1317 (2002).
DOI: 10.1111/j.1151-2916.2002.tb00268.x

[5] Chen I-W., Wang X-H.: Sintering dense nanocrystalline ceramics without final-stage grain growth. Nature, **404**, 168–171 (2000).
DOI: 10.1038/35004548

[6] Hill C. M., An Y. H., Kang Q. K., Hartsock L. A., Gogolewski S., Gorna K.: Osteogenesis of osteoblast seeded polyurethane-hydroxyapatite scaffolds in nude mice. Macromolecular Symposia, **253**, 94–97 (2007).
DOI: 10.1002/masy.200750713

[7] Liao S., Chan C. K., Ramakrishna S.: Stem cells and biomimetic materials strategies for tissue engineering. Materials Science and Engineering: C, **28**, 1189–1202 (2008).
DOI: 10.1016/j.msec.2008.08.015

[8] Sheikh F. A., Barakat N. A. M., Kanjwal M. A., Chaudhari A. A., Jung I-H., Lee J. H., Kim H. Y.: Electrospun antimicrobial polyurethane nanofibers containing silver nanoparticles for biotechnological applications. Macromolecular Research, **17**, 688–696 (2009).
DOI: 10.1007/BF03218929

[9] Hong K. H.: Preparation and properties of electrospun poly(vinyl alcohol)/silver fiber web as wound dressings. Polymer Engineering and Science, **47**, 43–49 (2006).
DOI: 10.1002/pen.20660

[10] Sheikh F. A., Barakat N. A. M., Kanjwal M. A., Jeon S-H., Kang H-S., Kim H-Y.: Self synthesize of silver nanoparticles in/on polyurethane nanofibers: Nanobiotechnological approach. Journal of Applied Polymer Science, **115**, 3189–3198 (2010).
DOI: 10.1002/app.31418

[11] Kim G. H., Han H., Park J. H., Kim W. D.: An applicable electrospinning process for fabricating a mechanically improved nanofiber mat. Polymer Engineering and Science, **47**, 707–712 (2007).
DOI: 10.1002/pen.20744

[12] Kidoaki S., Kwon I. K., Matsuda T.: Structural features and mechanical properties of *in situ*–bonded meshes of segmented polyurethane electrospun from mixed solvents. Journal of Biomedical Materials Research Part B: Applied Biomaterials, **76**, 219–229 (2006).
DOI: 10.1002/jbm.b.30336

[13] Khlystalova T. K., Kurganova M. N., Demina A. I., Petova M. B., Tarakanov O. G.: Hydrolytic stability of polyurethanes in model biological media. Mechanics of Composite Materials, **21**, 763–767 (1986).
DOI: 10.1007/BF00605943

[14] Han J. H., Taylor J. D., Kim D. S., Kim Y. S., Kim Y. T., Cha G. S., Nam H.: Glucose biosensor with a hydrophilic polyurethane (HPU) blended with polyvinyl alcohol/vinyl butyral copolymer (PVAB) outer membrane. Sensors and Actuators B: Chemical, **123**, 384–390 (2007).
DOI: 10.1016/j.snb.2006.08.042

[15] Hainš N., Friščić V., Gordoš D.: Testing electrostatic properties of polyurethane coated textiles used for protective clothing. International Journal of Clothing Science and Technology, **159**, 250–257 (2003).
DOI: 10.1108/09556220310478350

[16] Khil M-S., Cha D-I., Kim H-Y., Kim I-S., Bhattarai N.: Electrospun nanofibrous polyurethane membrane as wound dressing. Journal of Biomedical Materials Research Part B: Applied Biomaterials, **67**, 675–679 (2003).
DOI: 10.1002/jbm.b.10058

[17] Nie H., Wang C-H.: Fabrication and characterization of PLGA/HAp composite scaffolds for delivery of BMP-2 plasmid DNA. Journal of Controlled Release, **120**, 111–121 (2007).
DOI: 10.1016/j.jconrel.2007.03.018

[18] Kim H-W., Knowles J. C., Kim H-E.: Hydroxyapatite/poly(ε-caprolactone) composite coatings on hydroxyapatite porous bone scaffold for drug delivery. Biomaterials, **25**, 1279–1287 (2004).
DOI: 10.1016/j.biomaterials.2003.07.003

[19] Venugopal J., Low S., Choon A. T., Sampath Kumar T. S., Ramakrishna S.: Mineralization of osteoblasts with electrospun collagen/hydroxyapatite nanofibers. Journal of Materials Science: Materials in Medicine, **19**, 2039–2046 (2008).
DOI: 10.1007/s10856-007-3289-x

[20] Zhang Y., Venugopal J. R., El-Turki A., Ramakrishna S., Su B., Lim C. T.: Electrospun biomimetic nanocomposite nanofibers of hydroxyapatite/chitosan for bone tissue engineering. Biomaterials, **29**, 4314–4322 (2008).
DOI: 10.1016/j.biomaterials.2008.07.038

[21] Zhou S., Zheng X., Yu X., Wang J., Weng J., Li X., Feng B., Yin M.: Hydrogen bonding interaction of poly(D,L-lactide)/hydroxyapatite nanocomposites. Chemistry of Materials, **19**, 247–253 (2007).
DOI: 10.1021/cm0619398

[22] Zheng X., Zhou S., Li X., Weng J.: Shape memory properties of poly(D,L-lactide)/hydroxyapatite composites. Biomaterials, **27**, 4288–4295 (2006). DOI: 10.1016/j.biomaterials.2006.03.043

[23] Kim H-W., Song J-H., Kim H-E.: Nanofiber generation of gelatin–hydroxyapatite biomimetics for guided tissue regeneration. Advanced Functional Materials, **15**, 1988–1994 (2005). DOI: 10.1002/adfm.200500116

[24] Fujihara K., Kotaki M., Ramakrishna S.: Guided bone regeneration membrane made of polycaprolactone/calcium carbonate composite nano-fibers. Biomaterials, **26**, 4139–4147 (2005). DOI: 10.1016/j.biomaterials.2004.09.014

[25] Erisken C., Kalyon D. M., Wang H.: Functionally graded electrospun polycaprolactone and β-tricalcium phosphate nanocomposites for tissue engineering applications. Biomaterials, **29**, 4065–4073 (2008). DOI: 10.1016/j.biomaterials.2008.06.022

[26] Sui G., Yang X., Mei F., Hu X., Chen G., Deng X., Ryu S.: Poly-L-lactic acid/hydroxyapatite hybrid membrane for bone tissue regeneration. Journal of Biomedical Materials Research Part A, **82**, 445–454 (2007). DOI: 10.1002/jbm.a.31166

[27] Barakat N. A. M., Khalil K. A., Sheikh F. A., Omran A. M., Gaihre B., Khil S. M., Kim H. Y.: Physiochemical characterizations of hydroxyapatite extracted from bovine bones by three different methods: Extraction of biologically desirable HAp. Materials Science and Engineering: C, **28**, 1381–1387 (2008). DOI: 10.1016/j.msec.2008.03.003

[28] Barakat N. A. M., Khil M. S., Omran A. M., Sheikh F. A., Kim H. Y.: Extraction of pure natural hydroxyapatite from the bovine bones bio waste by three different methods. Journal of Materials Processing Technology, **209**, 3408–3415 (2009). DOI: 10.1016/j.jmatprotec.2008.07.040

[29] Aerssens J., Boonen S., Lowet G., Dequeker J.: Interspecies differences in bone composition, density, and quality: Potential implications for *in vivo* bone research. Endocrinology, **139**, 663–670 (1982). DOI: 10.1210/en.139.2.663

[30] Kokubo T., Kushitani H., Sakka S., Kitsugi T., Yamamuro T.: Solutions able to reproduce *in vivo* surface-structure changes in bioactive glass-ceramic A-W^3. Journal of Biomedical Materials Research, **24**, 721–734 (1990). DOI: 10.1002/jbm.820240607

[31] Leng Y., Qu S.: TEM examination of single crystal hydroxyapatite diffraction. Journal of Materials Science Letters, **21**, 829–830 (2002). DOI: 10.1023/A:1015722607608

[32] Lopatin C. M., Pizziconi V., Alford T. L., Laursen T.: Hydroxyapatite powders and thin films prepared by a sol-gel technique. Thin Solid Films, **326**, 227–232 (1998). DOI: 10.1016/S0040-6090(98)00531-8

[33] Yoon Y. I., Moon H. S., Lyoo W. S., Lee T. S., Park W. H.: Superhydrophobicity of PHBV fibrous surface with bead-on-string structure. Journal of Colloid and Interface Science, **320**, 91–95 (2008). DOI: 10.1016/j.jcis.2008.01.029

[34] Blakeslee K. C., Condrate R. A.: Vibrational spectra of hydrothermally prepared hydroxyapatites. Journal of the American Ceramic Society, **54**, 559–563 (1971). DOI: 10.1111/j.1151-2916.1971.tb12207.x

[35] Oyane A., Uchid M., Choong C., Triffitt J., Jones J., Ito A.: Simple surface modification of poly(ε-caprolactone) for apatite deposition from simulated body fluid. Biomaterials, **26**, 2407–2413 (2005). DOI: 10.1016/j.biomaterials.2004.07.048

[36] Lin K., Chang J., Cheng R.: *In vitro* hydroxyapatite forming ability and dissolution of tobermorite nanofibers. Acta Biomaterialia, **3**, 271–276 (2007). DOI: 10.1016/j.actbio.2006.11.003

eXPRESS Polymer Letters Vol.6, No.1 (2012) 54–62
Available online at www.expresspolymlett.com
DOI: 10.3144/expresspolymlett.2012.6

Microscopic analysis of the morphology of seams in friction stir welded polypropylene

*Z. Kiss, T. Czigány**

Department of Polymer Engineering, Faculty of Mechanical Engineering, Budapest University of Technology and Economics. Műegyetem rkp 3., H-1111 Budapest, Hungary

Received 19 April 2011; accepted in revised form 3 August 2011

Abstract. Supermolecular structure of welded seams prepared by friction stir welding (FSW) of polypropylene sheets has been studied by optical and electron microscopy. It has been shown that in the central parts of the seam spherulitic structures similar to that of the base material are formed, while at the borderline of the seam, a complex supermolecular structure could be identified. Lower welding rotation speed resulted in a border transition zone of more complex feature than the higher rotation speed during FSW. This was accompanied by reduced joint efficiency.

Keywords: *processing technologies, morphology, polymer welding, polypropylene*

1. Introduction

Friction stir welding (FSW) is a welding method patented by Thomas *et al.* [1] in 1991, developed mainly for welding aluminum and other light metals. During FSW, a rotating tool is pushed in-between the plates to be welded and, as a result of the rotation, enough friction heat is formed for welding, then, by moving the tool along the edge of the plates a butt weld seam is formed. When welding metals the FSW tool consists basically of two parts [2]. One is the pin intruding between the plates the other is the shoulder smoothing the upper surface of the plates. There are several possible designs for the pin, usually containing grooves, which homogenize the plastic flowing material and transport it behind the tool. The pin generates the friction heat necessary for welding (Figure 1.) The role of the shoulder is to contain the plastic material swirling around the pin in the seam region and by smoothing the seam to provide an aesthetic surface [2]. Joined by FSW the crystalline structure has been studied in detail in the seam and in its neighborhood [3]. Analysis was done already for various metals [4]. Shearing processes arising under the effect of the rotating tool (pin + shoulder) associated plastic flow processes play a decisive role in the strength of the welded seam [5]. Similar to metals the welded seam and welding zone formed in polymers depends strongly on the developing morphology, i.e. on the supermolecular structure generated [6]. In the case of all welding processes the temperature necessary for welding is at or above the melting range of the base material. This triggers melting and crystallization and vari-

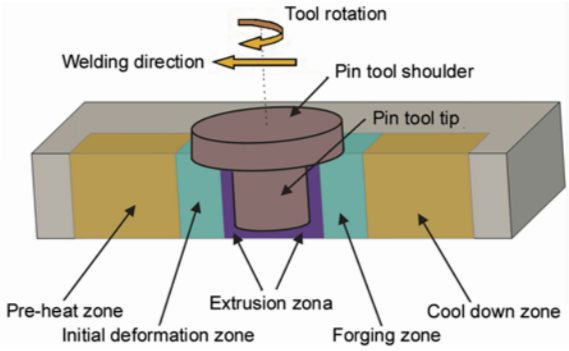

Figure 1. Scheme of the principle of friction stir welding for metals

*Corresponding author, e-mail: czigany@eik.bme.hu

ous deformation processes in the molten and heat affected layers, respectively, similar to other polymer processing technologies [7, 8]. Various friction welding methods were adapted for polymeric materials [6], and we have also dealt with the application possibilities of FSW in polymers [9].

Hot gas welding is an important and commonly used joining method. We have studied [10] the microstructure formed in the heat affected zone of welded polypropylene (PP) seams produced by this technique. The structure of the welded seam was divided into three main parts, starting from the base material toward the welded seam. The microspherulitic structure of the material essentially did not change during welding. A plastic zone was observed at the border of the seam and the base material, wherein a sheared zone arose due to the welding pressure, characterized by a cylindritic crystalline morphology. Practically the innermost part of the seam, defined as flow zone, consists of the additional material introduced. Mechanical and morphological properties of welded seams made by hot gas welding between plastic plates have also been studied by Balkan *et al.* [11]. In their work they pointed out that the weldability of materials is closely related to their rheological properties.

Varga *et al.* [12] welded together α and β-crystallized PP sheets made of various types of polypropylene (homo, random and block copolymers, different melt flow index values) by vibration method. Starting from the base material (bulk) a partially melted, sheared zone consisting of deformed spherulites was observed, wherein the degree of β nucleation also changed under the effect of shearing. At the center of the seam a fluid melt channel was observed which remained oriented during crystallization. The degree of orientation was so high at high welding pressures that it deteriorated the mechanical properties of the welded bond (the melt was squeezed out from the seam). In the case of smaller compressive forces, however, a fine spherulitic transition zone was observed between the base material and the fully molten, sheared layers, at the center of the seam, which improved the mechanical properties of the welded joint.

Schmachtenberg and Tüchert [13] investigated the seam of PP sheets welded by hot plate welding. The centerline of the welding was characterized by a transcrystalline structure. A structure similar to that of the base material could be observed in the coarse spherulitic zone, which was attributed to the effect of slow cooling rate. The coarse spherulitic structure was followed by a fine spherulitic layer caused by the high cooling rate. Streamlines formed in the sheared melt zone under the combined effect of fast cooling and shear. In contrast to the sheared melt zone spherulites melted only partially in the incompletely melted and sheared zone. The base material did not melt at all, within coarse spherulites could be observed.

Evolving microstructures arising during the FSW of metals and during the various welding processes of polymeric structural materials play a prominent role in determining the mechanical properties of the welded joints. The supermolecular structure formed in the seam and in its neighborhood during FSW has been scarcely studied. Very few publications are available on the application of the FSW method on polymers, however Nelson [14] filed a patent in this field. Aydin [15] has dealt with the FSW of polymers. The seams exhibited high strength values proving the applicability of FSW to polymeric structural materials, but the shoulder rotating together with the tool resulted in strongly degraded surface.

Strand and coworkers [16] used a stationary shoe equipped with an ancillary heating instead of the shoulder rotating together with the tool. Onion-ring like streamlines were observed on the cross section of the welded seams formed under the effect of melt flow. Comparing the microstructure of the welded seams with the results of three point bending tests it has been established that seams exhibiting spherulitic microstructure similar to that of the original base material (especially in the center of the seam) perform best. Spherulitic structure appeared if the tool diameter was large as compared to the plate thickness, at low feed rates. This can be explained by the fact that a higher peripheral speed resulting form the large diameter increased the frictional heat evolution too. Decreasing feed rate also results in more heat evolution. Arici and Sinmazçelýk [17] recognized the weaker mechanical properties, also published by Strand [16], were due to the weaker welding roots. Therefore they prepared two seams on both the lower and upper side of the plates. Using double seams welded joints with strength identical to the yield strength of the base material could be prepared. Rezugi *et al.* [18] have shown that the

surface of the welding tool and its rotation speed exerts a large influence on the welding temperature and on the strength of the joint. A version of FSW developed for point welding was studied by Bilici *et al.* [19] and by Arici and Mert [20]. Lap joints were prepared and the effects of welding parameters were studied. Both articles observed that in the preparation of point-welded seams the most important parameters were the penetration depth and the dwelling time used to preheat the part. During preheating the plates were touched by the rotating tool, resulting in heat evolution then, after a given time the rotation was stopped and the welding tool was pushed in-between the plates.

Having reviewed the literature it can be seen that the heat affected zone (HAZ) and morphology within play a decisive role in determining the strength of the joint. The effect of FSW parameters on the mechanical properties of the welded joint has been investigated by us [9] on friction stir welded PP joints. The aim of this paper is to study supermolecular structure of seams prepared by friction stir welding of PP sheets by optical and electron microscopy techniques.

2. Materials and methods

The scheme of the FSW technology is shown in Figure 2. In contrast to the welding of metals, instead of the shoulder rotating together with the tool, we used a non-heated smoothing shoe made of polytetrafluoroethylene.

In accordance with our preliminary experiments [9] a milling cutter of 8 mm in diameter with 8-tooth was used for welding of 10 mm thick extruded PP homopolymer plates (PP-DWST of Simona, Kirn, Germany, crystal melt temperature: 160–165°C, density: 0.905 g/cm^3, modulus: 1400 MPa, Melt Flow Index: 0.4 g/10 min, tensile strength: 25.6 MPa).

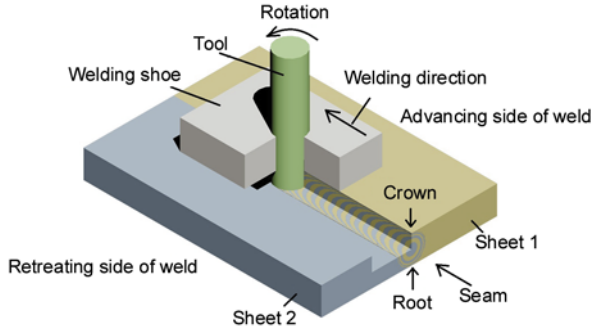

Figure 2. Scheme of the principle of friction stir welding for polymers

The welding cutting depth was 9.6 mm, the feeding rate was 60 mm/min. Two rotation speed values were selected for the morphological study: A lower strength (welded at a rotation speed of 2000 rotations per minute (rpm)) and the maximum tensile strength welded joints (welded at 3000 rpm) were compared. The efficiency factors of the joints are the tensile strengths of the welded joints as compared to the tensile strength of the base material. The efficiency factors of PP plates at the two investigated rotations were 54.9±5.7% at 2000 rpm and 86±2.6% at 3000 rpm (relative to the tensile strength of the base material, 25 MPa).

The crystalline structure was investigated using crossed polarizer (linear polarizer, analyzer and first order λ-plate between the polarizers (located diagonally)) in transmission mode in an Olympus BX 51 (Tokyo, Japan) optical microscope. For this about 10 µm thick slices were cut from the seam using a Bright 5040 microtome (Huntingdon, Cambridgeshire, United Kingdom) and 3–5 µm slices using a Leica EM UC6 ultramicrotome (Vienna, Austria) with an FC7 cryochamber (Vienna, Austria). Several smaller slices were prepared to study the welded seam: some cut from the center of the seam, others from the base material and from the borderline between the two zones.

A JEOL JSM-6380LA (Tokyo, Japan) type electron microscope was also used for the study of the crystalline structure. In order to visualize the supermolecular structure chemical etching was used [21]. The etchant was 0.7 m/m% potassium permanganate dissolved in a 2:1 mixture of sulfuric acid and phosphoric acid. The acidic medium etches first the amorphous part of the surface of the specimens immersed into the etchant, thus the residual crystalline parts (here the spherulites) protrude from the surface and become observable. Only suggested values are available for the etching time, so the etching time was selected to be 4 hours based on preliminary experiments. After etching the samples were first rinsed with diluted sulfuric acid (7:1 water: sulfuric acid) then with hydrogen peroxide and finally with distilled water. Before etching the cross sections of the seams were polished.

In our optical and electron microscopic studies the PP seams were observed in the cross section as shown in Figure 3. The welded seam meets the base material along the line defined by the outer perime-

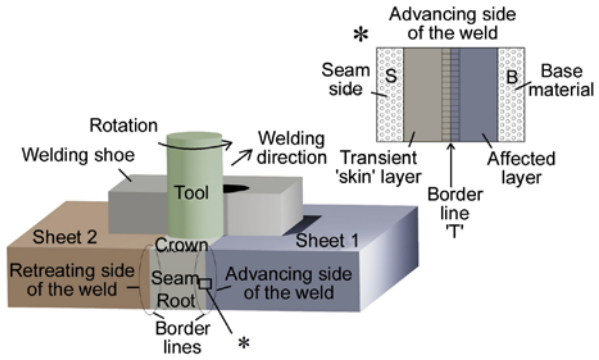

Figure 3. Build-up of the seam produced by FSW. Note: The blue region is the inset represents the heat affected zone (HAZ).

ter of the tool (borderlines). The borderlines on the both sides of the seam can be distinguished based on the relation between the peripheral speed of the tool and the welding direction. Where the direction of the peripheral speed of the tool is identical with the welding direction it is called the advancing side of the weld, while if the two directions are opposite, it is called the retreating side of the weld. In our studies no significant differences were found between the advancing and retreating sides of the weld. It is explained by the fact that assuming 2000 and 3000 rpm rotation speeds and 8 mm diameter tool the peripheral speed is 837 and 1256 mm/s respectively. Comparing these values with the feed rate of 1 mm/s, the difference coming from the rotation direction is negligible between the two sides of the seam. In our optical and electron microscopic studies special care has been taken to investigate the crystalline structure at the immediate neighborhood of the borderlines. To support the understanding of the results the position of the sample cut-offs is indicated in the, magnified inset in Figure 3.

3. Results and discussion

Optical microscopy

Spherulitic structure can be observed in the sections shown in Figure 4. No difference was found between the lower and upper parts of the cross sections (i.e. between the lower and upper sides of the plate). The spherulites were distributed homogeneously over the cross sections and in the central zone of the seam (Figure 4a). The crystalline structure is very similar to the spherulitic structure of the base material (see Figure 4b). At higher magnification (200×) a λ-plate was also used in the optical microscope. The spherulites of the base material (25–30 μm) are larger than those found in the seam (10–20 μm). The reduced spherulite diameter may likely be due to 'memory effect'. The heat development in FSW was not sufficient to erase the 'prehistory' of the extruded sheet. The residual self nuclei initiated the crystallization yielding spherulites with reduced mean diameter compared to the base sheet [22]. Nonetheless, similar spherulite sizes in the centre of the seam and in the base material suggest that the related cooling conditions were also comparable.

As no major differences were found in the supermolecular structure in the central regions of the seam in follow-up studies we concentrated on samples taken from the transition zone (on the borderline between the base material and the seam (Fig-

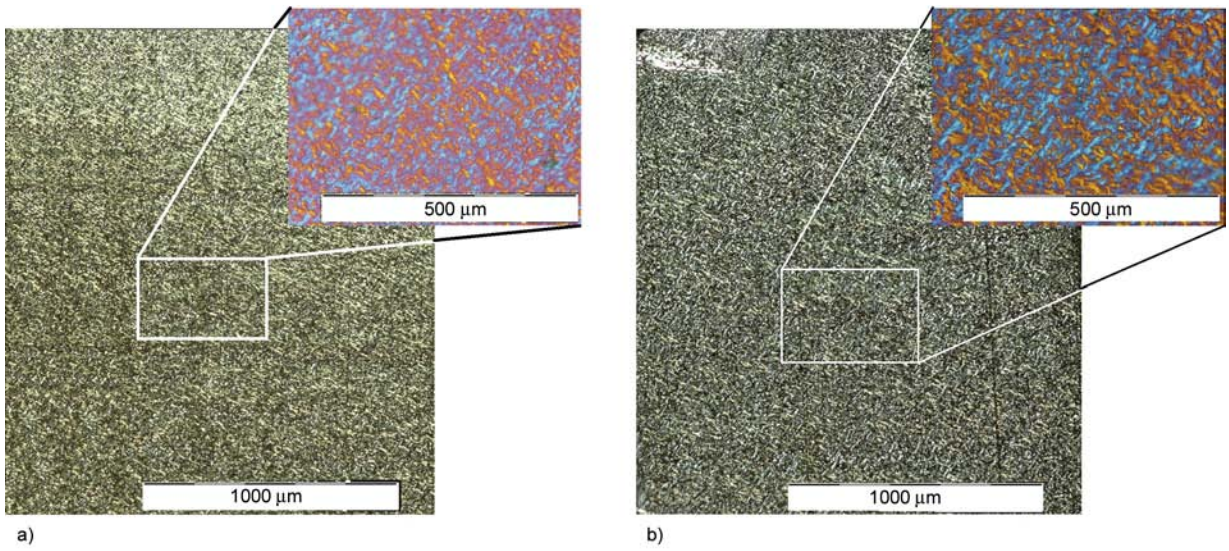

Figure 4. Optical micrograph with crossed polarizer a) From the center of the seam, b) From the base material. Note: inset images were made by additional use of λ-plate.

ure 3)). 5–10 μm thick slices were cut by microtome from the advancing and retreating sides of the seam for the study.

Figure 5a shows the borderline appearing at the advancing side of the welded seam prepared at a rotation speed of 2000 rpm. At the left and right sides of the borderline the sperulitic structures of the seam and of the base material are similar, but between the two a transition zone of 400–500 μm width can be observed. Figure 5b and 5c show a highlighted part of the transition zone, indicating the recognized supermolecular structural layers. From right to left these are as follows:

B: Original spherulitic structure of the base (bulk) material (average spherulite size is 25–30 μm).

T_{outer}: Sheared zone of distorted spherulitic structure produced by the peripheral speed of the welding tool. Although this layer is located near to the advancing tool, the temperature developed during welding softened the PP and 'smeared' along the mantle of the tool. A flow zone of the base material being located near to the movement of the tool. Here the polymer completely melted under the effect of the locally high temperature, flows and crystallizes in form of cylindrites along the shear rate direction. The cylindritic crystallization is due to the fact that shear aligned PP chains cannot relax owing to the fast cooling of this zone. The cylindritic structure is induced by row-nuclei (a special version of self-nucleation) [22].

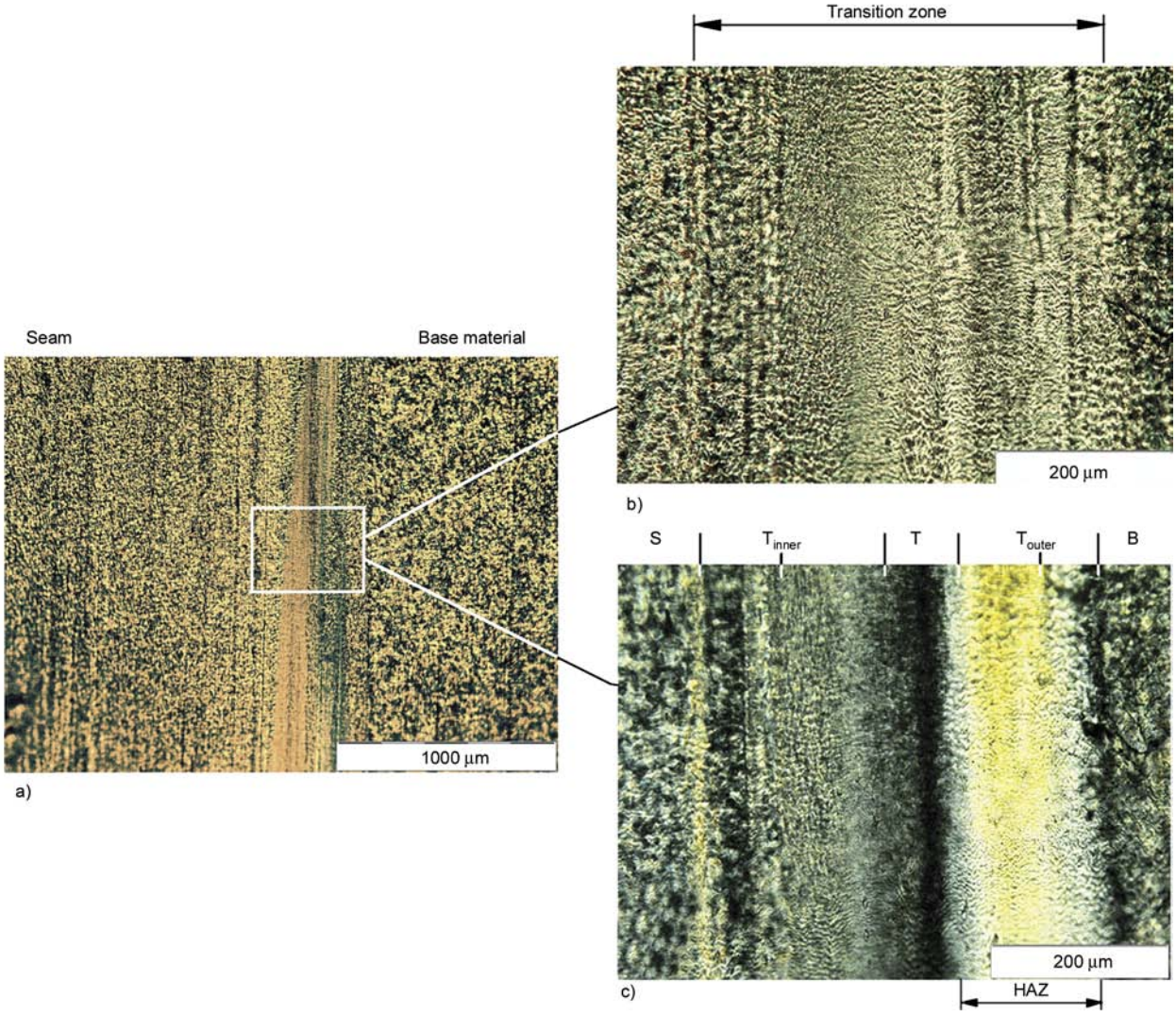

Figure 5. Optical micrographs of the border region between the seam (produced at 2000 rpm) and the base material in transmission mode using crossed polarizers. a) Spherulitic structure of the seam and of the base (bulk) material, b), c) Supermolecular structure developed in the border region. Notes: pictures b) and c) display the transitions zone (also referred to skin-core structure) of the FSW seam along with the designations introduced. Frames b) and c) were taken using a polarizer the plane of which was diagonal and parallel to the oriented structure of the seam, respectively.

T: This line represents the movement of the tool mantle. It is practically the initial borderline between the seam and the base material.

T_{inner}: A flow zone of the seam developed similar to that of T_{outer}, but on the seam side. Accordingly, this has the same cylindritic structure. Toward to the base (bulk) material a highly distorted spherulitic layer can be resolved. Its formation is controlled by two effects: heat subtraction toward to the bulk, and crystallization affected by self-nucleation.

S: Inside the seam (*S*) again spherulites are formed.

To sum up, this is some kind of skin-core structure, often found in injection molded PP items [7]. Slow cooling in the central part of the welding seam ('core') results in spherulitic crystallization. By contrast, in the 'skin' the formation of the supermolecular structure is due to interplay between cooling, molecular alignment/relaxation and crystallization markedly influenced by the latter. This kind skin-core structure (similar to that observed in injection molded specimens) provides the slow cooling necessary for the spherulitic crystallization. After welding while in the 'skin' regular spherulites cannot develop because of the more intense heat withdrawal (the heat diffusing towards the base material), in the central part of the seam (in the 'core') the crystallization goes on undisturbed.

In the case of the welded joint prepared at 3000 rpm the width of the transition zone between the base material and the seam was about 200–300 μm, much narrower than in case of at 2000 rpm. The faster rotation speed of the tool results in higher temperature associated with reduced melt viscosity. Consequently, the shearing conditions are different. Because of the higher temperature the time for molecular relaxation is longer. The width of the seam is controlled by the interplay of the above two parameters.

Figure 6 shows a cryomicrotomed specimen from the welded joint prepared at 3000 rpm. Using the cryomicrotome only very narrow slice could be made (about 300 μm width), but even here the decreasing size of the spherulites of the base material towards the seam can be observed. The cylindritic structure developed along a straight line described by the side line of the mantle of the tool (outer perimeter of the tool). The same straight borderline can be observed in the SEM micrographs too.

Electron microscopic studies on etched samples

In order to study the crystalline structure of the seam and of the base material etched samples were also prepared and studied afterwards by SEM. The advantage of the method compared to optical microscopy is that the seam needs not be divided into several parts to cut slices form it, as the etched sample can be placed as a whole into the sample holder of the SEM. Further advantages are the higher magnification and the depth of field.

Figure 7 shows the micrographs of the seam (Figure 7a) and of the base material (Figure 7b) with improved contrast for better visibility. One can see that the spherulites of the seam are somewhat smaller (10–20 μm diameter) than those of the base material (25–30 μm), this difference could be observed on the optical micrographs too. The spherulites in the seam are not only smaller, but,

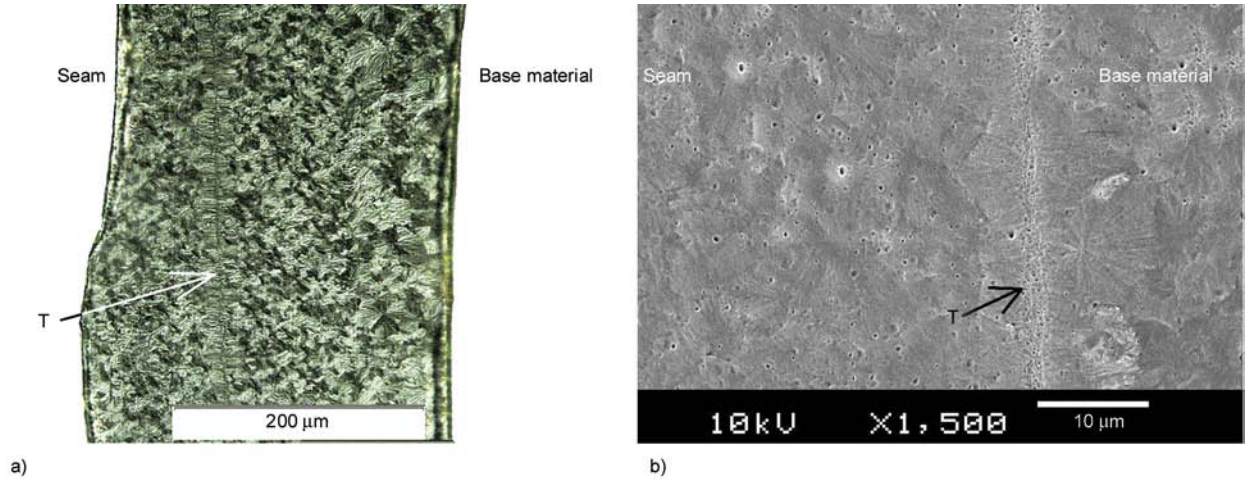

Figure 6. The border region between the seam and the base material at 3000 rpm. a) On a specimen prepared by cryomicrotome, b) SEM micrograph of an etched specimen.

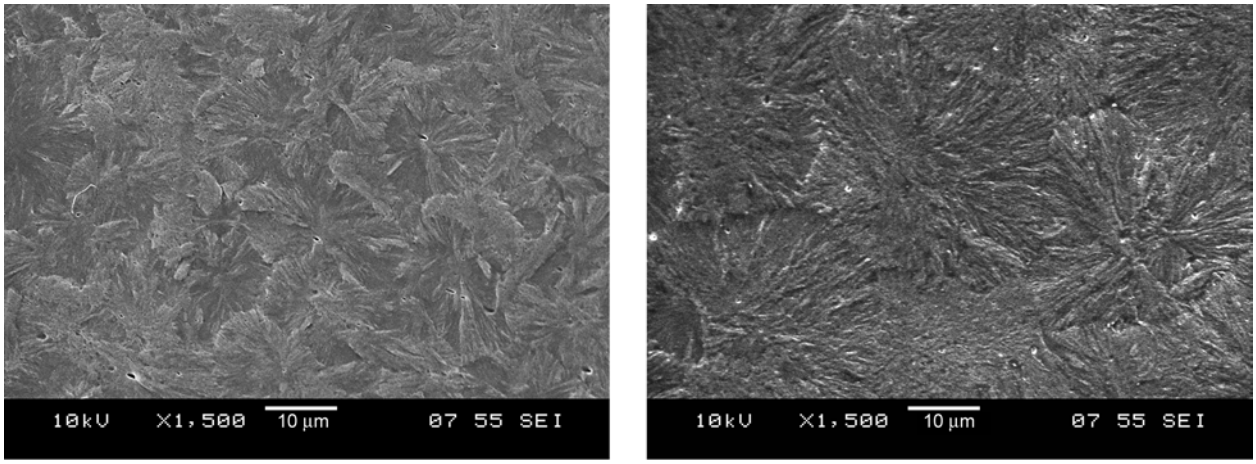

Figure 7. SEM micrographs after 4 hours etching: a) From the seam, b) From the base material

with respect to their regularity, they are much more fragmented. This can be attributed to the mixing-shearing effect of the welding tool.

When studying etched samples we have concentrated on the borderline between the seam and of the base material, investigating the transition zones observed by optical microscopy. Figure 8 shows that at 3000 rpm the spherulitic structure of the base material changes suddenly. When moving towards the center of the seam the spherulitic structure can again be observed after about a 40 µm distance but the size is smaller and the regularity is lower than in the case of the base material.

Similarly to our optical microscopic studies also in the SEM micrographs streamlines can be observed at 2000 rpm at the borderline of the seam and of the base material (Figure 3). At these parts the melt was exposed to strong shearing during welding, so the polymer crystallized in a layered form, along certain lines, corresponding to the streamlines. The

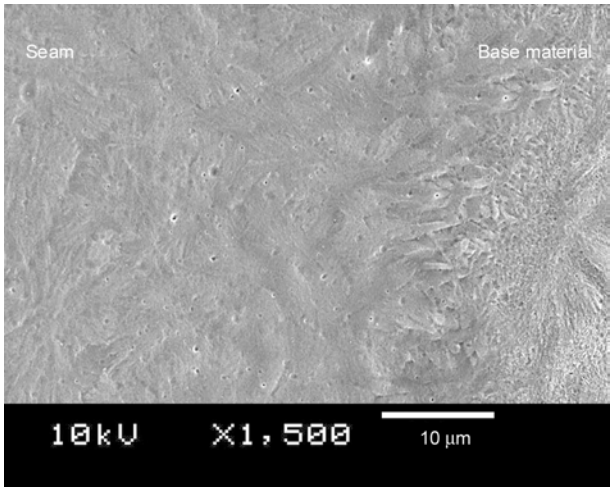

Figure 8. Borderline of the base material and of the seam at 3000 rpm

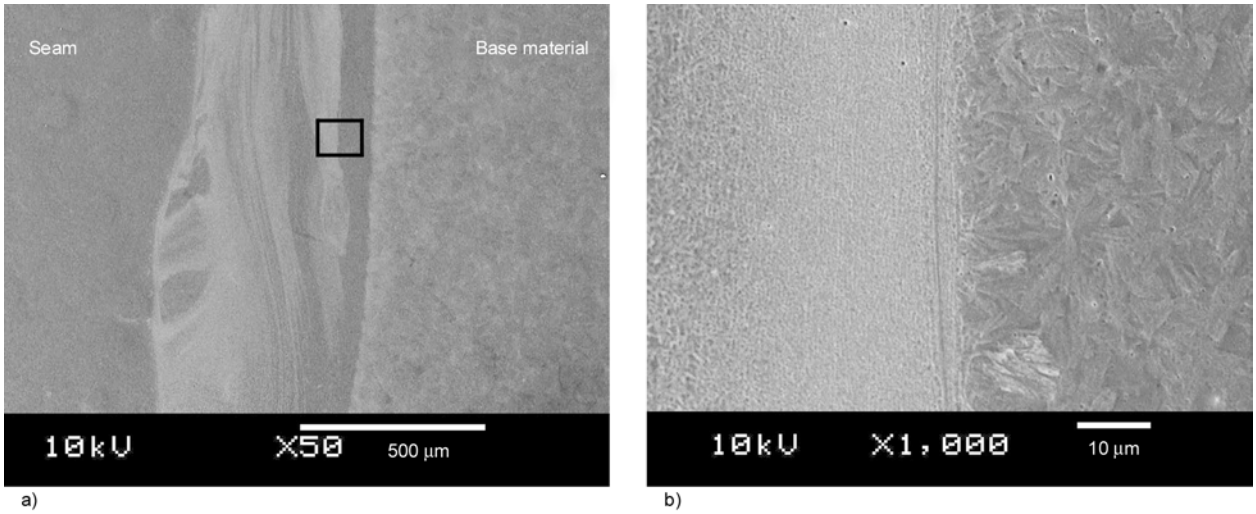

Figure 9. The borderline between the base material and the seam at 2000 rpm. a) Regularity caused by the flow, b) There are no spherulites in the region exposed to flow.

phenomenon shown in Figure 9a can also be observed by naked eye both at the retreating and at the advancing flow borderlines. Figure 9b shows the small spherulites characteristic of the seam at the borderline of the strongly sheared region with greater magnification, together with the crystallized layer formed along the streamlines produced by the tool. The layer sheared under the effect of flow developed because of the lower degree of melting due to the lower rotation speed, as here, because of the lower temperature the melt strength of polypropylene was higher. Consequently the homogeneity of the seam was lower, reflected by the lower weld strength.

4. Conclusions

Supermolecular structure of polyproplyene seams prepared by friction stir welding has been studied by optical and electron microscopy. One lower (welding at a rotation speed of 2000 rpm) and the maximum tensile strength welded joints (welded at 3000 rpm) were compared.

It has been observed both in optical microscopic and in electron microscopic studies that at the center of the seam spherulitic structure similar to that of the base material. However, the average diameter of the spherulites (10–20 μm) is only about half of than the base material (25–30 μm). The spherulitic structure, observed in the central part of the seam, is due to the relatively slow cooling rate in the central part of the seam. In the samples welded with low rotation speed a transition zone of 400–500 μm width was observed (Figure 5b) at the border of the base material and the seam. The width of this transition zone reduced to about half (200–300 μm) in FSW with high rotation speed. Several supermolecular structures were identified in the transition zone, and at the outer perimeter of the tool (in the side line of the mantle) a straight borderline was observed. The related structure was cylindritic or distorted aligned spherulitic when PP crystallized from the melt. Distorted spherulites were formed under shear stresses in the heat affected zone (HAZ – Figure 5b) where the PP became 'softer'. It was found that the smaller the overall width of the seam and the less complex its morphology are, the better the joint efficiency of the FSW weld is.

Acknowledgements

This work is connected to the scientific program of the 'Development of quality-oriented and harmonized R+D+I strategy and functional model at BME' project. This project is supported by the New Széchenyi Plan (Project ID: TÁMOP-4.2.1/B-09/1/KMR-2010-0002).

References

[1] Thomas W. M., Nicholas E. D., Needham J. C., Murch M. G., Temple-Smith P., Dawes C. J.: Friction stir butt welding. G.B. Patent 9125978.8, Great Britain (1991).

[2] Mishra R. S., Ma Z. Y.: Friction stir welding and processing. Materials Science and Engineering, 50, 1–78 (2005).
DOI: 10.1016/j.mser.2005.07.001

[3] Fonda R. W., Bingert J. F., Colligan K. J.: Development of grain structure during friction stir welding. Scripta Materiala, **51**, 243–248 (2004).
DOI: 10.1016/j.scriptamat.2004.04.017

[4] Fujii H., Sun Y., Kato, H., Nakata K.: Investigation of welding parameter dependent microstructure and mechanical properties in friction stir welded pure Ti joints. Materials Science and Engineering A, **527**, 3386–3391 (2010).
DOI: 10.1016/j.msea.2010.02.023

[5] Hamilton C., Dymek S., Blicharski M.: A model of material flow during friction stir welding. Materials Characterization, **59**, 1206–1214 (2008).
DOI: 10.1016/j.matchar.2007.10.002

[6] Patham B., Foss P. H.: Thermoplastic vibration welding: Review of process phenomenology and processing–structure–property interrelationships. Polymer Engineering and Science, **51**, 1–22 (2011).
DOI: 10.1002/pen.21784

[7] Karger-Kocsis J., Friedrich K.: Effect of skin-core morphology on fatigue crack propagation in injection moulded polypropylene homopolymer. International Journal of Fatigue, **11**, 161–168 (1989).
DOI: 10.1016/0142-1123(89)90435-0

[8] Wang L., Yang W., Huang L., Yang B., Sun N., Yang M-B.: Effect of thermal gradient field with phase change on crystal morphologies of HDPE During GAIM process. Plastics, Rubber and Composites, **39**, 385–391 (2010).
DOI: 10.1179/174328910X12777566997450

[9] Kiss Z., Czigány T.: Applicability of friction stir welding in polymeric materials. Periodica Polytechnica, Ser.Mech.Eng., **51**, 15–18 (2007).
DOI: 10.3311/pp.me.2007-1.02

[10] Marczis B., Czigány T.: Interrelationships between welding parameters of hot-gas welded polypropylene. Polymer Engineering and Science, **46**, 1173–1181 (2006).
DOI: 10.1002/pen.20570

[11] Balkan O., Demirer H., Ezdeşir A., Yıldırım H.: Effects of welding procedures on mechanical and morphological properties of hot gas butt welded PE, PP, and PVC sheets. Polymer Engineering and Science, **48**, 732–746 (2008). DOI: 10.1002/pen.21014

[12] Varga J., Ehrenstein G. W., Schlarb A. K.: Vibration welding of alpha and beta isotactic polypropylenes: Mechanical properties and structure. Express Polymer Letters, **2**, 148–156 (2008). DOI: 10.3144/expresspolymlett.2008.20

[13] Schmachtenberg E., Tüchert C.: Long-term properties of butt-welded poly(propylene). Macromolecular Materials and Engineering, **288**, 291–300 (2003). DOI: 10.1002/mame.200390024

[14] Nelson T. M.: Friction stir welding of polymeric materials. U.S. Patent 6811632, USA (2004).

[15] Aydin M.: Effects of welding parameters and pre-heating on the friction stir welding of UHMW-polyethylene. Polymer-Plastics Technology and Engineering, **49**, 595–601 (2010). DOI: 10.1080/03602551003664503

[16] Strand S. R.: Effects of friction stir welding on polymer microstructure. MSc Thesis, Department of Mechanical Engineering, Brigham Young University (2004).

[17] Arici A., Sinmazçelýk T.: Effects of double passes of the tool on friction stir welding of polyethylene. Journal of Materials Science, **40**, 3313–3316 (2005). DOI: 10.1007/s10853-005-2709-x

[18] Rezgui M. A., Ayadi M., Cheouat A., Hamrouni K., Zghal A., Bejaoui S.: Application of Taguchi approach to optimize friction stir welding parameters of polyethylene. EPJ Web of Conferences, **6**, 07003/1–07003/8 (2010). DOI: 10.1051/epjconf/20100607003

[19] Bilici M. K., Yükler A. İ., Kurtulmuş M.: The optimization of welding parameters for friction stir spot welding of high density polyethylene sheets. Materials and Design, **32**, 4074–4079 (2011). DOI: 10.1016/j.matdes.2011.03.014

[20] Arici A., Mert S.: Friction stir spot welding of polypropylene. Journal of Reinforced Plastics and Composites, **27**, 2001–2004 (2008). DOI: 10.1177/0731684408089134

[21] Olley R. H., Bassett D. C.: An improved permanganic etchant for polyolefines. Polymer, **23**, 1707–1710 (1982). DOI: 10.1016/0032-3861(82)90110-0

[22] Varga J.: Supermolecular structure of isotactic polypropylene. Journal of Materials Science, **27**, 2557–2579 (1992). DOI: 10.1007/BF00540671

eXPRESS Polymer Letters Vol.6, No.1 (2012) 63–69
Available online at www.expresspolymlett.com
DOI: 10.3144/expresspolymlett.2012.7

Shape memory polyurethane foams

*S. M. Kang, S. J. Lee, B. K. Kim**

Department of Polymer Science and Engineering, Pusan National University, Busan 609-735, Korea

Received 22 April 2011; accepted in revised form 4 August 2011

Abstract. Molded flexible polyurethane (PU) foams have been synthesized from polypropylene glycol (PPG) with different molecular weights (M_w) and functionalities (f), and 2,4/2,6-toluene diisocyanate (TDI-80) with water as blowing agent. It was found that the glassy state properties of the foam mainly depended on the urethane group content while the rubbery state properties on the crosslink density. That is, PPG of low MW and low f (more urethane groups) provided superior glass state modulus, strength, density, shape fixity and glass transition temperature (T_g), while that of high M_w and high f (higher crosslink density) showed high rubbery modulus and shape recovery. Consequently shape fixity of low M_w PPG decreased from 85 to 72% while shape recovery increased from 52 to 63% as the content of high M_w PPG increased from 0 to 40%.

Keywords: *smart polymers, polyurethane foam, dynamic mechanical properties, shape memory properties, density*

1. Introduction

Shape memory polymers (SMPs) respond to stimuli such as temperature, electricity, pH, ionic strength and light [1–4], and have many advantages like low density, good shape recovery and easy processing [5–9]. Thermally actuated SMPs have found broad applications in actuators, smart textiles and coatings, sporting goods [10, 11] and in biomedical devices [12]. Recently, triple shape effect and two way shape memory behavior which are largely based on thermal triggering have also been suggested. [13–15]. Excellent reviews have also been published along with recent developments [6, 16, 17].

Molded flexible polyurethane foams are used in a broad range of applications including transportation seating and trim parts, packaging, furniture, and novelty items. The greatest advantage is that the foam is molded into the desired intricate shape and the need for cutting is eliminated [18, 19]. If high shape fixity and high shape recovery are endowed to such foam products, precision molding with high durability will be implemented.

Shape memory effects of polyurethane foam have also been reported with regard to the thermomechanical properties [20, 21], laser-activated foam device [22], effect of shape holding conditions [23], and for biomedical application [24, 25] Most of these studies use commercially available polyurethane foams. Consequently, the basic structure-property relationships of the shape memory foam have not been reported perhaps except those by the present groups [26, 27].

In this work molded flexible polyurethane foams have been synthesized from polypropylene glycol (PPG) with various molecular weights (M_w) and functionalities (f), and 2,4/2,6-toluene diisocyanate with water as blowing agent. The reactivity, mechanical and dynamic mechanical and shape memory properties of the foams were analyzed along with basic structure- property relationship of the foam.

2. Experimental

2.1. Raw materials

Two types of polypropylene glycol (PPG), viz. SR-240 and GP-3000 (KPX, Korea) with different

*Corresponding author, e-mail: bkkim@pnu.edu

molecular weights (M_w) and functionalities (f) were used. SR-240 has the number average molecular weight (determined by gel permeation chromatography) of 240, and functionality of 2, while $f = 3$ and number average $M_w = 3000$ for GP-3000. The Toluene diisocynate (TDI-80) was provided by Dow Chemical whereas TA-350 as a cell-opener by KPX Chemicals. The water used as chemical blowing agent was distilled in our laboratory. L-626 (silicon surfactant), A1 (bis(2-dimethylaminoethyl) ether, amine catalyst) and methylene chloride (MC, blowing catalysts) and T-9 (stannous octoate, organometallic gelling catalyst) were provided by Air Products (USA) and used as received.

2.2. Preparation of polyurethane foam

The flexible foams were synthesized by one-shot method. All raw materials were first put into a 500 ml beaker and mixed for 20 s at 3000 rpm using a dispersing turbine type impeller of 2.5 cm diameter at 25°C and 70% relative humidity. Then the mixtures were discharged to an open mold (200 × 200 × 200 mm) and the foam cake was cured for 48 h at room temperature. The NCO index (isocyanate equivalents/polyol equivalents) was fixed at 1.00. We designed and synthesized six types of molded flexible polyurethane foams having various ratios of the two polyols giving different average M_w and f values. The basic formulations are given in Table 1.

2.3. Characterizations

Kinetics of the foam formation was followed by the physical change of the properties. The cream time corresponds to the start of bubble rise and hence color of the mixture becomes creamlike from milk due to the formation of foam bubbles. Rise time is the starting point of stable network formation by intensive formations of urethane and urea linkages and crosslinkings by allophanate and biuret reactions. The two characteristic times were measured by a digital stop watch.

The density of the foam was measured according to ASTM D 1622 with sample size of 30 × 30 × 30 mm (width × length × thickness), and an average of at least five measurements was taken to report. The cell structure of the foam was studied with a polarized optical microscope (POM) at a magnification of 120. For the measurement, central part of the foam was cryogenically fractured in liquid nitrogen. The total number of cells was countered to report the number average size of the cell. Dynamic mechanical properties of the foam were measured using a dynamic mechanical thermal analyzer (DMTA, Rheometrics MK-IV) in tension mode. Samples were heated from –100 to 150°C at 5°C/min, 10 Hz and 2% strain.

Tensile properties of the foam were measured at room temperature with an universal testing machine (UTM, Lloyd, UK) at 2.00mm/min with the specimen dimension of 4 × 25 × 0.3 mm (width × length × thickness). To measure the compressive strength, samples were cut into dimensions of 50 × 50 × 50 mm (width × length × thickness) and placed between metal plates and compressed to 50% of the original thickness.

Shape memory properties were characterized using a temperature controlled universal testing machine. The sample was first heated to a loading temperature (T_g + 20°C) at 4°C/min before it was loaded to a maximum strain (ε_m) of 100%, followed by cooling to (T_g – 20°C) at a rate of 7°C/min under constant strain. Then the sample was unloaded, giving a substantial amount of shrinkage (ε_u) depending on the molecular and shape parameters of the foam. Then the sample was reheated to the loading temperature (T_g + 20°C) to recover the strain, leaving a substantial amount of permanent strain (ε_p). These

Table 1. Formulations to synthesize the polyurethane foams, T_g, and $G°_n$ (unit: pphp)

	SR-240	GP-3000	TA-350	L-626	Water	A1	T9	M.C	TDI-80	T_g [°C]	$G°_n \cdot 10^6$ [dyne/cm^2]
S10	100	–	2	1	1.6	0.2	0.1	3	52.81	49.8	2.3
S08	80	20							47.06	39.6	3.6
S06	60	40							41.30	26.5	4.1
S04	40	60							35.64	–12.3	4.1
S02	20	80							29.92	–15.1	4.7
S00	–	100							24.21	–49.2	5.1

pphp: part per hundred polyol

three steps complete one thermomechanical cycle [28]. Shape fixity and shape recovery are defined by Equations (1) and (2) respectively:

$$\% \text{ shape fixity} = \frac{\varepsilon_u}{\varepsilon_m} \cdot 100 \quad (1)$$

$$\% \text{ shape recovery} = \frac{\varepsilon_r}{\varepsilon_m} \cdot 100 \quad (2)$$

where $\varepsilon_r = \varepsilon_u - \varepsilon_p$ is the recovered strain.

3. Results and discussion

3.1. Reactivity and foam density

Reactivity of the foaming reaction caused measuring the cream time and rise time. Table 2 shows that the two characteristic times monotonically increase with the increases of average molecular weight and functionality of the polyol mixture. This implies that both gelling and blowing reactions become slower. The reactivity decrease is primarily due to the decreased concentration of OH group which reacts with the isocyanate. This is seen from the decreased amount of the diisocyanate used in Table 1.

Typical POM morphologies of the foam are shown in Figure 1 and the details are summarized in Table 1 where the cell size increases from 0.3 (S10) to 0.45 mm (S04) with increasing molecular weight and functionality of the polyol. In accordance with the increased cell size, foam density decreases from about 59 (S10) to 52 (S04) [kg/m^3] (Figure 2). The smaller cell size with low M_w polyol is due to the fast gelling reaction over the foaming reaction.

Table 2. Reactivity and cell size

	S10	S08	S06	S04
Cream time [s]	9	11	14	18
Rise time [s]	189	200	219	235
Cell size [mm]	0.30	0.36	0.37	0.45

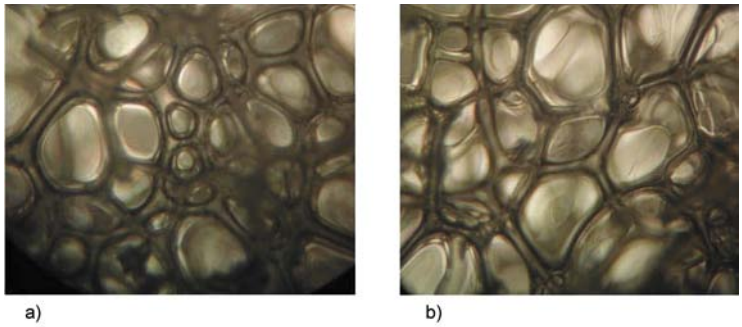

Figure 1. Typical POM morphologies of the foams (×120)

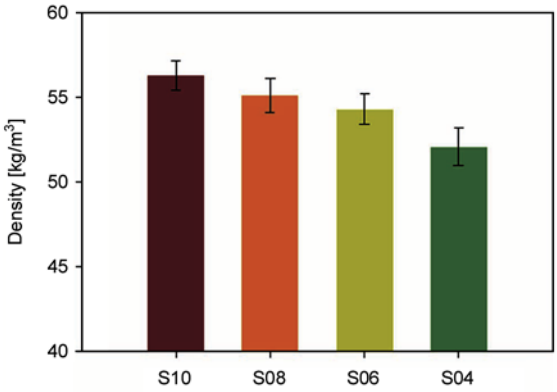

Figure 2. Density of the polyurethane foams

Then the cell becomes strong enough before it is blown keeping the cell small. Density is a most important parameter to control the mechanical properties of the foam. The decreased foam density is related to the decreased urethane group content and glass transition temperature of the foam to be discussed with the dynamic mechanical measurements to follow.

3.2. Mechanical properties

It is seen that the tensile stress-strain curves are almost linear regardless of polyol type (Figure 3).

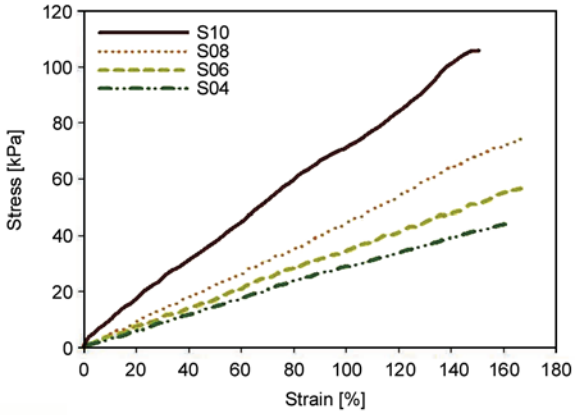

Figure 3. Tensile behaviors of the polyurethane foams

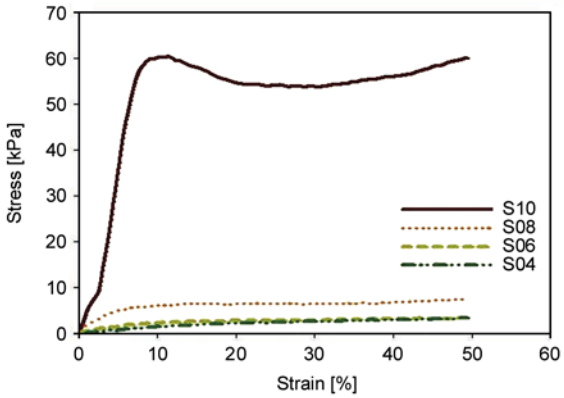

Figure 4. Compressive behaviors of the polyurethane foams

The initial modulus and break strength monotonically decrease with increasing molecular weight and functionality of the polyol while keeping the elongation at break almost constant. For example, the modulus of S10 is over 72 while that of S04 is about 25 kPa. The decrease is mainly due to the decreased T_g which on the other hand is introduced by the high molecular weight polyol which provides high chain flexibility and less urethane group. The two factors contribute to the lower T_g of the foam. It is mentioned that S02 and S00 showed insufficient loading capability to measure at room temperature.

Figure 4 shows the compressive strength of the foam. The strength at 50% deformation of the original thickness was taken as the compressive strength of the foam. As expected the compressive modulus and strength decreases with increasing molecular weight and functionality of the polyol. Only S10 shows compression yield, necking-like behavior and strain hardening. It is noted that the compressive strength of S10 is greater than the tensile strength while those of others are lower than the tensile strength when compared at the same deformation (50%). This is an indication that the S10 is in glassy state and others are in rubbery state.

3.3. Dynamic mechanical properties

The dynamic mechanical properties of the foams are given Figure 5 and Table 1 as a function of temperature. It is seen that the T_g of the foam which is seen in terms of tanδ peak decreases and the peak width broadens as the molecular weight and functionality of the polyol increases. The peak temperature ranges from about –50°C (S00) to 50°C (S10). Since the broad peak is an indication of broad damping and heterogeneity of the sample, lower molecular weight polyol augments the homogeneity of PU by the increased more hydrogen bonding between the urethane groups.

It is of interest to note that the glassy state modulus decreases while the rubbery state modulus increases with increasing molecular weight and functionality of the polyol. The decreased glassy modulus is a direct response of the decreased density of the foam. Density should decrease with decreasing intermolecular force which in this case is the hydrogen bonding between the urethane groups. On the other hand, increasing rubbery modulus is due to the increased crosslink density of the foam. Crosslink is introduced mainly by the tri-functional polyol. It is also introduced by the biuret reactions between the free isocyanate and urea groups, as noted from the existence of the rubbery plateau for S10 having no trifunctional polyol. Urea groups are introduced by the foaming reaction between the free isocyanate and water.

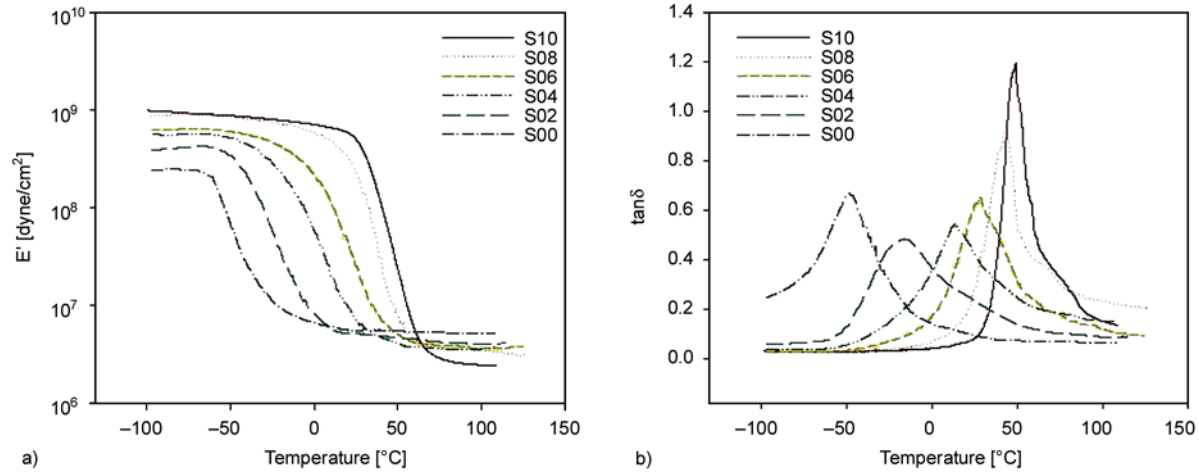

Figure 5. Dynamic mechanical properties of the polyurethane foams: storage modulus (a) and loss tangent (b)

It is noted that rubbery plateau modulus increases as the functionality of the polyol increases in accordance with the ideal rubber theory as shon by Equation (3) [29]:

$$G^{o}_{n} = \frac{\rho RT}{M_c} \tag{3}$$

where ρ is the density, R the gas constant, T the absolute temperature and M_c the molecular weight between the crosslinks. This implies that crosslink introduced by the tri-functional polyol of high molecular weight governs the rubbery state modulus while in glassy state the secondary force mainly governs the physical and mechanical properties of the foam.

3.4. Shape memory properties

Figure 6 shows the cyclic loading and unloading behavior of the foam for the first four thermomechanical cycles. It is seen that the shape fixity decreases from about 84 (S10) to 72% (S06) while shape recovery increases from 52 (S10) to 63 % (S06) with increasing molecular weight and functionality of the polyol [27]. This indicates that shape fixity depends on the glassy state modulus and shape recovery on the rubbery state modulus. This seems reasonable since shape is fixed during cooling where the slope of cooling step is the glass modulus [12] while the strain is recovered in rubbery state via the rubber elasticity which increases with increasing crosslink density. It is worth mentioning that the elastic strain energy viz. the area under the stress-strain curve is smaller with higher molecular weight polyol, thus the retractive force is maximum with S10. Regardless of polyol type, the cyclic hysteresis, viz. the reduction of area upon further cycling is mostly confined to the first cycle implying most chain breakages and chain slips are confined to the first cycle. However, it should be mentioned that the cyclic hysteresis of the foam is more serious than that of the elastomeric material [5, 28] due to the physical breakage of the cell structure, implying that foam is inherently more vulnerable to chain breakage upon tensile loading as compared with elastomeric materials.

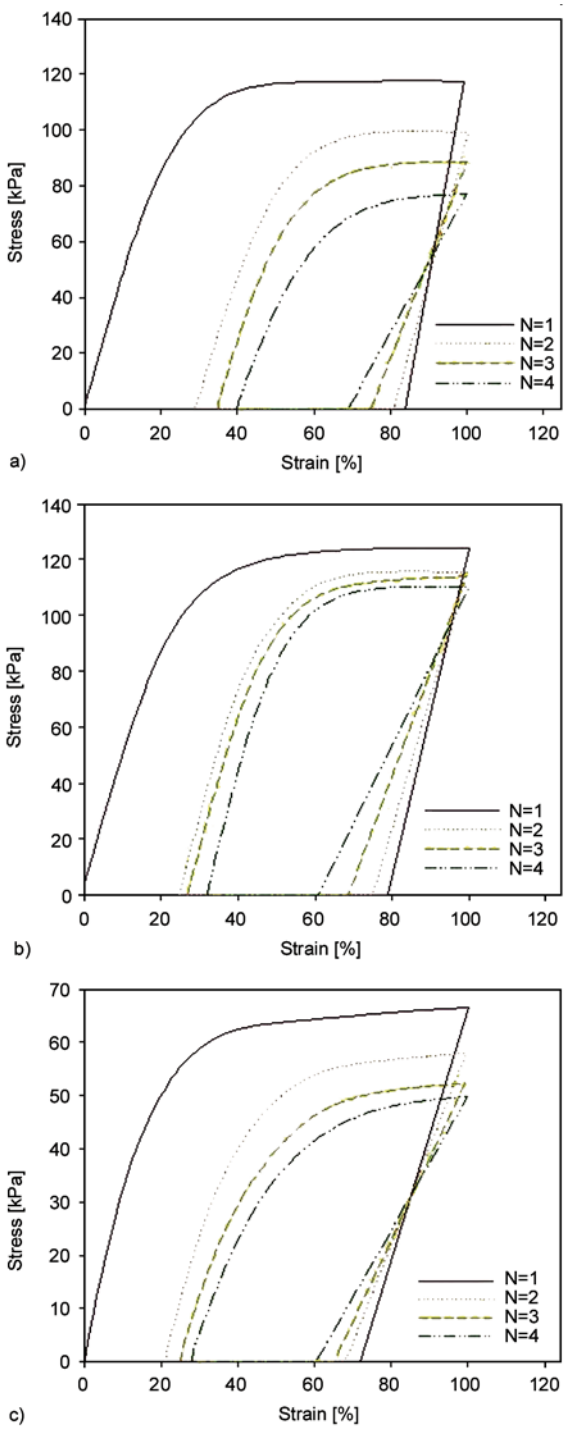

Figure 6. Thermomechanical cyclic behaviors of the polyurethane foams: (a) S10, (b) S08, (c) S06. *N* is the number of cycle.

4. Conclusions

The effects of molecular weight and functionality of polyol on the properties of molded flexible polyurethane foam were studied and the following conclusions were drawn.

The cream time and rise time monotonically increased with the increases of average molecular weight of the polyol mixture due to the decreased concentration of OH group.

The glassy state properties of the foam mainly depended on the urethane group content, i.e., lower molecular weight polyol gave smaller cell size, higher foam density, strength and glass modulus. On the other hand, the rubbery state properties mainly depended on the crosslink density of the polyurethane, i.e., high crosslink density of high molecular weight of polyol gave high rubbery modulus according to the rubber elasticity. Consequently, high shape fixity of low molecular weight polyol is due to the high glassy state modulus while the high shape recovery of high molecular weight polyol due to the great rubber elasticity.

Acknowledgements

The research has been supported by the NCRC and PNU-IFAM JRC both organized at PNU.

References

[1] Schmidt A. M.: Electromagnetic activation of shape memory polymer networks containing magnetic nanoparticles. Macromolecular Rapid Communications, **27**, 1168–1172 (2006).
DOI: 10.1002/marc.200600225

[2] Lendlein A., Jiang H., Jünger O., Langer R.: Light-induced shape-memory polymer. Nature, **434**, 879–882 (2005).
DOI: 10.1038/nature03496

[3] Scott T. F., Schneider A. D., Cook W. D., Bowman C. N.: Photoinduced plasticity in cross-linked polymers. Science, **308**, 1615–1617 (2005).
DOI: 10.1126/science.1110505

[4] Kolesov I. S., Radusch H-J.: Multiple shape-memory behavior and thermal-mechanical properties of peroxide cross-linked blends of linear and short-chain branched polyethylenes. Express Polymer Letters, **2**, 461–473 (2008).
DOI: 10.3144/expresspolymlett.2008.56

[5] Lee B. S., Chun B. C., Chung Y-C., Sul K. I., Cho J. W.: Structure and thermomechanical properties of polyurethane block copolymers with shape memory effect. Macromolecules, **34**, 6431–6437 (2001).
DOI: 10.1021/ma0018421

[6] Lendlein A., Kelch S.: Shape-memory polymers. Angewandte Chemie International Edition, **41**, 2034–2057 (2002).
DOI: 10.1002/1521-3773(20020617)41:12<2034::AID-ANIE2034>3.0.CO;2-M

[7] Fan K., Huang W. M., Wang C. C., Ding Z., Zhao Y., Purnawali H., Liew K. C., Zheng L. X.: Water-responsive shape memory hybrid: Design concept and demonstration. Express Polymer Letters, **5**, 409–416 (2011).
DOI: 10.3144/expresspolymlett.2011.40

[8] Huang W. M., Ding Z., Wang C. C., Wei J., Zhao Y., Purnawali H.: Shape memory materials. Materials Today, **13**, 54–61 (2010).
DOI: 10.1016/S1369-7021(10)70128-0

[9] Sun L., Huang W. M.: Mechanisms of the multi-shape memory effect and temperature memory effect in shape memorypolymers. Soft Matter, **6**, 4403–4406 (2010).
DOI: 10.1039/C0SM00236D

[10] Zhu Y., Hu J., Yeung L-Y., Liu Y., Ji F., Yeung K-W.: Development of shape memory polyurethane fiber with complete shape recoverability. Smart Materials and Structures, **15**, 1385–1394 (2006).
DOI: 10.1088/0964-1726/15/5/027

[11] D'hollander S., Van Assche G., Van Mele B., Du Prez F.: Novel synthetic strategy toward shape memory polyurethanes with a well-defined switching temperature. Polymer, **50**, 4447–4454 (2009).
DOI: 10.1016/j.polymer.2009.07.021

[12] Smela E.: Conjugated polymer actuators for biomedical applications. Advanced Materials, **15**, 481–494 (2003).
DOI: 10.1002/adma.200390113

[13] Kim B. K.: New frontiers of shape memory polymers. Express Polymer Letters, **4**, 589 (2010).
DOI: 10.3144/expresspolymlett.2010.73

[14] Chung T., Romo-Uribe A., Mather P. T.: Two-way reversible shape memory in a semicrystalline network. Macromolecules, **41**, 184–192 (2008).
DOI: 10.1021/ma071517z

[15] Hong S. J., Yu W-R., Youk J. H.: Two-way shape memory behavior of shape memory polyurethanes with a bias load. Smart Materials and Structures, **19**, 035022/1–035022/9 (2010).
DOI: 10.1088/0964-1726/19/3/035022

[16] Ratna D., Karger-Kocsis J.: Recent advances in shape memory polymers and composites: A review. Journal of Materials Science, **43**, 254–269 (2008).
DOI: 10.1007/s10853-007-2176-7

[17] Liu C., Qin H., Mather P. T.: Review of progress in shape-memory polymers. Journal of Materials Chemistry, **17**, 1543–1558 (2007).
DOI: 10.1039/B615954K

[18] Herrington R., Hock K.: Flexible polyurethane foams. Dow Chemical, Midland (1998).

[19] Neff R., Adedeji A., Macosko C. W., Ryan A. J.: Urea hard segment morphology in flexible polyurethane foam. Journal of Polymer Science Part B: Polymer Physics, **36**, 573–581 (1997).
DOI: 10.1002/(SICI)1099-0488(199803)36:4<573::AID-POLB4>3.0.CO;2-Q

[20] Tobushi H., Okumura K., Endo M., Hayashi S.: Thermomechanical properties of polyurethane-shape memory polymer foam. Journal of Intelligent Material Systems and Structures, **12**, 283–287 (2001).
DOI: 10.1106/FNSX-AP9V-QP1R-NMWV

[21] Madbouly S. A., Lendlein A.: Shape-memory polymer composites. Advanced in Polymer Science. **226**, 41–95 (2010).
DOI: 10.1007/12_2009_28

[22] Maitland D. J., Small W., Rodriguez J., Wilson T. S., Ortega J. M., Buckley P. R., Hartman J.: Prototype laser-activated shape memory polymer foam device for embolic treatment of aneurysms. Journal of Biomedical Optics, **12**, 030504/1–030504/3 (2007).
DOI: 10.1117/1.2743983

[23] Tobushi H., Matsui R., Hayashi S., Shimada D.: The influence of shape-holding conditions on shape recovery of polyurethane-shape memory polymer foams. Smart Materials and Structures, **13**, 881–887 (2004).
DOI: 10.1088/0964-1726/13/4/026

[24] Tey S. J., Huang W. M., Sokolowski W. M.: Influence of long-term storage in cold hibernation on strain recovery and recovery stress of polyurethane shape memory polymer foam. Smart Materials and Structures, **10**, 321–325 (2001).
DOI: 10.1088/0964-1726/10/2/318

[25] Metcalfe A., Desfaits A-C., Salazkin I., Yahia L., Sokolowski W. M., Raymond J.: Cold hibernated elastic memory foams for endovascular interventions. Biomaterials, **24**, 491–497 (2003).
DOI: 10.1016/S0142-9612(02)00362-9

[26] Lee S. H., Kim J. W., Kim B. K.: Shape memory polyurethanes having crosslinks in soft and hard segments. Smart Materials and Structures, **13**, 1345–1350 (2004).
DOI: 10.1088/0964-1726/13/6/007

[27] Lee S. H., Jang M. K., Kim B. K.: Shape memory effects of molded flexible polyurethane foam. Smart Materials and Structures, **16**, 2486–2492 (2007).
DOI: 10.1088/0964-1726/16/6/052

[28] Kim B. K., Lee S. Y., Xu M.: Polyurethanes having shape memory effects. Polymer, **37**, 5781–5793 (1996).
DOI: 10.1016/S0032-3861(96)00442-9

[29] Brydson J. A.: Rubbery materials and their compounds. Elsevier, London (1988).

eXPRESS Polymer Letters Vol.6, No.1 (2012) 70–77
Available online at www.expresspolymlett.com
DOI: 10.3144/expresspolymlett.2012.8

Preparation of polydivinylbenzene/natural rubber capsule encapsulating octadecane: Influence of natural rubber molecular weight and content

*A. Chaiyasat, C. Waree, K. Songkhamrod, P. Sirithip, V. Voranuch, P. Chaiyasat**

Department of Chemistry, Faculty of Science and Technology, Rajamangala University of Technology Thanyaburi, Klong 6, Thanyaburi, 12110 Pathumthani, Thailand

Received 2 June 2011; accepted in revised form 4 August 2011

Abstract. The encapsulation of octadecane (OD) as heat storage material was studied. The core-shell polydivinylbenzene (PDVB)/natural rubber (NR) capsules encapsulating OD was prepared using the Self-assembling of Phase Separated Polymer (SaPSeP) method by suspension polymerization. The mixture of dispersed phase consisting of DVB, NR, OD and benzoyl peroxide was added in polyvinyl alcohol aqueous solution and then homogenized at 5,000 rpm for 5 minutes. The obtained monomer droplet emulsion was subsequently polymerized at 80°C for 8 hours resulting in PDVB/NR capsule encapsulating OD. The influence of molecular weight and content of NR on the encapsulation efficiency and thermal properties of the encapsulated OD were investigated. It was found that both factors affected on the preparation of PDVB/NR/OD capsule. High molecular weight NR restricted phase separation of formed PDVB. High NR content also reduced phase separation of PDVB due to the increase of internal viscosity. Then, only the incorporation of appropriate molecular weight and content of NR resulted in the formation of PDVB/NR/OD capsule.

Keywords: *thermal properties, encapsulation, heat storage materials, natural rubber*

1. Introduction

In recent years, microcapsules of heat storage materials have attracted for many applications such as air condition of building, solar heat storage and thermally adaptable fibers [1–3]. Paraffin waxes such as tetradecane (TD), hexadecane (HD), octadecane (OD), nonadecane (ND), and eicosane are useful as one group of numerous heat storage materials that melt and solidify at a wide range of temperatures, making them attractive for many applications [4]. Several methods have been carried out to prepare heat storage microcapsules. The *in situ* polymerization to fabricate the microcapsules and nanocapsules containing OD core with melamine-formaldehyde shell [5], resorcinol-modified melamine-formaldehyde shell [6] were reported. Three types of paraffin waxes (HD, OD and ND) were encapsulated through complex coacervation of natural and biodegradable polymers, gum arabic-gelatin mixture [7]. Polystyrene (PS) microcapsules containing paraffin wax were synthesized by suspension like polymerization [8]. The Self-assembling of Phase Separated Polymer (SaPSeP) method is one of many methods applied for the encapsulation of them [9–12]. The polymer chains formed during polymerization in the monomer droplet are diffused and trapped near the interface based on surface coagulation and gradually piled at the inner interface resulting in a polymer shell. After the completion of polymerization, heat storage material was encapsulated inside as the capsule core. Previously, we have prepared the microcapsule of polydivinylbenzene (PDVB) encap-

*Corresponding author, e-mail: p_chaiyasat@mail.rmutt.ac.th

sulated OD (PDVB/OD) by microsuspension polymerization utilizing the SaPSeP method [13]. The prepared capsules are spherical with smooth outer surface.

Currently, there is a high level of interest in the utilization of natural polymers due to environmantal awareness. Natural rubber (NR) is one of the most important biopolymers in Thailand. NR latex is exuded from the *Hevea brasiliensis* tree as an aqueous emulsion [14]. It displays excellent elasticity and flexibility widely used in various applications such as medical gloves and tubing. Therefore, it is interesting to incorporate NR into PDVB shell. It not only improves the mechanical properties of PDVB shell but also reduces the utilization of petrochemical monomer corresponding with their costs.

In this study, the preparation of microcapsule encapsulating OD in polymer composite shell of PDVB and NR (PDVB/NR/OD) was carried out by suspension polymerization utilizing the SaPSeP method. The influence of the molecular weight of NR and its content on the encapsulation efficiency and thermal properties of encapsulated OD were investigated.

2. Experimental

2.1. Materials

DVB (Aldrich, Wisconsin, USA; purity, 80%) was washed with 1 N sodium hydroxide (BDH Prolabo, Leuven, Belgium) and distilled water to remove polymerization inhibitors before use. NR (Thai Rubber Latex Co., Ltd., Bangkok, Thailand) was used as received and oxidized with aqueous hydrogen peroxide solution (QReC, Auckland, New Zealand; 30% v/v) in the combination with sonication to reduce the molecular weight. Poly (vinyl alcohol) (PVA) (Aldrich, Wisconsin, USA; degree of saponification, 87–90%) was used as received. Reagent-grade benzoyl peroxide (BPO) (Merck, Munich, Germany) was purified by recrystallization. OD (Aldrich, Wisconsin, USA; 99.5%) was used as received. Tetrahydrofuran (THF) (QReC, Auckland, New Zealand; HPLC grade) was used as received.

2.2. Microcapsules preparation

The microcapsules of PDVB/NR/OD were prepared by suspension polymerization under the conditions listed in Table 1. The homogeneous organic phase of DVB/NR and OD at the ratio of 50:50% wt/wt (approximately 10 wt% of aqueous solution) were mixed with BPO (8 wt% of monomer) and then added to the aqueous phase containing PVA (1.5 g of PVA in 150 g of water). Emulsification was carried out by homogenization at the speed of 5000 rpm for 5 minutes resulting in the organic phase droplets dispersed in the aqueous medium. The resulting emulsions were subsequently transferred to the reactor and polymerized at 80°C for 8 hours with the stirring rate at 200 rpm under N_2 atmosphere.

2.3. Characterizations

Number- and weight-average molecular weights (M_n and M_w, respectively) and molecular weight distributions of NR and oxidized NR were determined using a gel permeation chromatograph (GPC) (Water 2414, Water, USA) with two poly(styrene-divinylbenzene) gel columns (Phenogel $5 \cdot 10^3$ and $5 \cdot 10^5$ A, 7.8 mm i.d × 30 cm, Phenomenex, USA) connected in series. The flow rate of THF as eluent was maintained at 1.0 ml/min with column temperature of 40°C and elution was monitored with refractive index detector. The columns were calibrated with six standard PS samples ($2.5 \cdot 10^3$–$6.0 \cdot 10^5$, M_w/M_n = 1.05–1.15).

The prepared capsules were observed with an optical microscope (OM) (SK-100EB & SK-100ET, Seek, Thailand) and scanning electron microscope (SEM) (JSM-6510, JEOL, Japan) to investigate the inner structure and surface morphology of the microcapsules, respectively. The ultrathin cross sections of the capsules were observed with a transmission electron microscope (TEM) (JEM-1230, JEOL, Japan). Dried capsule particles were dispersed in epoxy matrix, cured at room temperature for 24 h and then microtomed.

The OD content in microcapsule was determined with thermogravimetric analyzer (TGA) (TGA 4000, Perkin-Elmer, USA) using heating rate of 5°C/min. The latent heats of crystallization (H_c) and melting (H_m) and the crystallization (T_c) and melting (T_m) temperatures of OD encapsulated in microcapsules in aqueous solution (solid content: ca 10%) were measured with a differential scanning calorimeter (DSC) (DSC 4000, Perkin-Elmer, USA) under a N_2 flow with the scanning temperature range and rate of 0–40°C and 5°C/min, respectively. To compare H_c and H_m of the encapsulated OD having different wt% in the capsule particles and also bulk

OD, the H_c and H_m values were used in the unit of joule per 1 g of encapsulated OD (J/g-OD). They were calculated from the cooling/heating peak area of DSC thermogram and OD content obtained from TGA analysis using the Equation (1):

$$\text{J/g-OD} = \frac{A}{B} \cdot 100 \quad (1)$$

where $A = H_c$ or H_m of encapsulated OD in microcapsule dispersion obtained from DSC thermogram (J/g-sample), B = %OD in microcapsule dispersion obtained from TGA thermogram.

3. Results and discussion

The PDVB/NR/OD microcapsules prepared with various weight percents of NR (M_n = 308 130 g/mol) were observed with OM compared with PDVB/OD capsules as shown in Figure 1. The PDVB/OD capsules (Figure 1a) were spherical and OD core was completely encapsulated with PDVB shell. When NR was added, phase separation was not observed although at the lowest content at the lowest content as shown in Figure 1b–d. It can be explained that high molecular weight NR (308 130 g/mol) incorporated into the monomer droplets increases the internal viscosity. Therefore, it may prevent phase separation of PDVB formed during polymerization.

Table 1. Recipes for the preparation of PDVB/NR capsules with encapsulated OD by suspension polymerization[a] of DVB/NR/OD droplets prepared by homogenization[b]

Ingredient	NR (wt% of DVB)			
	0	**1**	**2.5**	**5**
DVB [g]	7.5	7.5	7.5	7.5
NR[c] [g]	0.0	0.075	0.188	0.375
OD [g]	7.5	7.5	7.5	7.5
BPO [g]	0.8	0.8	0.8	0.8
PVA [g]	1.5	1.5	1.5	1.5
Water [g]	150	150	150	150

[a]80°C, 8 hours, stirring rate at 200 rpm, N_2
[b]5000 rpm, 5 min
[c]M_n (polydispersity index; M_w/M_n): 308 130 (2.87), 162 519 (2.19), 146 001 (2.60) and 89 923 (15.62)

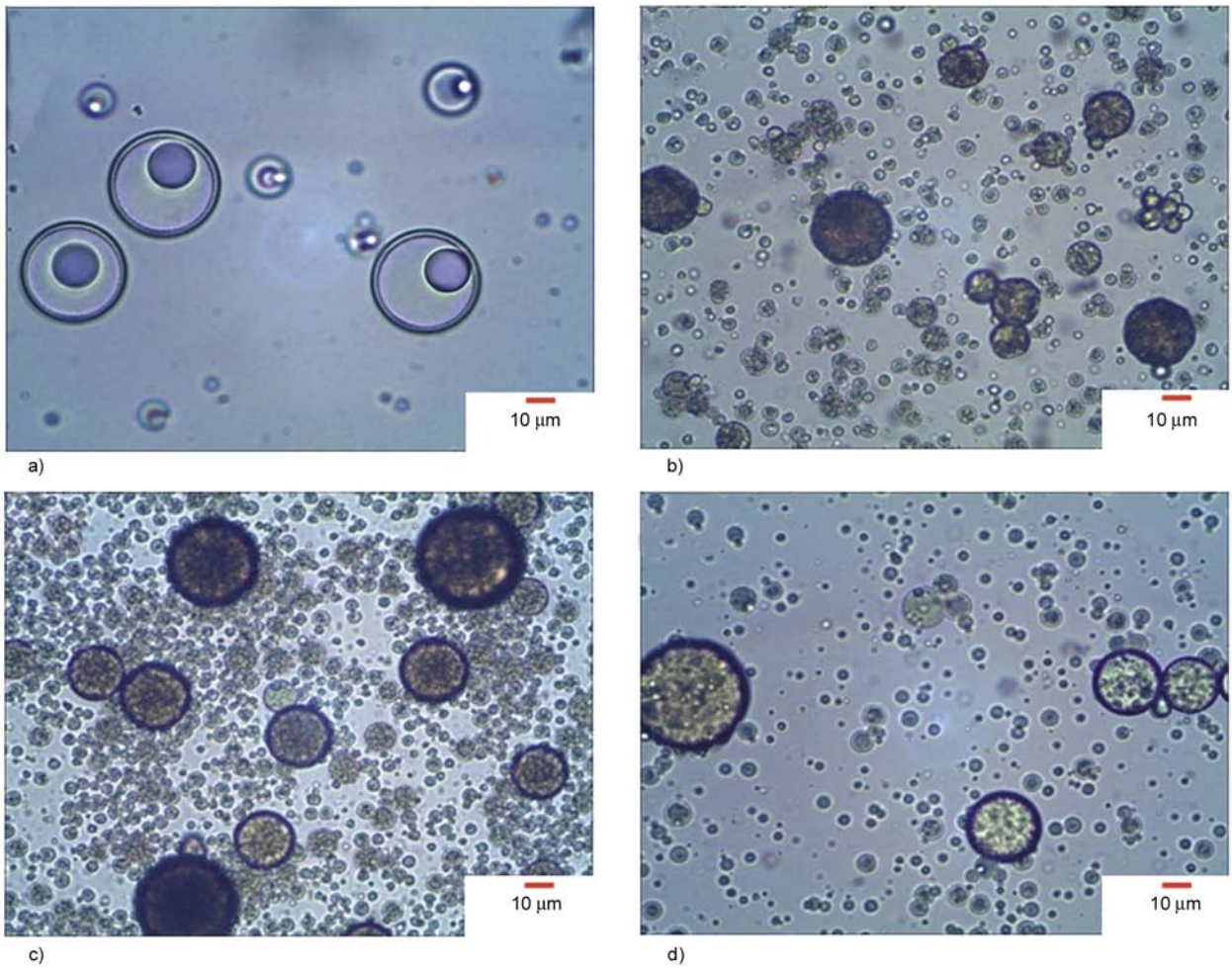

Figure 1. The optical micrographs of PDVB/NR/OD particles with NR having M_n 308 130 g/mol. NR (wt% of DVB): (a) 0; (b) 1; (c) 2.5 and (d) 5

To clarify this assumption, the utilization of the lower molecular weight NR was studied.

The original NR was oxidized with various amounts of aqueous hydrogen peroxide solution (30% v/v) in the combination with sonication for 1 hour to reduce its molecular weight. The obtained NR having different Mn measured with GPC was used for the preparation of PDVB/NR/OD capsules.

The PDVB/NR/OD capsules prepared with NR (1 wt% of DVB) having different molecular weights (M_n: 162 519, 146 001 and 89 923 g/mol) were shown in Figure 2. All of conditions show that the spherical particles were obtained. In the case of 162 519 g/mol NR (Figure 2a), it clearly shows heterogeneous particle where PDVB/NR shell encapsulate OD core. This indicates that using the lower molecular weight NR than the original one (308 130 g/mol; Figure 1) may reduce the internal viscosity resulting in the formation of the core-shell particles. However, when further decreased molecular weight NR (Mn: 146 001 and 89 923 g/mol) were used, the homogeneous particles were observed as shown in Figure 2b and 2c. These phenomena may be due to their molecular weight distributions being quite high as shown in the term of polydispersity index. They are 2.52 and 15.62 for 146 001 and 89 923 g/mol, respectively. This means that they still have many long chains polymer which easily obstruct the phase separation. In the case of 162 519 g/mol NR, although the M_n is higher than those of the lower ones, its molecular weight distribution is quite narrow (polydispersity index; 2.19) resulting in less long chain polymer components. This indicates that not only molecular weight of NR but also polydispersity index affect the formation of polymer capsule. However, we will discuss this phenomenon in more detail in the future. Therefore, NR having M_n about 162 519 g/mol was selected to prepare the PDVB/NR/OD capsules in the further study.

To increase NR content, the study of influence of NR weight content on the preparation of the capsule was shown in Figure 3. When low NR contents (1 and 2.5 wt% of DVB) were added, the spherical microcapsules were obtained as shown in Figure 3b and 3c. They clearly show PDVB/NR shell encapsulating OD core. However, at higher NR content (5 wt% of DVB), the polymer chains seem to be distributed throughout the particles. These results suggested that during polymerization the present of low concentration NR did not inhibit phase separation of PDVB chains formed in the monomer

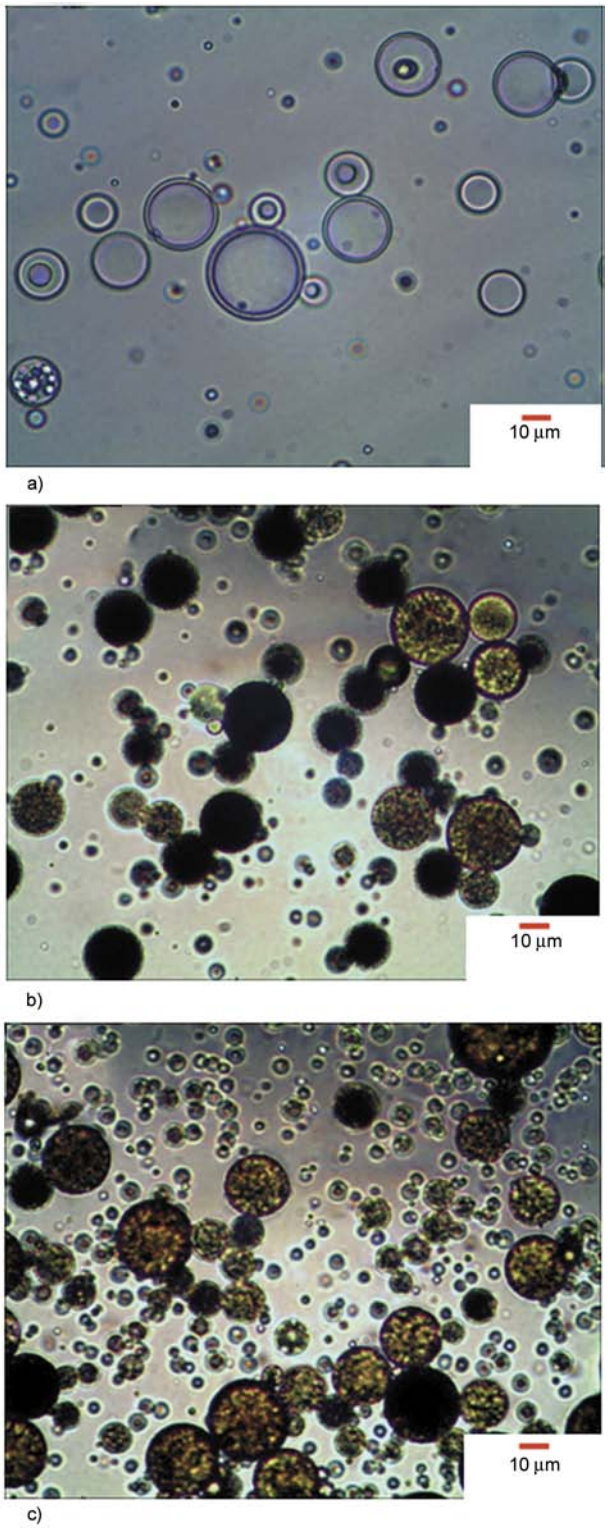

Figure 2. The optical micrographs of PDVB/NR/OD particles prepared with various molecular weight of NR at 1 wt% of DVB. M_n (polydispersity index) of NR [g/mol]: (a) 162 519 (2.19); (b) 146 001 (2.52) and (c) 89 923 (15.62)

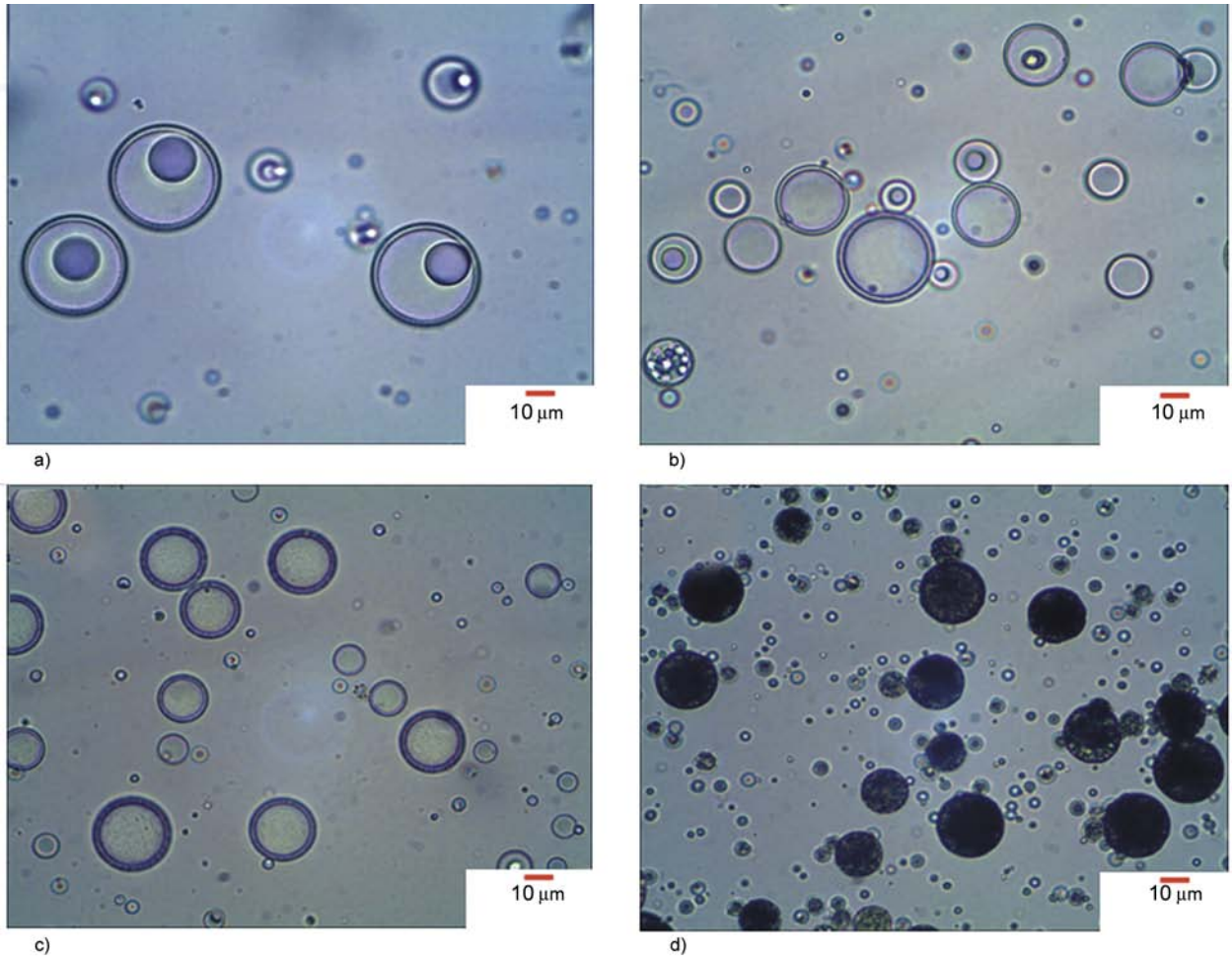

Figure 3. The optical micrographs of PDVB/NR/OD particles with NR having M_n 162,519 g/mol. NR (wt% of DVB): (a) 0; (b) 1; (c) 2.5 and (d) 5

droplets. Therefore, PDVB chains can easily diffuse to the interface and adsorb there to form the polymer shell resulting in the formation of the polymer capsule. Nevertheless, the increases of NR content until reaching a critical value (5 wt% of DVB) reduced phase separation due to high internal viscosity. In this case, the formed PDVB could not diffuse to the droplet interface resulting in homogeneous morphology particles.

The surface morphology of the capsules observed with SEM (Figure 4) support the results of OM that PDVB/OD and PDVB/NR/OD with NR 1 wt% of DVB have smooth outer surface of PDVB shell. No hole was observed indicating the complete encapsulation of the polymer shell. It is consistent with ultrathin cross-section TEM micrograph (Figure 5) showing the PDVB shell encapsulating OD core. In contrast, the rough outer surface of PDVB/NR/OD with NR 5 wt% of DVB was observed which may be due to incomplete encapsulation or less phase separation of formed PDVB chain to the outer surface. The distribution of PDVB and NR chains throughout the particles inhibit the formation of strong PDVB shell resulting in uneven surface particles.

TGA analysis showed the degradation temperature and the composition of the capsule. The degradation of PDVB/NR/OD capsule (Figure 6 curve d) consists of three steps weight loss corresponding to the decomposition of water, OD (Figure 6 curve a) and PDVB (Figure 6 curve c), respectively. In comparison with OD, the decomposition temperature of encapsulated OD was slightly higher than that of bulk OD due to the encapsulation. The NR (1 wt% of DVB) degradation was not observed due to low content. The OD content was further used for the calculation of heat of transitions of the encapsulated OD in the following section.

The thermal properties of encapsulated OD were measured with DSC. DSC thermograms of encap-

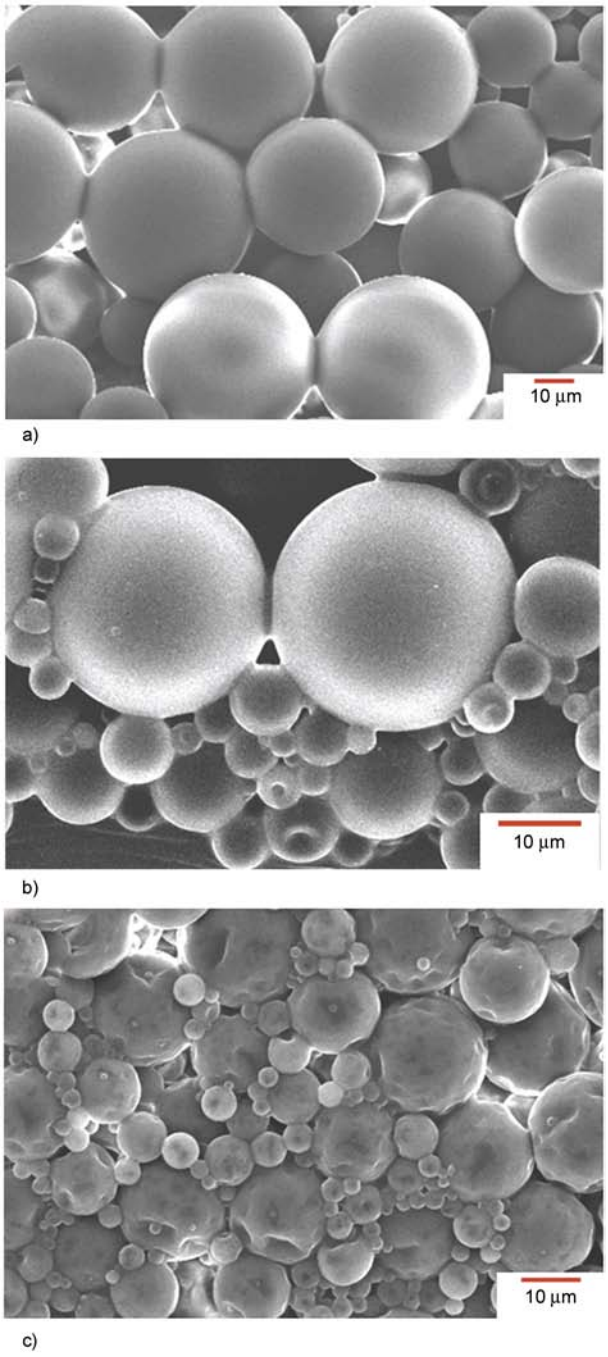

Figure 4. SEM micrographs of PDVB/NR/OD particles with NR having M_n 162 519 g/mol. NR (wt% of DVB): (a) 0; (b) 1 and (c) 5

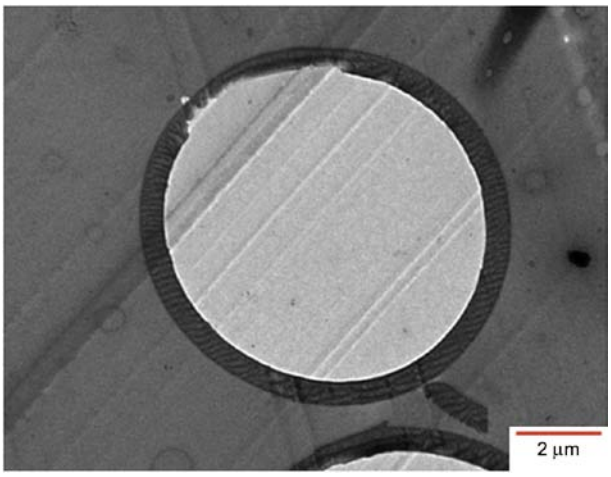

Figure 5. TEM micrographs of cross sections of PDVB/OD capsule

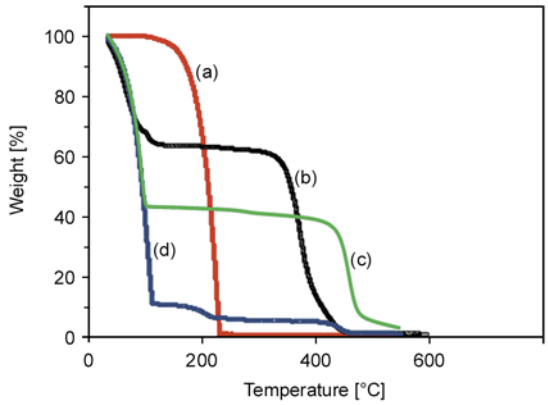

Figure 6. TGA thermograms of (a) bulk OD, (b) NR latex, (c) PDVB and (d) PDVB/NR/OD capsule (1 wt% of DVB) measured at the heating rate of 5°C/min

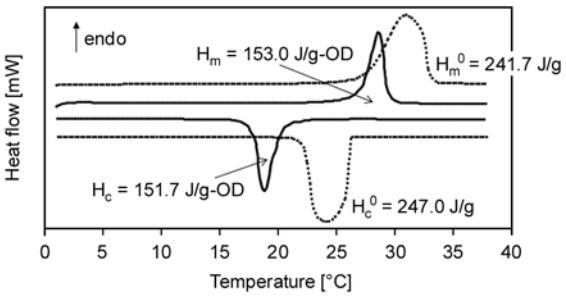

Figure 7. DSC thermograms of bulk OD (dot line) and encapsulated OD (solid line) in PDVB particles measured at the scanning rate of 5°C/min

sulated OD in PDVB capsules (Figure 7) showed that the H_m (153.0 J/g-OD) and H_c (151.8 J/g-OD) of encapsulated OD were lower than those of the bulk OD (241.7 and 247.0 J/g of H_m^0 and H_c^0, respectively). This phenomenon is quite general for the encapsulation as also observed by other researchers [3, 5, 6, 9–11, 15–19]. The possible reason of the reduction of H_m and H_c of encapsulated heat storage materials is that the phase separation between the polymer shell and heat storage material core was incomplete as in the case of PDVB/HD microcapsules prepared by suspension polymerization [11]. Moreover, the capsules may have some unreacted monomers or oligomers incorporated at the interface between polymer shell and heat storage material core as in the case of PS/HD microcapsules pre-

pared by suspension polymerization [16]. They may act as a compatibilizer and increase the miscibility between polymer and heat storage material leading to the decrease of their phase separation in the monomer droplet. However, to overcome this problem, the copolymerization with more polar monomers is a good idea as copolymerization of PDVB with methyl acrylate, ethyl acrylate and butyl acrylate [11]. In the case of phase transition temperature, T_m of encapsulated OD (28.3°C) was almost the same as that of bulk OD (30.0°C). In contrast, T_c was shifted to lower temperature compared to bulk OD. This phenomenon is called supercooling. Supercooling leads to the reduction of T_c resulting in a release of latent heat at a lower temperature or over a wider temperature range. This effect may limit the applications. To prevent supercooling, nucleating agents were incorporated in the heat storage materials core during the encapsulation process. However, increasing nucleating agent content decreased the latent heat [20, 21]. At the present, there is still no good solution to overcome this problem.

In the case of PDVB/NR capsules, the thermal properties of encapsulated OD were similar as those of OD in PDVB capsule. H_m and H_c of encapsulated OD were much lower than those of the bulk ones while a slightly lower than those of OD in PDVB capsule. It may be due to the presence of NR in OD matrix at the interface of capsule shell and OD core reduces the crystallization of the encapsulated ones. However, in the case of homogeneous particle, the increase of NR weight percent up to 5 showed greatly decreasing of heat of transition of the OD (Table 2). It may be due to the distribution of NR

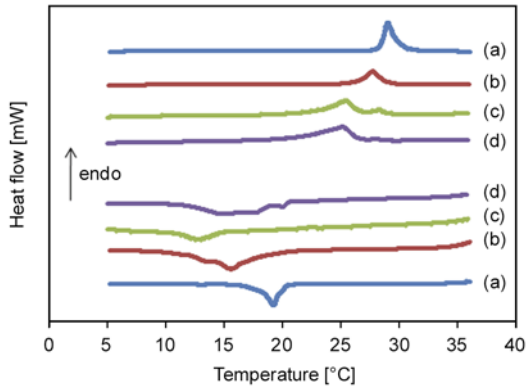

Figure 8. DSC thermograms of the encapsulated OD in PDVB/NR capsule measured at the scanning rate of 5°C/min. NR (wt% of DVB): (a) 0; (b) 1; (c) 2.5 and (d) 5

Table 2. Thermal properties of encapsulated OD in PDVB/NR capsule prepared with various weight percents of NR

NR (wt% of DVB)	Heat of transition (J/g-OD)	
	H_c	H_m
0	151.7	153.1
1	124.2	129.1
2.5	126.3	124.7
5	106.7	114.5

and PDVB, which restricts the crystallization of OD. T_m of the encapsulated OD was almost the same as that of the bulk ones while T_c was also shifted to the lower temperature compared to bulk OD (Figure 8). However, due to their high total surface area compared to bulk OD, these PDVB/NR/OD capsules are quite acceptable for energy storage applications even having a slightly lower latent heat.

4. Conclusions

The microcapsule of PDVB/NR encapsulating OD was successfully prepared by suspension polymerization utilizing the SaPSeP method. Using high molecular weight NR, the capsule could not be formed even though at 1 wt% of DVB. This is due to the presence of NR in the monomer droplet increasing the internal viscosity which prevents phase separation of PDVB formed during polymerization. However, the reduction of NR molecular weight leads to the formation of polymer capsule at the appropriate NR content. It was also found that the increase of NR content gradually reduced phase separation of PDVB due to the increase of internal viscosity. Therefore, it can be concluded that both molecular weight and content of NR are important factors affected on the preparation of PDVB/NR/OD capsule. The thermal properties of encapsulated OD in the PDVB/NR capsule were lower than those of bulk as in the case of PDVB capsule.

Acknowledgements

This work was supported by The National Research Council, Thailand (No. 44703).

References

[1] Su J-F., Wang L-X., Ren L.: Preparation and characterization of double-MF shell microPCMs used in building materials. Journal of Applied Polymer Science, **97**, 1755–1762 (2005).
DOI: 10.1002/app.21205

[2] Peng S., Fuchs A., Wirtz R. A.: Polymeric phase change composites for thermal energy storage. Journal of Applied Polymer Science, **93**, 1240–1251 (2004). DOI: 10.1002/app.20578

[3] Cho J-S., Kwon A., Cho C-G.: Microencapsulation of octadecane as a phase-change material by interfacial polymerization in an emulsion system. Colloid and Polymer Science **280**, 260–266 (2002). DOI: 10.1007/s00396-001-0603-x

[4] Farid M. M., Khudhair A. M., Razack S. A. K., Al-Hallaj S.: A review on phase change energy storage: Materials and applications. Energy Conversion and Management, **45**, 1597–1615 (2004). DOI: 10.1016/j.enconman.2003.09.015

[5] Zhang X. X., Fan Y. F., Tao X. M., Yick K. L.: Fabrication and properties of microcapsules and nanocapsules containing *n*-octadecane. Materials Chemistry and Physics, **88**, 300–307 (2004). DOI: 10.1016/j.matchemphys.2004.06.043

[6] Zhang H., Wang X.: Fabrication and performances of microencapsulated phase change materials based on *n*-octadecane core and resorcinol-modified melamine–formaldehyde shell. Colloids and Surfaces A: Physicochemical and Engineering Aspects, **332**, 129–138 (2009). DOI: 10.1016/j.colsurfa.2008.09.013

[7] Onder E., Sarier N., Cimen E.: Encapsulation of phase change materials by complex coacervation to improve thermal performances of woven fabrics. Thermochimica Acta, **467**, 63–72 (2008). DOI: 10.1016/j.tca.2007.11.007

[8] Sánchez P., Sánchez-Fernandez M. V., Romero A., Rodríguez J. F., Sánchez-Silva L.: Development of thermo-regulating textiles using paraffin wax microcapsules. Thermochimica Acta, **498**, 16–21 (2010). DOI: 10.1016/j.tca.2009.09.005

[9] Chaiyasat P., Suzuki T., Minami H., Okubo M.: Thermal properties of hexadecane encapsulated in poly (divinylbenzene) particles. Journal of Applied Polymer Science, **112**, 3257–3266 (2009). DOI: 10.1002/app.29648

[10] Chaiyasat P., Ogino Y., Suzuki T., Okubo M.: Influence of water domain formed in hexadecane core inside cross-linked capsule particle on thermal properties for heat storage application. Colloid and Polymer Science, **286**, 753–759 (2008). DOI: 10.1007/s00396-007-1831-5

[11] Chaiyasat P., Ogino Y., Suzuki T., Minami H., Okubo M.: Preparation of divinylbenzene copolymer particles with encapsulated hexadecane for heat storage application. Colloid and Polymer Science, **286**, 217–223 (2008). DOI: 10.1007/s00396-007-1764-z

[12] Ogino Y., Suzuki T., Okubo M.: Preparation of poly (divinylbenzene) particles with encapsulated hexadecane for heat storage application (in Japanese). Kobunshi Ronbunshu, **64**, 171–176 (2007). DOI: 10.1295/koron.64.171

[13] Chaiyasat P., Chaiyasat A., Boontung W., Promdsorn S., Thipsit S.: Preparation and characterization of poly(divinylbenzene) microcapsules containing octadecane. Materials Science and Applications, **2**, 1007–1013 (2011). DOI: 10.4236/msa.2011.28136

[14] de Oliveira P. C., de Oliveira A. M., Garcia A., de Souza Barboza J. C., de Carvalho Zavaglia C. A., dos Santos A. M.: Modification of natural rubber: A study by ^{1}H NMR to assess the degree of graftization of polyDMAEMA or polyMMA onto rubber particles under latex form in the presence of a redox couple initiator. European Polymer Journal, **41**, 1883–1892 (2005). DOI: 10.1016/j.eurpolymj.2005.02.030

[15] Zhang X-X., Tao X-M., Yick K-L., Wang X.: Structure and thermal stability of microencapsulated phase-change materials. Colloid and Polymer Science, **282**, 330–336 (2004). DOI: 10.1007/s00396-003-0925-y

[16] Ai Y., Jin Y., Sun J., Wei D.: Microencapsulation of n-hexadecane as phase change material by suspension polymerization. e-Polymers, no. 098 (2007).

[17] Sarı A., Alkan C., Karaipekli A., Uzun O.: Microencapsulated *n*-octacosane as phase change material for thermal energy storage. Solar Energy, **83**, 1757–1763 (2009). DOI: 10.1016/j.solener.2009.05.008

[18] Sarı A., Alkan C., Karaipekli A.: Preparation, characterization and thermal properties of PMMA/*n*-heptadecane microcapsules as novel solid–liquid microPCM for thermal energy storage. Applied Energy, **87**, 1529–1534 (2010). DOI: 10.1016/j.apenergy.2009.10.011

[19] Zhang H., Wang X.: Synthesis and properties of microencapsulated *n*-octadecane with polyurea shells containing different soft segments for heat energy storage and thermal regulation. Solar Energy Materials and Solar Cells, **93**, 1366–1376 (2009). DOI: 10.1016/j.solmat.2009.02.021

[20] Zhang X-X., Fan Y-F., Tao X-M., Yick K-L.: Crystallization and prevention of supercooling of microencapsulated *n*-alkanes. Journal of Colloid and Interface Science, **281**, 299–306 (2005). DOI: 10.1016/j.jcis.2004.08.046

[21] Fan Y. F., Zhang X. X., Wang X. C., Li J., Zhu Q. B.: Super-cooling prevention of microencapsulated phase change material. Thermochimica Acta, **413**, 1–6 (2004). DOI: 10.1016/j.tca.2003.11.006

eXPRESS Polymer Letters Vol.6, No.1 (2012) 78–94
Available online at www.expresspolymlett.com
DOI: 10.3144/expresspolymlett.2012.9

Preparation and characterization of interpenetrating networks based on polyacrylates and poly(lactic acid)

H. Kaczmarek[*], *I. Vuković-Kwiatkowska*

Department of Chemistry and Photochemistry of Polymers, Faculty of Chemistry, Nicolaus Copernicus University, Toruń, Poland

Received 27 April 2011; accepted in revised form 8 August 2011

Abstract. Three different, multifunctional acrylic monomers were photopolymerized in a matrix of poly(lactic acid), PLA, using 2-hydroxy-2-methyl-1-phenyl-propan-1-one as a photoinitiator. The kinetics of the photopolymerization of monomers in PLA, studied with Fourier Transform Infrared Spectroscopy, has been compared to analogous processes of pure monomers under the same conditions (room temperature, air atmosphere). Additionally, poly(ethylene glycol) was added to acrylate/PLA blends as plasticizer.The highly crosslinked networks obtained were characterized by FTIR and optical microscopy. The amount of insoluble gel has been estimated gravimetrically. It was found that the studied systems are characterized by very high polymerization rate, moreover, efficient grafting of polyacrylates on PLA takes place. The observed morphology indicates the heterogeneity of formed networks. The glass transition temperature of PLA in studied blends has been determined by differential scanning calorimetry.

Keywords: *polymer blends and alloys, interpenetrating polymer networks, poly(lactic acid), polyacrylates*

1. Introduction

Synthetic polymers such as polyethylene, polystyrene, poly (vinyl chloride), polyacrylates, polyesters and many other commercial macromolecular products are mainly obtained from fossil fuels. They are broadly applied in practice because of their numerous advantages such as durability, flexibility, resistance to water and chemical compounds. They are lightweight and easily processed, and also have good mechanical properties as well as possibility of various modifications.

However, their utilization is not a trivial task. Problems of waste management have led researchers and manufacturers to develop effective methods of manufacturing of materials offering an alternative to conventional plastics. Moreover, the rising fossil fuel prices and shrinking of its resources motivate the investigators to search for materials from renewable resources e.g. biopolymers. Such polymers exhibit useful properties of traditional plastics and can be organically recycled because of their biodegradability. This process includes the distribution and hydrolysis of polymers in wastewater, anaerobic digestion with biogas production and decomposition with the participation of oxygen, occurring directly in soil or in compost. Production and usage of biodegradable polymers is a competitive solution to high standards of environmental protection – relatively expensive methods of mechanical recycling of packaging waste from traditional plastics and the need for their transportation, collection and segregation into homogeneous polymers [1, 2].

An example of biopolymer commonly used worldwide is poly (lactic acid)/ polylactide (PLA), which has excellent application properties. PLA is energy

[*]Corresponding author, e-mail: halina@chem.uni.torun.pl

saving, non-toxic, biocompatible and biodegradable; it has good thermal processability and rheological properties. However, for special applications, it should be modified by several additives (such as fillers, fibers). Numerous recent works were devoted to PLA modification [3–5].

For instance, PLA in mixture with polysaccharides: starch and cellulose fibers lowers the production cost and reduces the time of biological decomposition. Increase of rigidity and higher heat resistance of PLA can be achieved by introduction of inorganic fillers such as talc, mica, glass. Improved resistance to tensile load is associated with the addition of rubber to PLA. Nevertheless, the problem of incompatibility occurs during mixing of PLA with other polymers such as styrene based rubbers, thus, modified polymers containing functional groups or compatibilizers have to be used additionally.

In the case of PLA modified with polyacrylates, and especially with poly(methyl methacrylate), the films obtained from these blends are transparent, have higher glass transition temperature but lower crystallinity degree in comparison to pure PLA. Polycarbonates improves PLA the thermal stability and the resistance to cracking when stretched [1, 6].

A common feature of polymer blends is the presence of a continuous phase of one polymer in which other components are dispersed. Depending on the degree of dispersion and on the chemical properties one can obtain real solutions or colloidal systems.

Different physical properties of compositions can be obtained by polymer mixing in the molten state. Such manufacturing depends e.g. on the ingredient types and their interactions, stability of the mixture and its morphology. Research of the crystalline phases (in the case of semicrystalline polymers), observations of the blend structure and defects, heterogeneity of multicomponent polymeric films are carried out using precise optical methods.

There is still a lack of information of the possibility of PLA modification using ultraviolet radiation, contrary to other polymers [7–9].

Photo(co)polymerization is a polymer synthesis method induced by photon absorption of the substrate. The products of photopolymerization are protective polymer coatings on the surface of various materials such as wood, metal, paper, glass, ceramics [10, 11]. Photografting, photocrosslinking or surface properties modification are other broadly used processes occurring upon electromagnetic radiation. The process of initiation of photochemical reactions requires the application of efficient photoinitiators [12–14].

The chemical structure of monomer used in photopolymerization has essential influence on the properties of product obtained. Depending on the monomer functionality one can obtain linear polymers (from monomers containing one double bond or cyclic group in molecule) or the form of a spatially cross-linked networks (from multifunctional monomers) [15].

The main advantages of multifunctional monomers polymerization is high speed of process that takes place at low, room temperature in air atmosphere (without the necessity of removing oxygen) and in the absence of organic solvents. Due to these features, photochemical manufacturing of materials is classified as an environmentally friendly technology.

Poly(lactic acid) as biodegradable and commercially available polymer found numerous applications in the production of food packaging. PLA is a good candidate for replacement of poly(ethylene terephthalate), PET – basic material for drink bottles, which is not susceptible to biological decomposition. However, PLA is characterized by a relatively high gas permeability compared to PET. Thus, intensive studies are devoted to improvement of its barrier properties. One of the possibilities of PLA modification is the preparation of blends with other components. The aim of our work was to obtain and characterize the interpenetrating polymer network based on poly (lactic acid) and polyacrylates capable to crosslinking.

2. Experimental part

2.1. Chemicals

The following chemicals were used:

- polymer – poly(lactic acid) PLA (2002 D, NatureWorks, USA) with average molecular weight ~200 000;
- monomers: pentaerythritol triacrylate (PETA, M = 298 g/mol), pentaerythritol tetraacrylate (PETeA, M = 352 g/mol), dipentaerythritol pentaacrylate (DPEPA, M = 524 g/mol) – all from Polyscience Inc, Warrington, PA, USA;

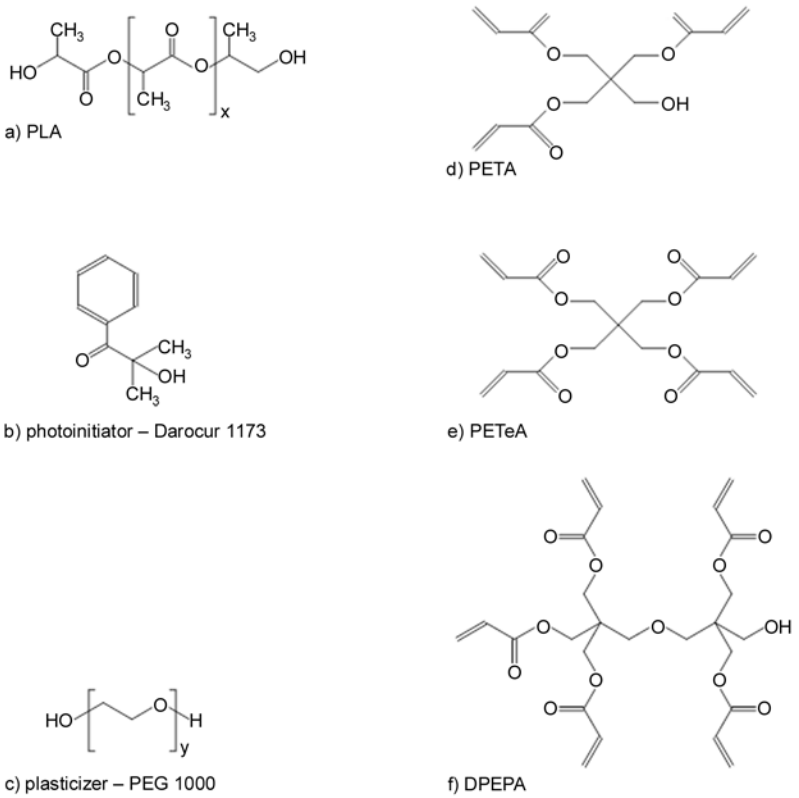

Figure 1. The chemical structure of poly(lactic acid), PLA (a); photoinitiator – Darocur 1173 (b); plasticizer – PEG (c) and monomers: PETA (d), PETeA (e) and DPEPA (f)

– photoinitiator 2-hydroxy-2-methyl-1-phenyl-propan-1-one (DAROCUR 1173, Ciba, Switzerland);
– solvent – chloroform (Polish Chemical Reagents, POCH S.A., Poland),
– plasticizer – poly (ethylene glycol), PEG 1000 (M_v = 1000 g/mol, Polish Chemical Reagents, POCH S.A., Poland).

All materials were used as received. The chemical structures of all studied compounds are shown in Figure 1.

Number of functional groups per monomer molecule is: 3 in PETA, 4 in PETeA, 5 in DPEPA and functionality (calculated as number of C=C bonds per 1 kg of monomer) is: 10.07 in PETA, 11.36 in PETeA and 9.54 in DPEPA.

2.2. Sample preparation

Pure PLA films were obtained from 3 wt% solution in chloroform. IPN films were prepared by mixing the monomers and photoinitiator with polymer solution. 1:1 weight ratio of polymer to the monomer and 5 wt% concentration of photoinitiator were used. After mixing, solution was poured onto leveled plates (from KBr for FTIR spectroscopy or from glass for microscopic observations and for determination of gel amount). Additionally, 10% wt. plasticizer was introduced for improvement of the sample flexibility. Simultaneously, the films of pure monomers with 5 wt% initiator were also prepared. After solvent evaporation at room temperature and careful drying (also at room temperature) in the dark, the solid blends were UV-irradiated for curing.

The samples of the same thickness (~10 μm) have been chosen for all experiments.

2.3. Photopolymerization conditions

The high pressure mercury vapor lamp, HPK 125 W, Philips has been used for polymerization. The wavelength range and intensity of the incident light at the sample level was 248–578 nm and 16.65 W/m^2, respectively.

The following conditions were applied: time of irradiation – maximum 5 minutes, air atmosphere and room temperature (20°C). The home-made device equipped with a photographic shutter has been applied for short curing times. It allows exposure to

the sample for a split second (since 1/60 s). The polymerization kinetics were monitored by FTIR spectroscopy. The film thickness was about 0.02 mm.

2.4. FTIR spectroscopy

FTIR spectra with 2 cm^{-1} resolution were recorded using Genesis II spectrophotometer (Mattson, USA) in range of 400–4000 cm^{-1}. The number of scans was 32. The spectra analysis i.e. baseline correction, normalization, band intensity calculation has been done using WinFirst 3.57 software (Mattson Instruments).

The absorption band at 809 cm^{-1}, attributed to =C–H bending vibration, was chosen for monitoring the course of photopolymerization. The conversion degree (X, %) has been calculated by Equation (1) on the basis of the number of consumed double bonds:

$$\text{Conversion degree}\,[\,\%\,] = \left(1 - \frac{A_t}{A_0}\right)\cdot 100\,\% \quad (1)$$

where A_t/A_0 is the ratio of absorbance of the band at 809 cm^{-1} in the spectrum of the sample after t time of reaction to the absorbance of unirradiated sample. This ratio corresponds to the amount of unreacted double bonds.

The maximum rate of polymerization was obtained from the slope of the linear part of recorded kinetic curve (where the conversion degree was plotted vs time of reaction).

2.5. Optical microscopy

Samples of unmodified and modified films of PLA were observed under the inverted research microscope Nikon ECLIPSE TE 2000S in the bright field technique using the Hoffman modulation contrast (HMC) allowing the enhancement of specimen contrast. The magnification was 100×. The most representative images of samples were taken using a microscopic digital camera. Transfer of microscopic image on the computer screen was possible due to the specialized program of documentation and analysis of microscopic image ELEMENTS Ar NIS 2.30.

2.6. Scanning Electron Microscopy

Morphology of the samples was observed using LEO1430 field-emitting Scanning Electron Microscopy at accelerating voltage of 5 kV. All specimens were coated with thin layer of gold.

2.7. Differential Scanning Calorimetry

DSC measurements were carried out in helium atmosphere in the temperature range of 20–250ºC using Diamond DSC power compensation type (Perkin-Elmer). Indium was used for calibration. The following conditions were applied: flow rate – 20 ml/min, heating and cooling rate – 200ºC/min, sample weight – ca. 5 mg. The glass transition temperature of PLA (T_g) was obtained from the inflection point on DSC curve (second run).

2.8. Gel amount and grafting degree

Gel content in obtained IPN films was determined gravimetrically, according to Equation (2):

$$\text{Gel}\,[\,\%\,] = \frac{m_g}{m_0}\cdot 100\,\% \quad (2)$$

where m_g is weight of insoluble gel and m_0 is total weight of initial sample.

After curing and weighting, the samples were dissolved in chloroform: soluble part (sol) was extracted and separated from insoluble fraction. The extraction has been done first in chloroform at room temperature for 24 hours, then, in Soxhlet apparatus in boiling chloroform for 24 hours.

The separated gel was dried in vacuum oven to a constant weight. The amount of gel is an average of at least three values.

Taking into account that the weight ratio of PLA to acrylate was always 50:50, the amount of grafted PLA (so-called grafting degree) has been obtained from the Equation (3):

$$\text{Grafting degree}\,[\%] = \frac{\text{gel amount} - 50}{50}\cdot 100\,\% \quad (3)$$

3. Results and discussion

3.1. Spectral characterization of reagents

FTIR spectra of reagents used in this work are presented in Figures 2 and 3. Poly(lactic acid) spectrum contains characteristic absorption bands at 2800–3000, 1300–1500 and 756 cm^{-1} which can be assigned to methylene groups (stretching and defor-

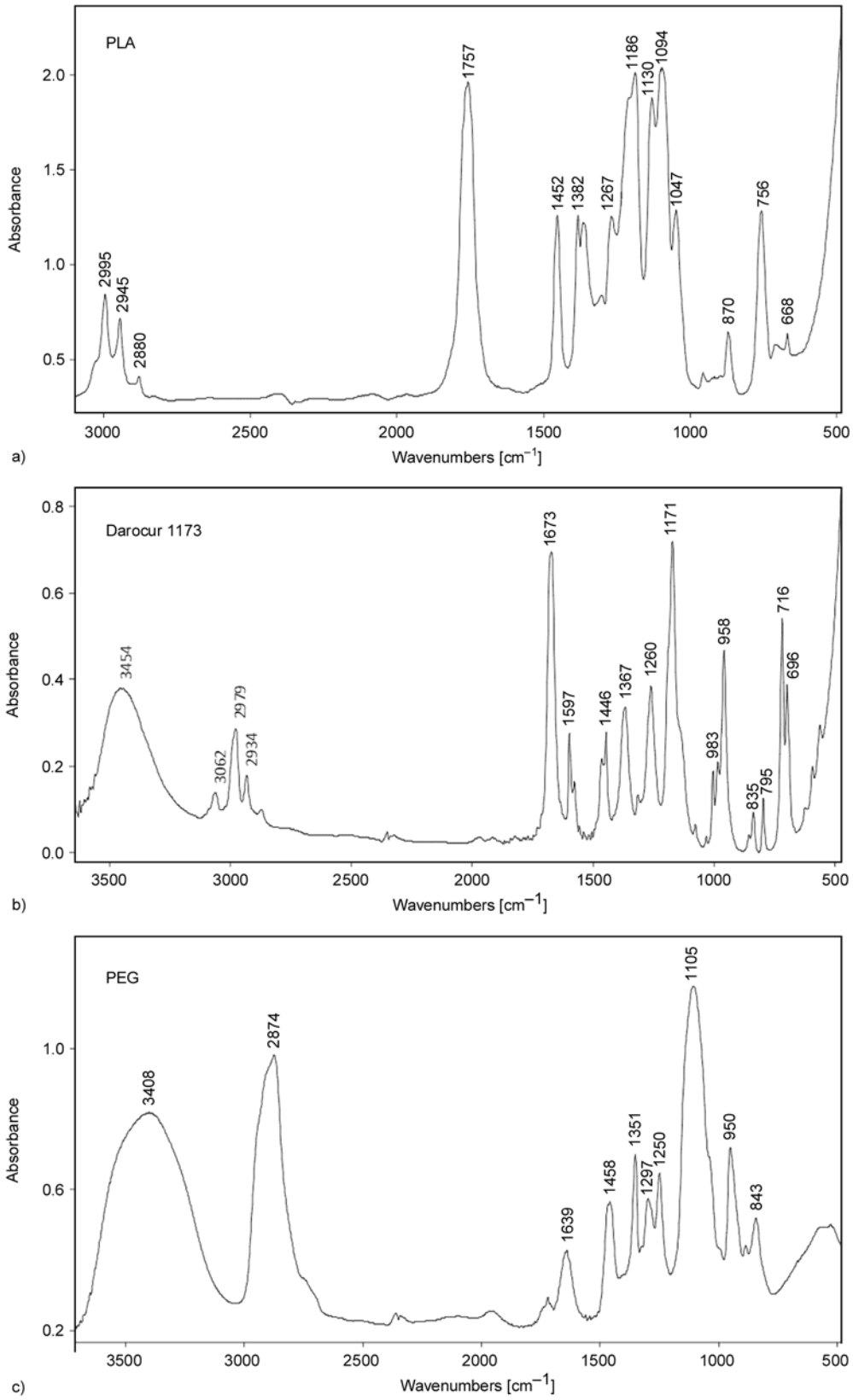

Figure 2. FTIR spectra of virgin reagents: PLA (a), photoinitiator – Darocur 1173 (b) and plasticizer – PEG (c)

mation vibrations, respectively). Strong, sharp peaks at 1757 cm^{-1} due to carbonyls and 1186, 1094 cm^{-1} attributed to C–O–C groups appear (Figure 2a). Only very small, residual hydroxyl band at ~3500 cm^{-1} can be seen.

Photoinitiator (Figure 2b) spectrum exhibits intensive hydroxyl absorption (with maximum at 3460 cm^{-1}), bands at 2800–3100 range, at 1597, 1446, 1367, 958, 716 cm^{-1} assigned to aliphatic and aromatic C–H (stretching and bending), 1673 cm^{-1} (carbonyl) and 1171 cm^{-1} (C–O–C vibrations).

Plasticizer (PEG) spectrum is relatively simple: broad hydroxyl band is centered at about 3400 cm^{-1}, methylene at 2874, 1458, 1351, 1250, 950 and 843 cm^{-1} (stretching and deformation) and ether (strong) at 1113 cm^{-1} (Figure 2c). Additionally, two low intensity peaks appear at carbonyl region (1721, 1639 cm^{-1}) indicating some internal impurities.

As expected, the spectra of tri- tetra- and pentacrylate monomers are very similar because they contain the same type of functional groups (Figure 3). The methyl/methylene (2800–3000 cm^{-1} stretching region), carbonyl (1726 cm^{-1}) and ether (1000–1200 cm^{-1}) bands exist in all acrylate spectra. The broad hydroxyl band (3300–3700 cm^{-1}) is also seen in all spectra, although OH groups are not originally present in PETeA structure. The other characteristic bands, appearing at 1634, 1468, 985 and 809 cm^{-1}, can be assigned to C=C stretching, C–H deformation (in-plane), C–H deformation (out-of plane) and =C–H bending vibrations, respectively.

The distinct difference appears in the stretching methylene range: the ratio of intensities of 2962 to 2898 cm^{-1} bands (A_{2962}:A_{2898}) decreases with an increase of functional groups in monomer molecule (Figure 3a). It changes in the following order:

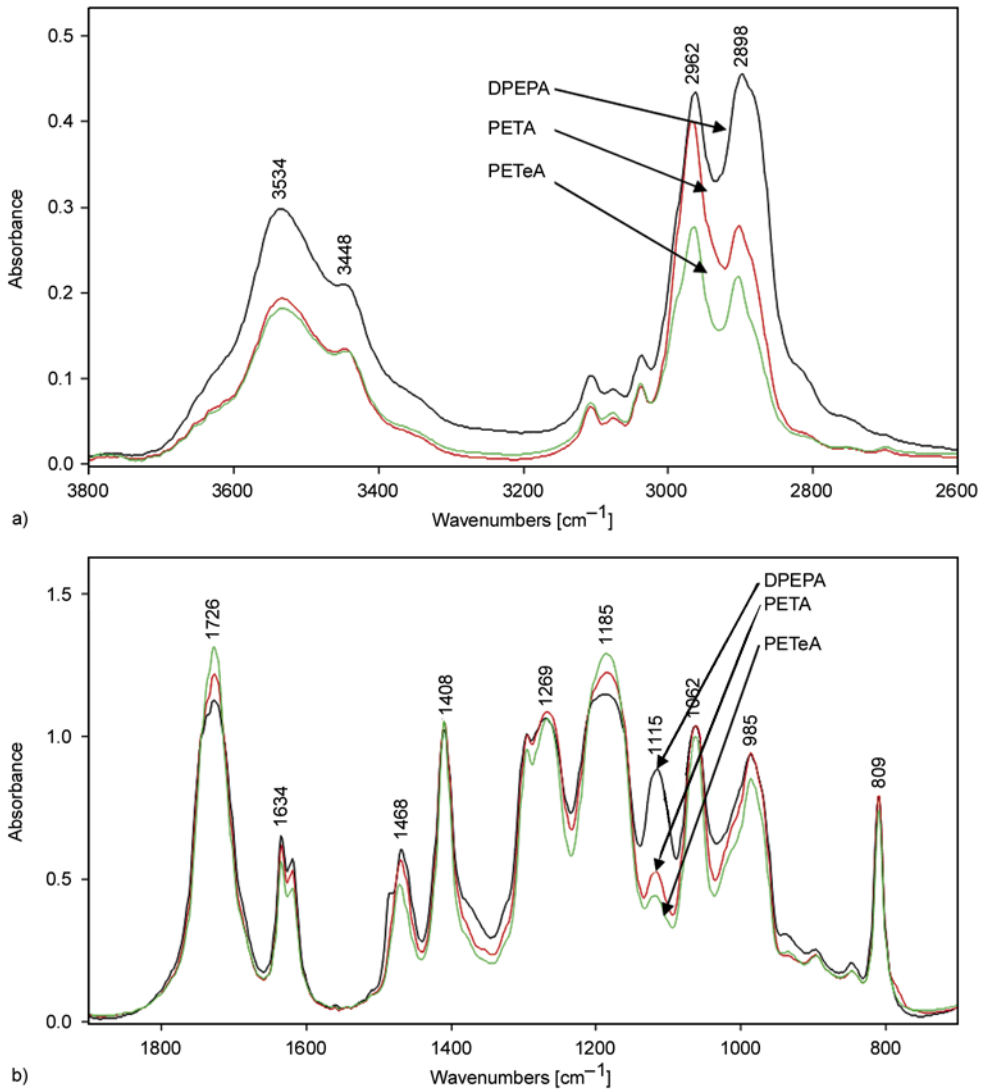

Figure 3. FTIR spectra of three acrylate monomers in 2600–3800 cm^{-1} (a) and 700-1900 cm^{-1} (b) ranges (DPEPA – black, PETA – red, PETeA – green)

$(A_{2962}:A_{2898})(PETA) = 1.452 >$
$(A_{2962}:A_{2898})(PETeA) = 1.279 >$
$(A_{2962}:A_{2898})(DPEPA) = 0.976$

The second modification is seen in 1115 cm^{-1} band attributed to ether type vibrations – the highest intensity of this band is observed for DPEPA containing six C–O–C groups in molecule, contrary to PETeA and PETA (four C–O– bonds/molecule).
The band at 809 cm^{-1}, due to =C–H bending vibrations has been selected for monitoring the progress of photopolymerization.

3.2. General observations concerning IPN preparation

The solutions of acrylate/PLA and acrylate/PLA/PEG blends (containing also photoinitiator) in chloroform as well as solid films obtained after solvent evaporation were completely transparent.
The photopolymerization in all studied systems started immediately after exposure to UV. Process underwent with high efficiency in a few minutes. We decided to finish the kinetic studies after 5 minutes of UV-irradiation although the conversion of double bond was not completed. Longer exposure could be dangerous for IPN specimens because of possibility of photodegradation process. The application of photographic shutter allowed the observation of subtle changes in the first period of photopolymerization and distinguishing the variation between the PLA containing different monomers. The obtained samples of acrylates cured in PLA matrix were translucent, rigid and very brittle, thus poly(ethylene glycol), PEG, was added for plasticization. The course of monomers photopolymerization in the presence of PEG has been also determined.
Figure 4 shows FTIR spectra of acrylate+PLA blends before (black lines) and after 5 minutes UV-irradiation (red curves). In all cases the bands characteristic for both components exists. As predicted, the main changes after photopolymerization occur at bands attributed to double bonds in acrylate monomers: at 1635, 1409, 986 and 809 cm^{-1}. The differences in other absorption bands caused by photocuring are negligible. No new additional peak which could indicate that any other reactions take place.

The mechanism of photopolymerization of multifunctional monomers is described as a free-radical chain reaction [10, 12, 15]. During the first stage of process, photosensitive initiator absorbs quanta of radiation and undergoes excitation followed by the creation of initiating species, usually free radicals. The initiation is mainly dependent on the photoinitiator absorption coefficient, the quantum yield of radicals formation and the intensity of radiation.
The next step is propagation, when active radicals react with monomer molecules leading to chain growth. Because the multifunctional monomers contain a few functional groups, the macromolecules become highly branched, moreover, a high rate of reaction is characteristic for such systems. Particularly, the first period of polymerization is fast, then process slows down due to crosslinking and vitrification. Formed network contains a significant amount of trapped or 'frozen' radicals and unreacted double bonds. The probability of their further reaction is limited (because of segmental mobility restrictions) but is possible. The final conversion is strongly dependent on the mobility of the functional groups, which is also determined by the slow relaxation processes occurring at room temperature even in the dark. The termination is a radical recombination or diffusion-controlled reaction.
The differences in the kinetics and efficiency of the acrylates photopolymerization in PLA in this study are connected mainly with different structure and reactivity of monomers because the conditions of curing were kept constant. The monomers differ mainly in their functionality (expressed as the amount of functional groups per molecule or as the number of double bounds per kilogram of monomer) and branching degree. As the viscosity of monomers is very high, the inhibiting action of oxygen is reduced because of its negligible diffusion.

3.3. Kinetics of polymerization of acrylate monomers alone and in PLA matrix

The rate of polymerization was evaluated by FTIR spectroscopy on the basis of the band at 809 cm^{-1}, which is attributed to the double bond vibrations in acrylate monomer. Examples of absorbance decrease in FTIR spectrum of photopolymerized PETeA and PETeA in PLA film are shown in Figure 5. Analysis of other bands attributed to unsaturated groups (e.g. 1634, 1409 cm^{-1}) leads to the same conclusions.

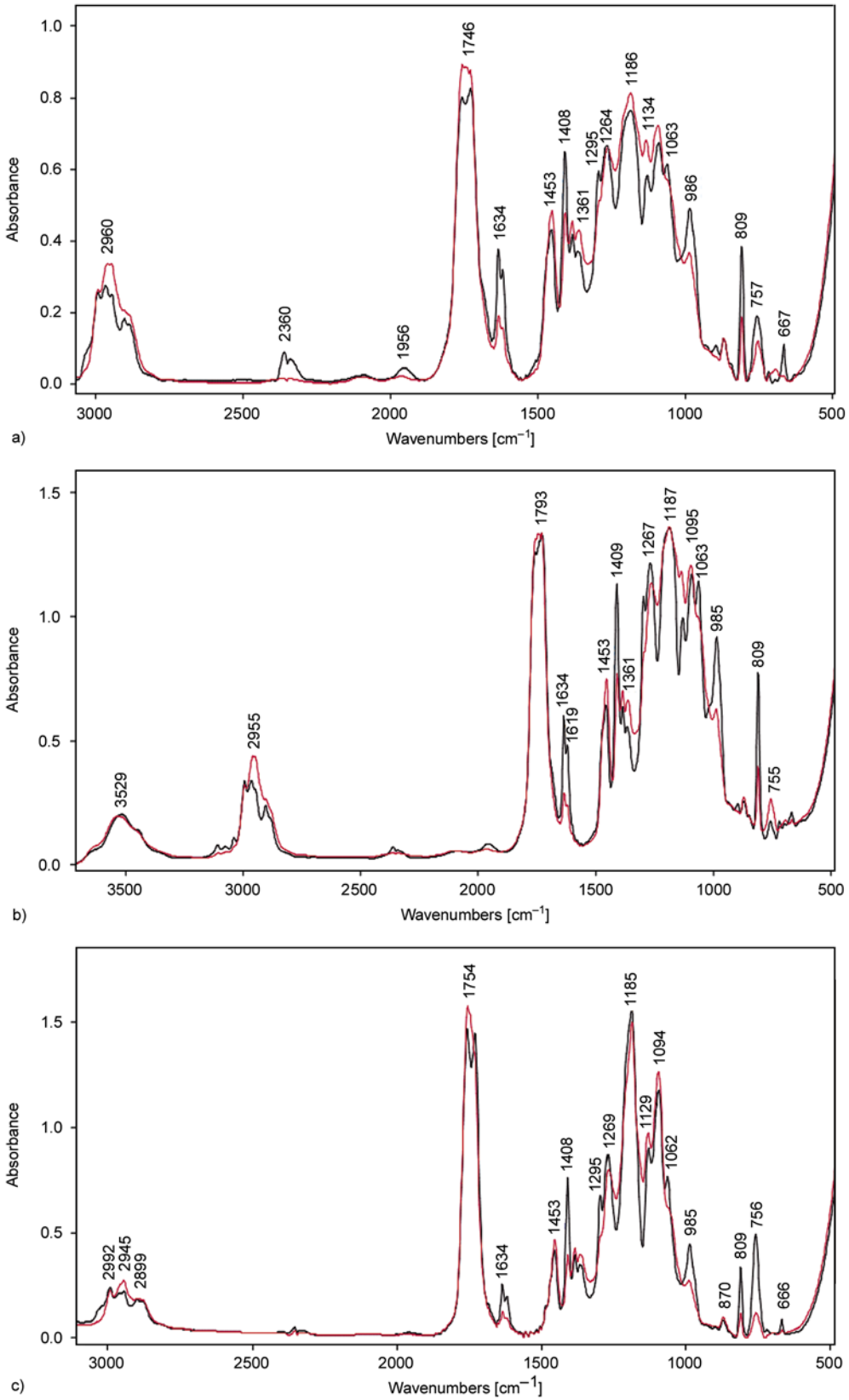

Figure 4. FTIR spectra of acrylate/PLA networks before irradiation (black) and obtained after 5 min photopolymerization (red); PLA/PETA (a), PLA/DPEPA (b) and PLA/ PETeA (c)

Because of the lack of induction period, the inflection point has not been observed on the plot of conversion degree versus exposure time (Figure 6), thus, the maximum polymerization rate, R_p^{max}, was

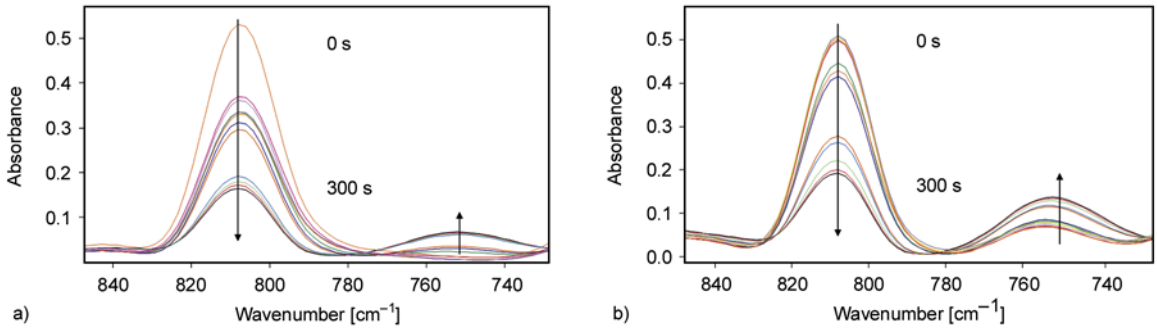

Figure 5. Changes of C=C band during 5 min photopolymertization of PETeA (a) and PETeA in PLA matrix (b)

obtained from the slope of straight-line part of these kinetic curves for the beginning period of reaction.

Photopolymerization of tri-, tetra- or penta-acrylate monomers (Figure 6a) as well as photocuring of these reagents in PLA matrix, occurs rapidly (Figures 6b and 6c). The shapes of conversion curves are similar for DPEPA, PETA and PETeA.

In the case of polymerization of monomers alone, the highest polymerization rate has been observed up to approximately 10 seconds (Figure 6a). At this time the conversion degree achieved already 50% but the final conversion (after 5 min of exposure) does not exceed 80%. The course of photopolymerization is similar and kinetic curves partially overlap.

The main kinetic parameters are listed in Table 1. As one can see, R_p^{max} slightly decreases with the increase of functional groups for monomers photopolymerized alone, thus, 50% conversion is reached fastest in PETA (after 2 s) and lowest in DPEPA (13 s). For that reason, needed dose for 50% conversion is relatively low (below 220 J/m^2). After approximately 50 seconds, the polymerization significantly slows down and finally, after about 2 minutes of exposure, a plateau is observed. Such behavior is in accordance to results obtained previously for these monomers in similar conditions [11, 16].

Photopolymerization rates of acrylates in PLA films (Figure 6b) are lower than those previously observed without polymeric matrix. Unexpectedly, the highest R_p^{max} among these three specimens was observed for PETeA in PLA. The maximum rate can be ordered as follows:

R_p^{max}(PETeA + PLA) > R_p^{max}(DPEPA + PLA) > R_p^{max}(PETA + PLA)

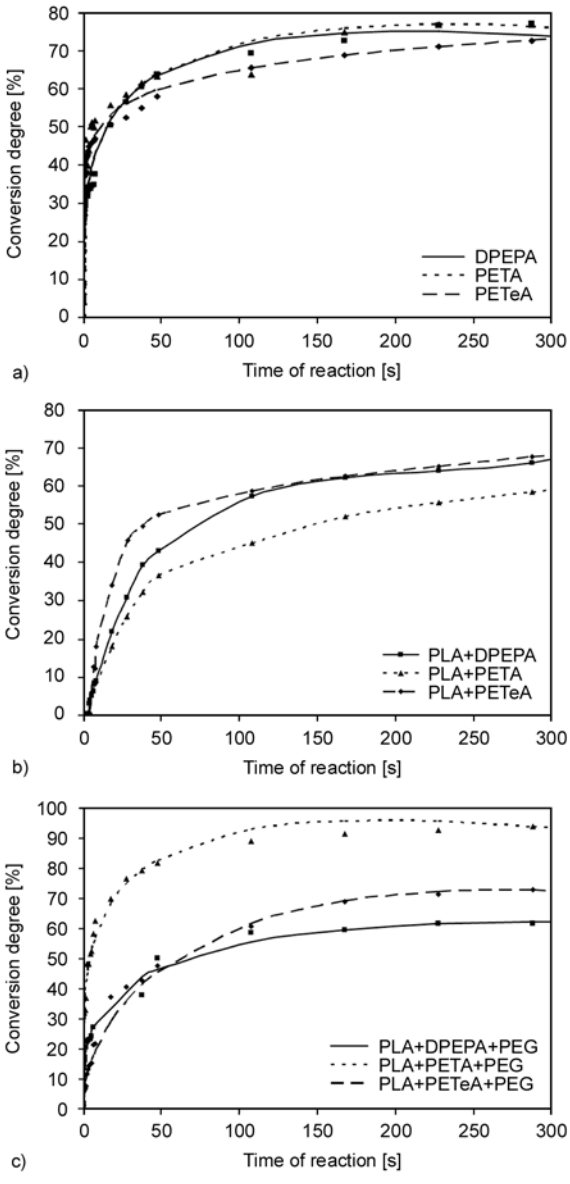

Figure 6. Kinetics of photopolymerization of acrylates (a), acrylates in PLA matrix (b) and acrylate/PLA/PEG formulations (c); presence of photoinitiator – 5 wt%, process conducted in air atmosphere at room temperature upon a HPK lamp

Since, the 50% conversion degree in these formulations is reached after longer irradiation time (comparing to ~10 s for pure monomers) i.e. at ~40, 70 and 150 s in PETeA + PLA, DPEPA + PLA and PETA + PLA, respectively. Therefore, the energy necessary for fifty percentage conversion is high (ca. 650–2580 J/m^2). The final efficiency is also lower for all monomers in the blends (below 70% for DPEPA + PLA or PETeA + PLA and about 60% for PETA + PLA). It clearly indicates that acrylate photopolymerization is hampered in the PLA network, which is obviously caused by the trapping of growing macroradicals in polymer matrix, which is in glassy state in the room temperature.

Plasticization of PLA by PEG causes an increase of polymerization rate in the first step compared to the course of reaction in nonplasticized PLA. R_p^{max} values are even higher than those for monomers cured alone (Table 1). 50% conversion is achieved after about 5, 60 and 70 s of UV action in PETA + PLA + PEG, PETeA+PLA+PEG and DPEPA + PLA + PEG, respectively. Assuming that polymer plasticization facilitates the polymerization process because of higher mobility of acrylate monomers and radicals in PLA blends, we can conclude that the best plasticizing effect was found in the network containing PETA. The formation of IPN in this formulation is saving-energy process (83 J/m^2).

The order of R_p^{max} in ternary blends is reversed comparing to the previously indicated for nonplasticized systems:

R_p^{max}(PETA + PLA + PEG) >
R_p^{max}(DPEPA + PLA + PEG) >
R_p^{max}(PETeA + PLA + PEG)

It means that plasticizer increases the rate of phtotopolymerization and this effect is particularly high in the case of PETA + PLA + PEG system where additionally the great conversion degree (exceeding 90%) was found (Figure 6c).

The conversion degree is strictly connected to the number of unreacted acrylate bonds in formed IPN (Table 2), which is the largest in the case of PETA + PLA (nonplasticized) and DPEPA + PLA + PEG.

However, the amount of unsaturations can be reduced by the heating of interpenetrating network above glass transition temperature in which post-polymerization takes place owing to improvement of macrochain mobility and reactivity [17].

Table 1. The parameters characterizing the kinetics of polymerization of acrylate monomers (alone), acrylate monomers in PLA and acrylate + PLA + PEG ternary systems obtained from FTIR

Sample	R_p^{max} [%·s^{-1}]	X(5') [%]	t(50%) [s]	D(50%) [J/m^2]
PETA	2.7	77	2	33
PETeA	2.3	73	10	167
DPEPA	1.6	74	13	216
PETA + PLA	1.0	59	155	2581
PETeA + PLA	2.1	68	39	649
DPEPA + PLA	1.3	67	72	1199
PETA + PLA + PEG	10.0	94	5	83
PETeA + PLA + PEG	3.0	73	62	1032
DPEPA + PLA + PEG	7.7	62	69	1149

R_p^{max} – maximum polymerization rate; X(5') – final conversion degree after 5 min UV action, t(50%) – time needed for 50% conversion; D(50%) – dose needed for 50% conversion of monomer. Formulations and reaction conditions: acrylate to PLA ratio = 1:1, 5%(m/m) Darocur 1173, 10%(m/m) PEG placticizer, UV-source – HPK lamp, incident intensity – 16.65 W/m^2, air atmosphere and room temperature.

Table 2. The amount of gel [%] formed in acrylate monomers, acrylate monomer + PLA blends and acrylate + PLA + PEG, estimated grafting degree of PLA and number of unreacted double bonds after 5 minutes of photoreaction (conditions as in Table 1).

Sample	Total amount of gel [%]	Gel containing PLA [%]	Degree of PLA grafting [%]	Number of unreacted C=C [%]
PETA	99.5	–	–	23
PETeA	99.7	–	–	27
DPEPA	100.0	–	–	26
PETA + PLA	96.6	46.6	93.2	41
PETeA + PLA	94.4	44.4	88.8	32
DPEPA + PLA	88.8	38.8	77.6	33
PETA + PLA + PEG	93.3	43.3	86.6	6
PETeA + PLA + PEG	98.8	48.8	97.6	27
DPEPA + PLA + PEG	74.8	24.8	49.6	48

3.4. Gel formation of pure acrylate monomers and in PLA matrix

The acrylate monomers applied for preparation IPN are known as crosslinking agents. In fact, the efficiency of gel formation in our system is very high. An insoluble gel was formed in both cases: during photopolymerization of acrylate monomer alone as well as in PLA matrix (also in the presence of plasticizer). The values of percentage amount of gel after 5 min photocuring are listed in Table 2.

One can observe, that gel content exceeds 50% in all polyacrylate/PLA specimens (although the amount of introduced monomer is always 50%). It clearly indicates that PLA, which does not undergo photocrosslinking when is exposed alone, has to participate in photoprocesses in the presence of acrylate monomers. Two possibilities should be taken into consideration: first, most probable, is physical entanglement of PLA macrochains in the rapidly formed acrylate system. This way interpenetrating polymer network is formed. Second option is photografting process of increasing acrylate molecule onto PLA chains. It suggests that created free radicals (from initiator photolysis or growing acrylate macroradicals) are able to abstract hydrogen atom from PLA. The simple recombination of two types of macroradicals (PLA and polyacrylate) forms the graft or random copolymer. Direct grafting is also probable because HPK lamp emits high energy radiation and some free macroradicals can be generated in PLA, which can further react with acrylate monomer, recombine with any other (macro)radical or undergo chain transfer reaction (onto polyacrylate). Another possibility of formation of covalent bonds between both network constituents is possibility of ester exchange (transesterification) between ester PLA groups and hydroxyl groups present in PETA and DPEPA:

$$RCOOR' + R''OH \rightleftharpoons RCOOR'' + R'OH$$

where RCOOR′ is PLA and R″OH is PETA, DPEPA or polyPETA, polyDPEPA.

Transesterification is also possible between PLA macromolecules and PEG which contain hydroxyl end-groups. Moreover, monomers containing OH groups (PETA and DPEPA) can directly participate in the additional curing with PEG and PLA.

Assuming that the monomer in the blend was completely crosslinked, one can conclude that the grafting degree, expressed as the amount of PLA involved in this process, is very high (Table 2). The highest amount of gel was found in PETA + PLA (96.6%), which allows determining the grafting degree of PLA equal to 93.2%. Both remained samples, are characterized by slightly lower PLA grafting degree: 88.8 and 77.6% in PETeA + PLA and DPEPA + PLA, respectively. One can conclude that the higher functionality of acrylate monomer negligibly hampers the efficiency of photografting onto PLA, which is probably caused by the competition of very efficient crosslinking of multifunctional monomer.

The added plasticizer slightly modifies the photocrosslinking process of acrylates/PLA blend. The total amount of gel formed after 5 minutes exposure is continually very high (~75–99%), which evidently indicates that besides of acrylates also PLA and PEG molecules are entangled and trapped in IPN.

3.5. Glass transition temperature (T_g)

Pure PLA sample exhibits the glass transition at 56ºC. Moreover, DSC curve contains the crystallization peak above 150ºC. Pure polyacrylates (PETA, PETeA and DPEPA) do not show the glass transition under the applied conditions (temperature range: from –50 to 220ºC). It can be caused by high crosslinking density in these samples – the crosslinking usually strongly depresses the chain mobility.

In the composition of PLA with polyacrylates, an increase of T_g by about 15–18ºC is observed. It is an evidence of restricted chain mobility. As was suggested above, PLA macromolecules are entangled or even covalently bound to crosslinked acrylates (resulting of grafting).

PEG is a flexible polymer characterized by very low glass temperature (below 0ºC) and develops flexibility to other polymers. The plasticization effect is generally attributed to the increase of free volume facilitating macromolecular movements. However, the introduction of PEG (as plasticizer) to PLA+polyacrylate blend only slightly decreases the glass transition temperature.

The plasticization of PLA has been the subject of several works [18–21] but the mechanism is still controversial. Blending of polymers containing functional groups induces intermolecular interactions and excess volume formation. Owing to terminal hydroxyl groups, PEG chains can participate in

Table 3. Glass transition temperature of PLA in studied systems determined from DSC curves

Sample	T_g [°C]
PLA	56
PETA + PLA	71
PETeA + PLA	73
DPEPA + PLA	74
PETA + PLA + PEG	68
PETeA + PLA + PEG	69
DPEPA + PLA + PEG	67

hydrogen bonding and act as 'flexible crosslinks'. The other model is based on the dissolving the polymer in excess PEG, however, it needs higher plasticizer concentration (in our case it was only 10% wt). Although higher amount of PEG usually enhances polymer plasticization, the opposite effect can be observed when phase separation occurs. In studies by Piotrowska *et al.* [18] it was described that the phase separation occurred also during the crystallization in poly(L-lactide) plasticized with poly (propylene glycol).

3.6. Samples morphology

The microstucture of PLA and its interpenetrating networks with three polyacrylates was observed by means of optical microscopy (Figure 7). Pure PLA forms homogeneous, clear film, typical for one component systems. Only small defects can be observed on PLA microphotographs. In microscopic magnification, crystalline forms of PLA are not seen. Probably, the size of crystalline structures are to small for observation under optical microscope.

The structure of polyacrylate + PLA networks (Figures 7b–e) is more diversified, which indicates sample heterogeneity, in spite of the homogeneity of solutions used for film preparation. It means that phase separation occurs just after solvent evaporation, however, the clear phase border is not distinguished on microscopic images. In all studied acrylate/PLA films, small inclusions and regions of different morphology are observed. The size of single grains dispersed in PLA is ca. 5–10 μm. Larger particles, indicating the possibility of their aggregation, can be also seen, particularly in PETA + PLA sample (Figure 7b). However, it should be pointed out that the size of phase-separated domains is controlled by the network density determined by the high functionality of acrylates.

Interesting images were found for samples containing additionally PEG as plasticizer, which is a semicrystalline polymer (Figure 7e–h).

The structure of PLA containing PEG (plasticizer) is rather homogeneous (Figure 7e). Only small inclusions are rarely observed. Comparing images of pure PLA (Figure 7a) and PLA + PEG (Figure 7e) one can conclude that just PEG is responsible for these small imperfections.

PEG formed spherulitic structures (more or less regular) in matrix of PLA and its IPN with PETeA and DPEPA (Figures 7g and 7h). The size range of these crystallites is from few to 200 μm. The morphology of PETA + PLA + PEG specimen (Figure 7f) is rather dissimilar to both others plasticized networks: protrusions of different diameters (from twenty to above 200 μm) appear. This different morphology partially explains the different behavior of this sample upon UV action.

As was demonstrated (Figure 6c), the highest curing rate and conversion degree was found in this case. It suggests that observed morphological structures are characterized by other molecules arrangement (probably less ordered), consequently the plasticizing effect is more evident. Probably, the hydroxyl groups from PETA and PEG interact, which retards the crystallization of plasticizer. Although OH groups are also present in DPEPA but this monomer is more branched, therefore, steric hindrances can make difficult hydrogen bonding formation. In consequence, the rate and efficiency of PETA polymerization in PLA + PEG are higher than those for DPEPA in PLA + PEG.

The specific details of samples structure have been also observed by SEM. The chosen examples are shown in Figure 8. Pure PLA and polyacrylates are relatively uniform with exception of PETA+PLA (Figure 8b). An altered, more heterogeneous morphology was found in the case of ternary blends: polyacrylate+PLA+PEG (Figure 8e-h).

It is necessary to remind that photographs in Figure 8 present the surface morphology of the samples, which can be different from internal structure. The surface of samples composed of acrylates, PLA and PEG is not smooth, some protrusions of different sizes are observed. It indicates that under top layer heterogeneous domains (connected to crystallization and phase separation) were formed.

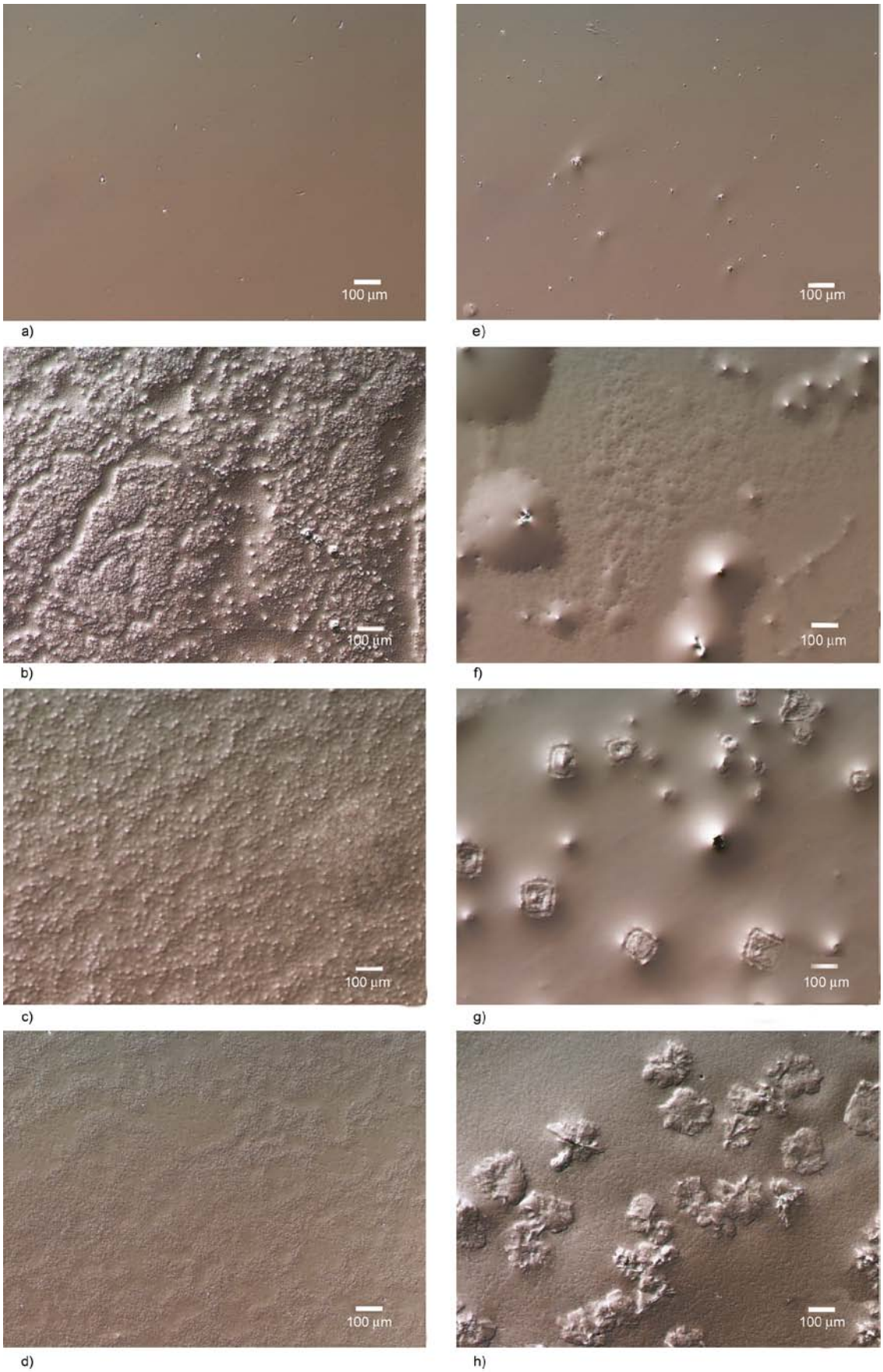

Figure 7. Microphotographs of PLA (a) and photopolymerized blends: PETA + PLA (b), PETeA + PLA (c) and DPEPA + PLA (d) as well as PLA + PEG (e) and photopolymerized ternary blends: PETA + PLA + PEG (f), PETeA + PLA + PEG (g) and DPEPA + PLA + PEG (h)

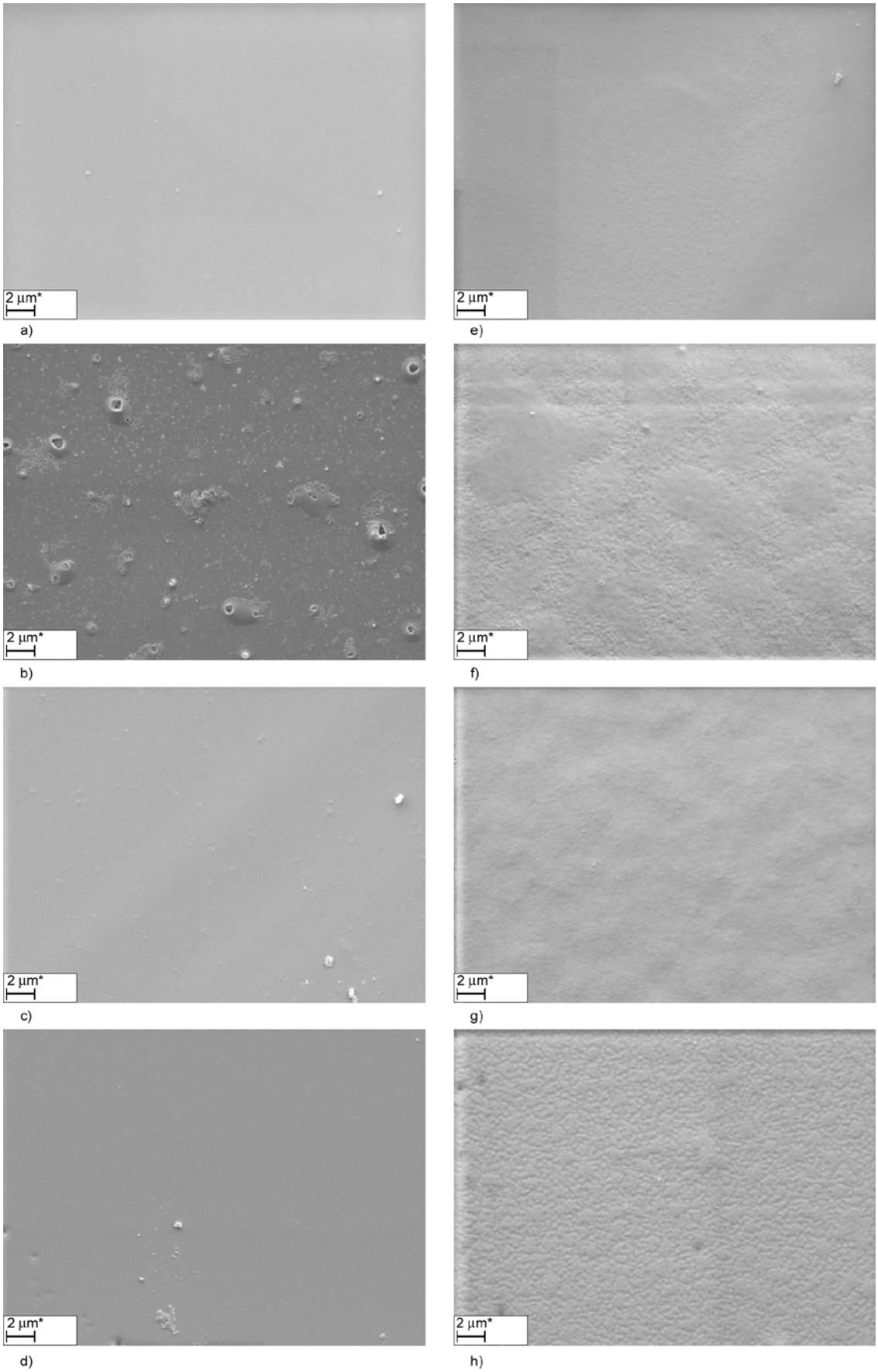

Figure 8. SEM images of PLA (a) and photopolymerized blends: PETA + PLA (b), PETeA + PLA (c) and DPEPA + PLA (d) as well as PLA + PEG (e) and photopolymerized ternary blends: PETA + PLA + PEG (f), PETeA + PLA + PEG (g) and DPEPA + PLA + PEG (h)

On the other hand, surface morphology determines the useful properties of thin polymeric films applied as packaging materials.

Finally it should be mentioned, that networks morphology strongly depends on the conditions of their preparation. It was observed in the case of three components mixture (acrylate+PLA+PEG) obtained by casting from a common solvent. Slow drying in air atmosphere led to formation of relatively large crystalline structures of PEG in network, while the fast drying in vacuum caused generation of numerous tiny spherulite precursors. Nevertheless, they are often covered by a layer of PLA, which forms a kind of surface 'skin'.

3.7. Miscibility considerations

The IPN heterogeneity observed in microphotographs suggests the component separation just after solvent evaporation from PLA/acrylate mixture. The prediction of component miscibility is possible comparing Hildebrand solubility parameters (δ) [22].

The literature values of solubility parameters of PLA and poly(methyl acrylate) or poly(methyl methacrylate) [22–24], chosen as a model compounds for polyacrylates obtained from multifunctional monomers, are listed in Table 4.

The differences arising from experimental error (or from different testing method) are rather broad. From cited data, total solubility parameter (δ_{total}) of PLA is 19.28–21.73 and the δ_{total} range for PMA/PMMA is comparable: 19.1–22.6 $(J/cc)^{0.5}$. According to Hansen's theory, the more detailed analysis can be done using partial solubility parameters concerning dispersion forces (δ_d), polar forces (δ_p) and hydrogen bonding (δ_{hb}) [23, 24]. From Table 3 it is seen, that also the partial solubility parameters of PLA and model acrylate polymers have values in a similar range. It suggests that both polymers, thus, the components of our networks, should be miscible according to the theory.

As reported earlier, the photopolymerization of components characterized by a lack or limited miscibility led to the lower conversion degree comparing to compatible mixture [11, 17].

On the basis of microscopic studies, we can conclude that phase separation occurs in the mixture of monomer + PLA already during film preparation because of differences in molecular weight of polymer and acrylates. Heterogeneity stays after photopolymerization since the NET structure becomes very rapidly inflexible. However, it was proved and explained based on the thermodynamic theory that crosslinking reduces the effective driving force for macrophase separation [25].

On the other hand, the lack of full miscibility is not inconvenient – as it has been reported, the good physical properties of IPN can be obtained from heterogeneous systems [26].

Table 4. Hansen solubility parameters of PLA, poly(methyl acrylate), PMA, and poly(methyl methacrylate), PMMA from literature data (PMA and PMMA were chosen as a model compounds for studied polyacrylates) [22–24].

Polymer	δ_d $[(J/cc)^{0.5}]$	δ_p $[(J/cc)^{0.5}]$	δ_{hb} $[(J/cc)^{0.5}]$	δ_{total} $[(J/cc)^{0.5}]$	Reference
PLA	15.80	8.7	11.10	21.10	[23]
	17.40	7.6	10.50	21.70	[23]
	17.61	5.3	5.80	19.28	[22]
	16.85	9.0	4.05	19.53	[22]
	18.50	9.7	6.00	21.73	[22]
PMA	17.10	1.5	8.40	19.10	[24]
PMMA	18.60	10.5	7.50	22.60	[24]
	19.10	6.5	3.90	20.50	
	15.60	10.5	5.20	19.50	

4. Conclusions

In summary we can conclude that interpenetrating polymer networks of different morphological structures can be obtained using tri- tetra- and pentaacrylate monomers for photopolymerization in poly(lactic acid) matrix. The polyacrylate/PLA IPN's are heterogeneous – the inclusions and aggregates of different size have been observed under optical microscope.

Numerous factors influence the rate of photopolymerization besides of mixture composition: functionality of monomer, components miscibility and phase separation, intermolecular interactions, crystallinity, macrochain flexibility and mobility. Moreover, it was found that the initial sample morphology has strong effect on polymerization and photocuring kinetics influences the final network structure and properties.

On the basis of FTIR kinetics studies, it was found that PETeA exhibited the highest rate of reaction in nonplasticized PLA, whereas PETA photopolymerized fastest in PLA in the presence of PEG. It can be concluded that the number of functional groups and

chemical structure of monomers plays an important role in the course of photopolymerization of acrylates in PLA matrix. Moreover, the decrease of PLA crystallinity in ternary composition facilitates the photopolymerization.

Gravimetric estimation of insoluble gel amount proves that a significant amount of PLA (~50–90%) participates in the photocrosslinking process. It means that full-IPN has been obtained resulting of competitive processes. The following mechanisms of interpenetrating network formation have to be taken into account: physical entanglement and chemical reaction because PLA becomes insoluble (only few % sol fractions were obtained from most samples). Chemical reactions comprise the grafting, simple recombination of macroradicals from both polymeric components as well as transesterification between PLA and monomer containing hydroxyl groups (PETA, DPEPA).

The benefits of this photochemical process are high rates, relatively high conversion degrees, conditions acceptable for industry (room temperature, air atmosphere). In plasticized networks, PEG crystallites were created, what was the reason of insufficient plasticization effect.

FTIR spectroscopy appeared as a convenient, powerful tool for the investigation of photopolymerization kinetics of multifunctional acrylate monomers alone, in linear polymer matrix as well as in plasticized formulations.

The plasticization effect by addition of PEG has been rather weak. In the case of ternary blends, the various factors influence the final properties of networks depending on the polymerization kinetics (composition, plasticizer presence, phase separation, partial crystallization of components and high crosslinking degree).

Finally, it should be added, that owing to the high efficiency of crosslinking, these networks composed of polyacrylate/PLA (1:1) can be recommended as protective surface layers, which are simultaneously ecological materials. The studies of IPN with lower amount (<50%) of acrylate in PLA matrix will be conducted in the future for finding the optimal content for good physical/mechanical/barrier properties and biodegradability.

Acknowledgements

Authors thank Barbara Góralczyk from Department of Pathophysiology, Collegium Medicum, Nicolaus Copernicus University, Bydgoszcz, Poland for making microscopic images.

References

[1] Foltynowicz Z., Jakubiak P.: Polylactid acid – Biodegradable polymer obtained from vegetable resources. Polimery, **47**, 769–774 (2002).

[2] Duda A., Penczek S.: Polylactide [poly(lactic acid)]: Synthesis, properties and applications. Polimery, **48**, 16–27 (2003).

[3] Nieddu E., Mazzucco L., Gentile P., Benko T., Balbo V., Mandrile R., Ciardelli G.: Preparation and biodegradation of clay composites of PLA. Reactive and Functional Polymers, **69**, 371–379 (2009). DOI: 10.1016/j.reactfunctpolym.2009.03.002

[4] Gupta B., Revagade N., Hilborn J.: Poly(lactic acid) fiber: An overview. Progress in Polymer Science, **32**, 455–482 (2007). DOI: 10.1016/j.progpolymsci.2007.01.005

[5] Rasal R. M., Janorkar A. V., Hirt D. E.: Poly(lactic acid) modifications. Progress in Polymer Science, **35**, 338–356 (2010). DOI: 10.1016/j.progpolymsci.2009.12.003

[6] Krasowska K., Brzeska J., Rutkowska M., Dacko P., Sobota M., Kowalczuk M.: The effect of poly(D,L-lactide) modification with poli[(R,S)-3-hydroxybutyrate] on the course of its degradation in natural environments. Polimery, **53**, 730–736 (2008).

[7] Athanassiou A., Lassithiotaki M., Anglos D., Georgiu S., Fotakis C.: A comparative study of the photochemical modifications effected in the UV laser ablation of doped polymer substrates. Applied Surface Science, **154–155**, 89–94 (2000). DOI: 10.1016/S0169-4332(99)00380-3

[8] Mao C., Zhao W. B., Zhu A. P., Shen J., Lin S. C.: A photochemical method for the surface modification of poly(vinyl chloride) with *O*-butyrylchitosan to improve blood compatibility. Process Biochemistry, **39**, 1151–1157 (2004). DOI: 10.1016/S0032-9592(03)00225-5

[9] Bahners T., Häßler R., Gao S-L., Mäder E., Wego A., Schollmeyer E.: Photochemical surface modification of PP for abrasion resistance. Applied Surface Science, **255**, 9139–9145 (2009). DOI: 10.1016/j.apsusc.2009.06.118

[10] Paczkowski J.: Polymer photochemistry. Theory and applications (in Polish). Nicolaus Copernicus University Publishing. Toruń (2003).

[11] Kaczmarek H.: Photopolymerization of trimethylolpropane triacrylate in a matrix of linear-polymers. Polimery, **40**, 333–340 (1995).

[12] Fouassier J. P., Rabek J. F.: Radiation curing in polymer science and technology. Elsevier, London (1993).
[13] Narayanan V., Scranton A. B.: Photopolymerization of composites. Trends in Polymer Science, **5**, 415–419 (1997).
[14] Decker C.: New developments in UV radiation curing of protective coatings. Surface Coatings International Part B: Coatings Transactions, **88**, 9–17 (2005).
DOI: 10.1007/BF02699702
[15] Andrzejewska E.: Photopolymerization kinetics of multifunctional monomers. Progress in Polymer Science, **26**, 605–665 (2001).
DOI: 10.1016/S0079-6700(01)00004-1
[16] Kaczmarek H., Ołdak D., Szalla A.: Networks of photocrosslinked poly(meth)acrylates in linear poly(vinyl chloride). Journal of Applied Polymer Science, **86**, 3725–3734 (2002).
DOI: 10.1002/app.11434
[17] Kaczmarek H., Decker C.: Interpenetrating polymer networks. I. Photopolymerization of multiacrylate systems. Journal of Applied Polymer Science, **54**, 2147–2156 (1994).
DOI: 10.1002/app.1994.070541317
[18] Piorkowska E., Kulinski Z., Galeski A., Masirek R.: Plasticization of semicrystalline poly(L-lactide) with poly(propylene glycol). Polymer, **47**, 7178–7188 (2006).
DOI: 10.1016/j.polymer.2006.03.115
[19] Martin O., Avérous L.: Poly(lactic acid): Plasticization and properties of biodegradable multiphase systems. Polymer, **42**, 6209–6219 (2001).
DOI: 10.1016/S0032-3861(01)00086-6
[20] Feldstein M. M.: Peculiarities of glass transition temperature relation to the composition of poly(*N*-vinyl pyrrolidone) blends with short chain poly(ethylene glycol). Polymer, **42**, 7719–7726 (2001).
DOI: 10.1016/S0032-3861(01)00225-7
[21] Li H., Huneault M. A.: Effect of nucleation and plasticization on the crystallization of poly(lactic acid). Polymer, **48**, 6855–6866 (2007).
DOI: 10.1016/j.polymer.2007.09.020
[22] Agrawal A., Saran A. D., Rath S. S., Khanna A.: Constrained nonlinear optimization for solubility parameters of poly(lactic acid) and poly(glycolic acid)–validation and comparison. Polymer, **45**, 8603–8612 (2004).
DOI: 10.1016/j.polymer.2004.10.022
[23] Schenderlein S., Lück M., Müller B. W.: Partial solubility parameters of poly(D,L-lactide-co-glycolide). International Journal of Pharmaceutics, **286**, 19–26 (2004).
DOI: 10.1016/j.ijpharm.2004.07.034
[24] Lindvig T., Michelsen M. L., Kontogeorgis G. M.: A Flory–Huggins model based on the Hansen solubility parameters. Fluid Phase Equilibria, **203**, 247–260 (2002).
DOI: 10.1016/S0378-3812(02)00184-X
[25] Mamun C. K.: Microstructures in interpenetrating polymer networks. Superlattices and Microstructures, **23**, 1107–1115 (1998).
DOI: 10.1006/spmi.1998.0566
[26] Athawale V. D., Pillay P. S.: Interpenetrating polymer networks based on uralkyd–butylmethacrylate. Reactive and Functional Polymers, **50**, 1–8 (2001).
DOI: 10.1016/S1381-5148(01)00084-0